Microcalorimetric Investigations of Organic Molecules' Adsorption and Lead Deposition on Gold Electrodes from Aqueous Solutions

Zur Erlangung des akademischen Grades einer

DOKTORIN DER NATURWISSENSCHAFTEN

(Dr. rer. nat.)

von der KIT-Fakultät für Chemie und Biowissenschaften

des Karlsruher Instituts für Technologie (KIT)

genehmigte

DISSERTATION

von

M.Sc. Katarina Josifovska

1. Referent: Prof. Dr. Rolf Schuster

2. Referent: Prof. Dr. Andreas-Neil Unterreiner

Tag der mündlichen Prüfung: 24. Oktober 2024

To my sister, Simona, for your unwavering support.

ZUSAMMENFASSUNG

Diese Arbeit befasst sich mit der Untersuchung entropischer Effekte während elektrochemisch induzierter Adsorptionsprozesse an Au(111)-Elektroden mittels elektrochemischer Mikrokalorimetrie. Durch diese Methode können kleinste Temperaturänderungen an der Elektrode gemessen und somit die Wärmeentwicklung sowie die Entropieänderungen bei Grenzflächenreaktionen bestimmt werden.

Untersucht wurden zwei Arten von Prozessen: die Adsorption von organischen Molekülen, Pyridin und Thymin, sowie die Über- und Unterpotentialabscheidung (OPD/UPD) von Blei. Bei der Adsorption von Pyridin wurde eine Reaktionsentropie von etwa –98 J mol^{-1} K^{-1} festgestellt, während für die Adsorption von Thymin eine Entropie von –60 J mol^{-1} K^{-1} ermittelt wurde. In beiden Fällen wurde der Hauptbeitrag zur negativen Adsorptionsentropie auf die Fixierung der Moleküle an der Au(111)-Oberfläche zurückgeführt. Dies deutet darauf hin, dass die Entropieänderung überwiegend durch die eingeschränkte Beweglichkeit der adsorbierten Moleküle bestimmt wird.

Bei der Untersuchung der Über- und Unterpotentialabscheidung von Blei zeigten die Ergebnisse, dass die Reaktionsentropie der Bulk-Abscheidung von Blei etwa 50 J mol^{-1} K^{-1} beträgt, bezogen auf Elektronenmengen. Diese Entropieänderung wird größtenteils durch die Desolvatisierung der Bleikationen dominiert, die sogar den Effekt der Fixierung der Bleiatome an der Oberfläche übertrifft. Im UPD-Bereich von Blei zeigte sich, dass die Reaktionsentropie und die Peltier-Wärme vergleichbar mit der der Bulk-Abscheidung sind, was auf das Fehlen von Nebenprozessen hinweist.

Table of Contents

CHAPTER 1 INTRODUCTION 1-4

1.1 Studied systems 1-5

CHAPTER 2 THEORETICAL BACKGROUND OF THE ELECTROCHEMICAL MICROCALORIMETRY 2-8

2.1 The electrochemical Peltier effect 2-8

2.2 Irreversible Heat Contribution 2-11

CHAPTER 3 EXPERIMENTAL ASPECTS OF ELECTROCHEMICAL MICROCALORIMETRY 3-13

3.1 Home-built Microcalorimeter 3-14
3.1.1 Construction of the Microcalorimeter and cell assembly 3-14
3.1.2 Preparation of the Solutions and the Electrodes 3-16
3.1.2.1 Preparation of the gold electrode 3-16
3.1.2.2 Preparation of the counter electrode 3-17
3.1.2.3 Preparation of the reference electrodes 3-17

3.2 Electrochemical and microcalorimetric experiments, conduction and evaluation 3-18
3.2.1 Cyclic voltammetry 3-18
3.2.2 Microcalorimetric pulse methods 3-20
3.2.3 Calibration and Evaluation 3-22
3.2.3.1 Determination of the accumulated heat 3-23
3.2.3.2 Determination of heat per charge and the calibration factor 3-25
3.2.3.3 Determination of the reversibly exchanged heat of a reaction of interest 3-27

3.3 Sources of errors in the measuring method 3-28

CHAPTER 4 ADSORPTION PROCESSES OF ORGANIC MOLECULES AT AN ELECTRODE SURFACE 4-30

CHAPTER 5 PYRIDINE ADSORPTION ON AU(111) FROM AQUEOUS SOLUTIONS 5-32

5.1 Results from the Microcalorimetric Measurements 5-37

5.1.1 Microcalorimetric pulse experiments 5-37
5.1.1 a Continuous current pulse experiments 5-37
5.1.1 b Potential pulse experiments 5-40

5.2 Molar Peltier Heats of Pyridine Adsorption on (111)-textured Au film from $NaClO_4$ 5-43

5.3 Determination of the experimental Reaction Entropy 5-46

5.4 Quantitative comparison of the experimental reaction entropy with the literature 5-47
5.4.1 Thermodynamic Cycle 5-47
5.4.2 Alternative simple model 5-51

5.5 Influence of the pyridine concentration on *Π* 5-53
5.5.1 Microcalorimetric investigations on different pyridine concentrations 5-54

5.6 Influence of the anion on pyridine adsorption 5-56

5.7 Conclusions 5-60

CHAPTER 6 THYMINE ADSORPTION ON AU(111) FROM AQUEOUS SOLUTIONS 6-62

6.1 Cyclic voltammetry 6-64

6.2 Results from the Microcalorimetric Experiments 6-66
6.2.1 Continuous current pulses 6-66

6.3 Molar Heat from the Microcalorimetric Measurements 6-70

6.4 Experimental Reaction Entropy of the process 6-72

6.5 Quantitative comparison of the experimental reaction entropy with the literature 6-73

6.6 Conclusions 6-78

CHAPTER 7 OVERPOTENTIAL AND UNDERPOTENTIAL DEPOSITION OF PB ON AU(111) – A MICROCALORIMETRIC INVESTIGATION 7-1

7.1.1 Pb overpotential deposition on a monolayer of Pb from aqueous solution 7-2

7.1.2 Pb underpotential deposition on Au(111) from aqueous solution 7-3

7.2 Results from Microcalorimetric Experiments 7-5
7.2.1 Cyclic voltammetry 7-5
7.2.1a Cyclic voltammetry of Pb_{OPD} 7-5
7.2.1b Cyclic voltammetry of Pb_{UPD}/Au(111) 7-7
7.2.2 Microcalorimetric experiments 7-11
7.2.2a Current pulses 7-11
7.2.2b Potential pulses 7-13
7.2.2c Continuous current pulses 7-15

7.3 Molar Peltier Heats of Pb OPD and Pb UPD in Perchloric Acid 7-19

7.4 Molar Peltier Heat and Reaction Entropy for Pb Overpotential Deposition 7-22

7.4.1 Quantitative comparison of the experimental reaction entropy with the literature 7-24

7.5 Molar Peltier Heat and Reaction Entropy of Pb UPD 7-26
7.5.1 Enthalpy change between Pb_{UPD} and Pb_{OPD} 7-27

7.6 Conclusions 7-28

CHAPTER 8 SUMMARY 8-1

REFERENCES 8-4

LIST OF ABBREVIATIONS 8-12

TABLE OF FIGURES 8-14

LIST OF TABLES 8-18

ACKNOWLEDGEMENTS 8-20

Chapter 1 Introduction

In the ongoing pursuit of sustainable energy solutions, there is a concerted effort to explore innovative renewable resources. Therefore, many researchers have focused on modifying solid surfaces, for example, by adsorbing organic molecules or depositing another metal on them, because these variations are crucial for enhancing the properties of energy-storage devices such as batteries, catalytic systems and sensors. A thorough comprehension of the electrochemical interfaces is needed to understand the mechanism of the previously mentioned adsorption processes.

Electrochemical reactions are often studied by conventional electrochemical methods like cyclic voltammetry, that is, by measuring the current or charge as a function of the applied potential. From the thermodynamic perspective, the variations of the Gibbs free energy are correlated to the state of the electrochemical system, characterized e.g., by the charge on the electrode. Measurements of other thermodynamic quantities, which might provide additional, independent information on such typically multivariate electrochemical systems, are rather scarce. The electrochemical microcalorimetry enables the determination of the entropy changes at an electrode, which provides an alternative, complementary quantity to the Gibbs energy, characterizing the electrochemical interface.

This thesis aims to investigate the adsorption phenomena at metal surfaces by using electrochemical microcalorimetry. Three prototypical systems for potential-controlled molecular adsorption on electrodes are considered: pyridine and thymine adsorption on (111)-textured Au-films. Later, the study is extended to over- and underpotential deposition of lead on (111)-textured Au-films from aqueous solutions.

The objective of this thesis is to provide answers to the following questions:

- What is the contribution of the configurational entropy to the stabilization of pyridine-surface structures?
- Can this study be extended to the adsorption of slightly larger neutral molecules, such as thymine, and what would be the entropic contribution to the stabilization of thymine-surface structures?
- What entropic contributions are involved, and how do they influence the free energy during over- and underpotential lead deposition on Au(111) from aqueous solutions?

1.1 Studied systems

Pyridine is subject of research in various fields of electrochemistry. On the one hand, pyridine has been identified as a cocatalyst for converting the greenhouse gas carbon dioxide into valuable fuels via the CO_2 reduction reaction. On the other hand, it was demonstrated that adsorbed pyridine significantly enhances the oxidation rate of formic acid on Au(111) [1]. In addition, pyridine can also serve as a ligand in the synthesis of nanoparticles with different morphologies [2].

Pyridine adsorption on metal surfaces in dependence on applied electrode potential has been extensively studied in the literature using electrochemical, spectroscopic, and microscopic techniques [3, 4]. All these studies reported potential-driven adsorption in two different molecule orientations on the metal surface. This feature makes pyridine a good model for molecular switches.

Despite the extensive research on pyridine adsorption on metal surfaces in previous studies, several knowledge gaps remain. For instance, the entropy change during pyridine adsorption on metal surfaces has not been resolved yet. Knowledge of the various entropic contributions is essential for gaining further insight into the adsorption process and therefore for building better models. The application of electrochemical microcalorimetry can render unbiased conclusions on the entropic contributions to the potential-driven pyridine adsorption. This finding motivates the investigation of pyridine adsorption on a Au(111) electrode using electrochemical microcalorimetry, as carried out in the present dissertation. This approach allows the determination of the Peltier heat, which is connected to the reaction entropy.

Given that this thesis successfully established the application of the electrochemical microcalorimetry setup for pyridine adsorption on Au(111), this method is transferred to a slightly larger molecule – thymine.

Similar to pyridine, various measurement techniques, including cyclic voltammetry, capacitive measurements, chronocoulometry, in-situ scanning tunnelling microscopy, surface-enhanced Raman spectroscopy, infrared spectroscopy, or X-ray photoelectron spectroscopy [5–7] have been applied to study the adsorption of thymine on metal surfaces such as Hg, Au(111), and Ag(111) under applied electrode potential. As with pyridine, the DNA bases adsorb in different molecule orientations on mercury and single-crystal electrodes, forming a well-ordered condensed monolayer [8].

Potential application of adsorbed thymine on metal electrodes is the usage as an additive in plating baths to improve the quality of the metallic coatings [9], as a modifier of the chemical nature of the metal electrodes [10], or as a highly selective sensor in biochemistry and analytical chemistry. In addition, the adsorption of thymine on single-crystalline metal electrodes is considered a model system for studying structural transitions in adlayers and the self-organization of molecules on surfaces [7]. To this end, in the scope of this thesis the thymine adsorption on Au(111) it is investigated using electrochemical microcalorimetry to elucidate the heat and the entropic contributions towards the adsorption process. The obtained insight can contribute to the construction of advanced theoretical models aimed at entropy estimates from electronic structure theory and could be important for the development of next-generation bio-nanosensors [10].

After studying the adsorption of organic compounds on Au(111), the focus is moved on to the electrodeposition, of lead, on Au(111) surfaces.

Lead deposition on Au(111) substrates is considered a model system in electrochemistry and surface science. The electrodeposition of a Pb monolayer on Au(111) is observed at potentials positive to the Nernst potential, which is also referred to as underpotential deposition, Pb_{UPD}.

It is noteworthy that the modification of electrode surfaces through underpotential electrodeposition of a metal, such as Pb and Bi, on noble metal surfaces can significantly increase the reaction rates for both small molecule oxidation and oxygen electroreduction in aqueous fuel cells [11, 12]. Therefore, the underpotential deposition of Pb has been extensively studied by electrochemical techniques, scanning tunneling microscopy, atomic force microscopy, low energy electron diffraction (LEED), and in-situ x-ray diffraction in order to understand the formation and structure of the UPD and to gain insight into the electrocatalytic activity.

In this thesis, the Pb_{UPD} is investigated by electrochemical microcalorimetry because the fundamental insights gained from knowing the heat generated during this process and the direct access to the rection entropy can be used to determine to which extent the deposition potential is entropy or enthalpy driven.

The work on the Pb_{UPD} on Au(111) is extended towards the overpotential deposition (OPD), known as bulk deposition of Pb. Here, the Pb is cathodically deposited on the same bulk metal from a solution containing Pb ions. The bulk deposition occurs when an overpotential is applied at potentials negative to the

reversible electrode potential of the Pb / Pb^{2+} couple in that solution. Knowledge of the Peltier heat of the OPD and access to the reaction entropy can be helpful in calculating the enthalpy involved in the deposition processes, as calibration system. By comparison of the Peltier heat of the Pb UPD with that of Pb OPD in the same electrolyte, a qualitative information on the contributions to the reaction entropy was obtained.

Chapter 2 Theoretical background of the electrochemical microcalorimetry

The electrochemical Peltier effect is the heat exchange at the electrode/ electrolyte interface when a reversible electrode reaction occurs. These heat effects can be measured by a microcalorimeter. Bouty was the first to experimentally observe the heat exchange at single electrodes in 1879 [13]. He used two copper-coated thermometers as electrodes for the electrochemical copper deposition and dissolution in $CuSO_4$ solution. The conclusion of his experiment was that at one of the electrodes, where the copper was deposited, the thermometer cooled down; that is, the deposition and dissolution resulted in cooling and warming, respectively. Bouty [13] recognized that this phenomenon at the electrode/electrolyte junction is analogous to the Peltier effect at junctions of solid conductors. Based on Eastman's theory of entropy transport, further theoretical description of the Peltier effect was developed by Wagner [14, 15] and Lange and co-workers [16, 17] and the basic concepts were later summarized, e.g., by Agar [18]. An overview of the method can be found in the work by Gottfried and Schuster [19].

Chapter 2.1, describes the thermodynamic principles of the Peltier effect, which are relevant to determine the reaction entropy based on a change in heat. Furthermore, the specific reversible and irreversible heat exchange measured by electrochemical microcalorimetry are discussed.

2.1 The electrochemical Peltier effect

To describe the electrochemical Peltier effect, an electrode made of metal M is immersed in a solution of the corresponding metal ion M^+ and a counterion A^-, shown in Figure *2-1*. In order to explain the processes at the electrode/ electrolyte interface, the boundary conditions of the interface are defined as follows: on the metal side, the interface is surrounded by a fictitious plane P so that all electrons flowing into and out of the interface pass through this plane. On the solution side, the interface is limited by H, a so-called "Hittorf reference plane" [18]. When current flows through the electrochemical cell, M^+ and A^- can migrate through this plane. The position of this plane can adjust to maintain a constant amount of solvent at the interface.

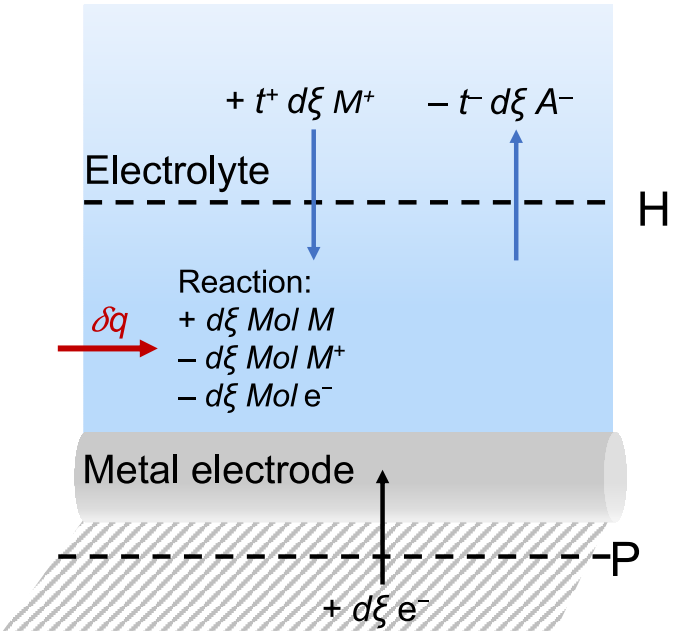

Figure 2-1 Schematic representation of the electrode/electrolyte interface for the ion and electron transport that takes place through the volume between boundaries P and H of the interface: $d\xi$ moles of the metal are produced at the metal electrode, resulting in a heat exchange δq with the environment. Figure modified and adapted from reference [19].

A small current reduces dξ mol of the metal ion, M^+, to M through the reversible reaction:

$$M^+ + e^- \rightarrow M$$

Consequently, $t^+d\xi$ ions of the reduced ion M^+ enter the interface and $t^-d\xi$ ions of the counterion A^- leave the interface, where t^+ and t^- are the respective Hittorf transfer numbers indicate the contribution of the ions to the charge transport.

For this process, the entropy changes of the interface, under isothermal and isobaric conditions is given by equation (1):

$$dS = (s_M - s_{M^+} + t^+ s_{M^+} - t^- s_{A^-} - s_{e^-})d\xi \qquad (1)$$

The entropy change, dS, as calculated from the changes in quantity of the components of the interface, is caused by the transport of ions and electrons into the interface, as well as by the reversibly exchanged heat, δq_{rev}. Thus, dS can alternatively be calculated from the entropy transported across the boundary of the interface during the electrochemical reaction.

The reversibly exchanged heat; that is, the amount of heat that is exchanged with the environment during the reversible process, is the so-called Peltier heat, Π:

$$\Pi = \frac{\delta q_{rev}}{d\xi} \qquad (2)$$

The transported entropy $\overline{\overline{S}}_i$, corresponds to the sum of the molar entropies of the transported species, s_i, and the ion-specific Eastman entropy of transfer $\hat{s}_i$:

$$\overline{\overline{S}}_i = (s_i + \hat{s}_i) \tag{3}$$

The Eastman entropy of transfer is the entropy that affects the solvation shell and the structure of the water when the ion is transported through the solution. Depending on whether the ion is “structure-making” or “structure-breaking,” an increase or a decrease in the entropy of the surrounding solution is observed. The resulting heat is absorbed in front of the ion and released behind it. Thus, the transport of ions through the solution leads to heat transport.

Since the entropy dS in equation (1), is state variable, it should correspond to the sum of the entropy change of the ion transport and the entropy resulting from the heat exchanged:

$$\left(s_M - s_{M^+} + t^+ s_{M^+} - t^- s_{A^-} - s_{e^-}\right) = \left(t^+ \overline{\overline{S}}_{M^+} - t^- \overline{\overline{S}}_{A^-} + \overline{\overline{S}}_{e^-} + \frac{\Pi}{T}\right) \tag{4}$$

Rearranging the above relationship gives:

$$\frac{\Pi}{T} = s_M - s_{M^+} - s_{e^-} - \left(t^+ \hat{s}_{M^+} - t^- \hat{s}_{A^-} + \hat{s}_{e^-}\right) = \Delta_R S - \Delta_T S \tag{5}$$

In equation (5), $\Delta_R S$ is the reaction entropy of an electrochemical reaction, and $\Delta_T S$ corresponds to the transport entropy defined by $t^{\pm}$. Note that the above equation refers to electrochemical equilibrium.

For a general electrochemical process consisting of i reactants, E_i, with stochiometric coefficient $|\nu_{E1}|$, $|\nu_{E2}|$, …, $|\nu_{Ei}|$ and j products, P_j, with stochiometric coefficient $|\nu_{P1}|$, $|\nu_{P2}|$, …, $|\nu_{Pj}|$, the reaction entropy, $\Delta_R S$, is defined according to equation (5):

$$|\nu_{E1}|E_1(aq) + |\nu_{E2}|E_2(aq) + \ldots + |\nu_{Ei}|E_i(aq) \longrightarrow |\nu_{P1}|P_1(aq) + |\nu_{P2}|P_2(aq) + \ldots + |\nu_{Pj}|P_j(aq)$$

$$\Delta_R S = \sum_j S_{P,j} - \sum_i S_{E,i} \tag{6}$$

From the absolute molar entropies at standard conditions, s_i^0 (pressure p = 101,325 Pa, activity a = 1, and temperature T = 298.15 K in aqueous solution), the molar entropies of the individual reactants, s_i, given by the respective composition of the electrolyte solution, can be calculated:

$$s_i = s_i^0 - R \ln a_i - RT \frac{\partial \ln a_i}{\partial T} \approx s_i^0 - R \ln a_i \tag{7}$$

The temperature dependence of the activity is neglected due to the small temperature changes (all measurements are done at room temperature, and there are only minute, μK, temperature changes in one pulse). In this work, the activity for the chapters on pyridine and thymine adsorption is approximated with the concentration. For the chapter on lead over- and under-potential deposition it is taken into consideration and calculated using *PhreeqC Interactive*.

$$\Delta_R S^0 = \sum_j s^0_{P,j} - \sum_i s^0_{E,i} \tag{8}$$

The transport entropy, $\Delta_T S$, can be calculated by adding the Eastman entropies of transfer and the transfer numbers of the individual ions, namely by using equation (9):

$$\Delta_T S = \sum_i \left(\frac{t_i \hat{s}_i}{z_i} \right) \tag{9}$$

The Hittorf transfer numbers, t_i, can be estimated according to the following equation (10):

$$t_i = \frac{\lambda_i^0 |z_i| c_i}{\sum \lambda_i^0 |z_i| c_i} \tag{10}$$

In equation (10), λ_i^0, z_i, and c_i denote the molar limiting conductivities, charge, and concentration of the individual ions, respectively.

2.2 Irreversible Heat Contribution

For the process to be reversible, the system must be constantly in equilibrium, and we know from practice, that it is infinitely slow. Thus, when determining the heat contributions experimentally, in addition to the rise of the reversible heat, irreversible heat contributions arise from the following two factors:

i. Electrochemical processes only take place if an overpotential $\eta = E - E_0$, corresponding to the excess electrode potential with respect to the equilibrium potential E_0, is applied. The applied overpotential is the cause for the observation of a polarization heat, q_{pol}, which is proportional to the overpotential and charge flow:

$$\delta q_{pol} = - zF|\eta| \, d\xi \tag{11}$$

In equation (11), z and F indicate the number of electrons involved in the reaction and the Faraday constant, respectively.

ii. The current flow through the electrolyte creates what is known as Joule heat due to the electrolyte resistance:

$$\delta q_{Joule} = - RI^2 dt \tag{12}$$

In equation (12) R, I, and dt are the resistance of the electrolyte, current, and time interval, respectively.

Therefore, the total irreversible heat exchange during the electrochemical reaction with the environment is given by:

$$\delta q_{irrev} = - zF|\eta|d\xi - RI^2 dt \tag{13}$$

By combining equations (2) and (13) the total heat exchanged is:

$$\delta q_{exch} = \Pi \, d\xi - zF|\eta|d\xi - RI^2 dt \tag{14}$$

In equation (14) dξ is determined by the amount of charge, dQ, as specified by the following relationship:

$$d\xi = \frac{dQ}{zF} \tag{15}$$

The combination of equations (14) and (15) leads to the following expression:

$$\frac{dq_{exch}}{dQ} zF = q_m = \Pi - zF|\eta| - RI^2 dt \tag{16}$$

Note that the ratio $\frac{dq_{exch}}{dQ}$ is exactly what we measure by the application of electrochemical microcalorimetry. This term linearly scales with the applied overpotential, η. The process is reversible at zero overpotentials, and the ratio corresponds to the entropy change of the electrochemical process.

In experiments in which different overpotentials are applied, the entropy change can be estimated by interpolating q_m to the values up to an overpotential of zero from the plot of the conversion-normalized heat input over the overpotential.

In the following chapter, firstly the experimental setup (in which the exchanged heat is measured) and the measuring principles of the home-built electrochemical microcalorimeter are described. After that, the used measurement methods in this work are explained by showing a typical measurement result and its calibration.

Chapter 3 Experimental Aspects of Electrochemical Microcalorimetry

The results obtained for this thesis are based on cyclic voltammetric and microcalorimetric measurements. Both methods investigate electrochemical processes. Cyclic voltammetry provides the change of the current depending on the potential of an electrode and, in this work, is used for surface characterization. Reactions without an external current flow cannot be characterized by cyclic voltammetry since this method is limited to charge-dependent processes. Electrochemical microcalorimetry enables the determination of the reaction entropy of the electrochemical half-cell reaction at the electrolyte-electrode interface.

The pioneer of experimental determination of the Peltier heat is Bouty [13], as mentioned at the beginning of the previous chapter. The subsequent work from Ozeki and co-workers [20] on measuring the Peltier heat of various electrochemical reactions was limited to processes associated with high electrochemical conversions. Boudeville [21] measured the resulting temperature changes in the range of millikelvin with liquid thermometers and thermistors.

Schuster et al. [22, 23] built a microcalorimeter based on thin electrodes and a pyroelectric PVDF film. Due to the high thermal conductivity, all the heat generated at the working electrode is immediately and entirely detected by the pyroelectric sensor. Therefore, with this construction, processes with minimal heat conversions can be measured in the range of a few µK. In addition, the influence of the Joule heat is reduced by applying short 10 ms potential pulses. For some experimental conditions, these pulses can be longer, up to 40 ms. Since the Joule heat is generated due to the electrolyte resistance when current flows in the electrolyte, the resulting heat is not transported to the electrode on the short experimental time scale [24]. Therefore, the Joules heat can be neglected. The sensitivity was further improved by replacing the PVDF film with $LiTaO_3$ single crystal as a pyroelectric sensor [25]. Due to the crystallographic properties of $LiTaO_3$ [26], it has a permanent electrical dipole moment, meaning that if a reaction causes a temperature change, the surface of the sensor becomes electrically charged, which results in a potential difference between the top and the bottom of the sensor. This change is recorded by metallic electrodes of eq. Au. The associated current flow serves as a direct measure of the temperature change caused by the electrochemical process.

In the following subchapter, the setup construction used in this work and the preparation of the solutions and electrodes are described. Section 3.2, presents the measuring method, cyclic voltammetry, microcalorimetric pulse experiments, showing typical measurement results from this work. Lastly, the calibration and evaluation procedure are presented.

3.1 Home-built Microcalorimeter

For this work, a home-built microcalorimeter based on the work of Frittmann et al. [25] was used. The experimental setup and the cell construction are described in the following sections.

3.1.1 Construction of the Microcalorimeter and cell assembly

The experimental setup is shown in Scheme *3-1*. A sensor is mounted in the central top area of a brass cylinder. A $LiTaO_3$ sheet is used as a sensor. Gold is deposited on the both sides of the sensor, allowing good electrical conduction. One side of the sensor is grounded, and the other is connected to the charge amplifier. On the top side of the sensor, a small drop of heat-conducting oil is applied, and directly after, a 50 µm thick sapphire plate is placed to help reduce the mechanical tension. On top of the sapphire plate again, a small drop of oil is applied, and the working electrode is sited. The application of the heat-conduction oil improves the thermal contact. For the electrical contact, a brass ring and a brass plate ring with a central, circular recess of 7 mm are positioned on the top of the working electrode. A Viton O-ring with an inner diameter of 5 mm is placed in the recess to seal the cell and the electrolyte, providing a working electrode area of around 0.2 cm^2. This O-ring was previously cleaned in Caro's acid, thoroughly rinsed with ultrapure water, and dried.

The cell is made of polychlorotrifluoroethylene, Kel-F, with a capacity of ~ 300 µL and a circular recess of the same size as the brass ring. Before each assembly, this cell is cleaned in Caro's acid, thoroughly rinsed with ultrapure water, dried and afterwards screwed on top of the brass spring. In order to increase the thermal conductivity between the sensor-cell structure, the air is removed by a rotary vane pump (the vacuum is in order of 10^{-1}–10^{-2} mbar). After several minutes the argon flow is turned on, the counter and the reference electrodes are placed, as well as the solution is filled, and the system is closed by screwing a cylinder-brass cover. For all the experiments, except the calibration, the solutions were bubbled with Ar for about

30 min for the dissolved oxygen to be removed. The upper side of this cover has a removable lid, which can be adjusted for the level of openness. The cyclo-voltammogram is usually first recorded under argon flow. Later, the argon flow is turned off, the top of the brass cylinder is tightened, and the whole setup is covered with a wooden cover, isolated with sponge-rubber sealing from the inner side to keep the air convection and temperature fluctuations minimal. The entire setup is placed on a wooden platform with rubber legs, so the vibrations from the table and the ground would not affect the measurements.

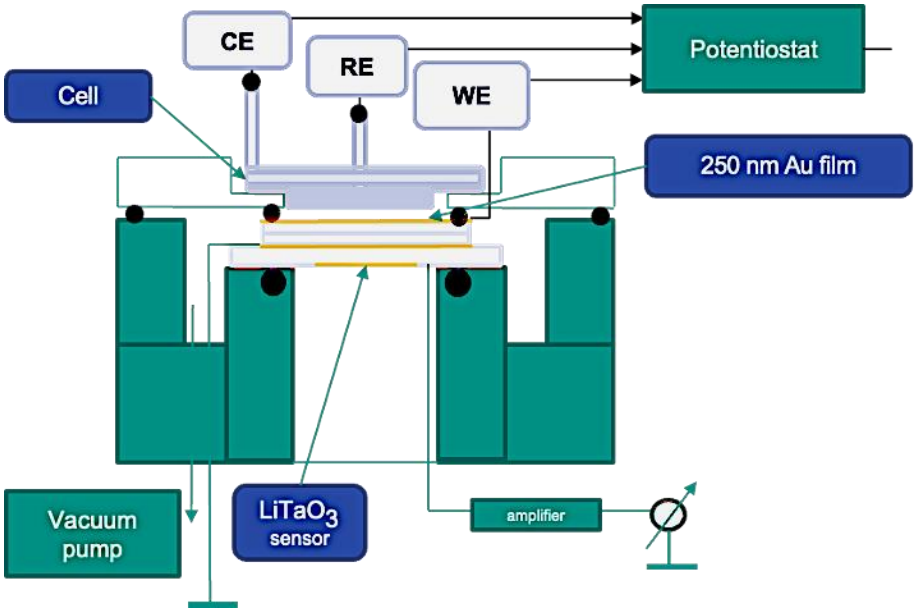

Scheme 3-1 Schematic illustration of the microcalorimeter. At the central area the pyroelectric, $LiTaO_3$, sensor is mounted. On the one side it is grounded and the other side is connected to the electronics. Above it, the working electrode (WE) is placed, and on the top of it the polychlorotrifluoroethylene, Kel-F cell is positioned. The thermal contact between them is improved by removing the air between them with the vacuum pump. The CE and RE are the counter and the reference electrode, respectively.

For the conduction of the microcalorimetric experiment, the cell is assembled as described above. As indicated, the cyclo-voltametric experiments were recorded under Ar-flow in situ in the calorimeter cell. In section 3.2.1, the cyclo-voltammetric measurements are described by using the calibration solution, $K_3[Fe(CN)_6$ / $K_4[Fe(CN)_6]$, as an example. After the CV measurements, the Ar flow is stopped, the lid is tightened, and the setup is closed with a wooden cover. Afterwards, one proceeds with the microcalorimetric pulse measurements, explained in section 3.2.2.

After the experiments, the brass lid was opened and replaced with a glass-brass lid to perform the laser heating measurements. Before the laser pulses, the RE

was removed from the pathway to ensure that the sensor detected the heat from the laser.

Finally, after the laser pulses, the electrolyte solution was removed, the cell was cleaned with ultrapure water several times, and filled with the calibration solution, 0.1 M $K_3[Fe(CN)_6]$ / 0.1 M $K_4[Fe(CN)_6]$. A Pt-wire was attached as a reference electrode, and the calibration measurement could start.

3.1.2 Preparation of the Solutions and the Electrodes

All vessels and containers used for preparing the solutions were cleaned before with Caro's acid (3:1 mixture of 96% sulfuric acid and 30% hydrogen peroxide) and then carefully and thoroughly washed with ultrapure water (≥ 18.2 MΩcm, *Sartorius*, Arium). All aqueous solutions were prepared with ultrapure water. A list of all chemicals used, including their manufacturers and purity levels, can be found below.

- Pyridine, 99.5%, ultrapur (Alfa Aesar)
- Thymine, 99% (Thermo Scientific)
- $PbCO_3$, 99.9% (Alfa Aeser)
- solid $NaClO_4$, 99%, for analysis (Acros Organics)
- $HClO_4$ 70%, suprapur (Merck)
- $NaPF_6$, 99+% (Alfa Aesar)
- NaF, 99.5 % (Merck)
- HNO_3, 65% suprapur (Merck)

3.1.2.1 Preparation of the gold electrode

A Gold-sapphire surface was used as a substrate to study the pyridine and thymine adsorption and the Pb over- and underpotential deposition. To prepare the gold electrode, 50 µm thick sapphire sheets were placed inside a Teflon holder, cleaned with Caro's acid, thoroughly rinsed with ultrapure water, and put for 15 min in boiling ultrapure water. Afterwards, they were carefully taken from the Teflon holder with ceramic tweezers and dried with a butane gas flame. The dried sapphire plates were positioned in a holder and sited in a UHV vapour deposition chamber where a 250 nm thick' layer of gold was deposited on them. Before the gold deposition, a 2 nm thick Cr layer, as an adhesion layer, was vapour-deposited for the pyridine and thymine adsorption experiments. Before use, the electrode was again flame-annealed with a

butane flame. For this work, (111)-textured Au-films were used, which are referred as Au(111) electrodes, in the following chapters.

3.1.2.2 Preparation of the counter electrode

For all experiments in this work, a 0.5 mm thick Pt wire was used as a counter electrode. The wire runs in a ring shape around the outer edge of the recessed cell to ensure the largest possible surface area. Before use, the wire was cleaned with Caro's acid and thoroughly rinsed with ultrapure water.

3.1.2.3 Preparation of the reference electrodes

A 0.5 mm thick Pt wire was used as a pseudo-reference electrode for pyridine and thymine adsorption experiments. It was cleaned as previously described before being placed in the cell.

For a better representation of the Peltier heat versus the electrode potential for pyridine adsorption, the potential shift is corrected for the electrode potential versus the SCE electrode even though it was measured against the Pt pseudo reference electrode. That is done by correlating the main peak, A2, from the differential capacitance, *C*, obtained from the relationship between the difference of the current in the consecutive current pulses, from the continuous current pulses' experiments, and the resulting potential jump, with the literature capacitance data taken from [27].

Lastly, a Pb wire was used as a reference electrode for the lead under- and overpotential deposition experiments. Since the Pb wire is sensitive to air and oxidizes quickly, it was kept in ultrapure water in an exicator when not used. Before assembling it in the cell, the wire was immersed in 65 % nitric acid for 10-15 s and rinsed with ultrapure water. After cleaning, it was immediately assembled in the cell.

Each metal wire is bent so its tip can be closer to the WE. This helps to reduce the voltage drop in the electrolyte solution caused by electrolyte resistance.

3.2 Electrochemical and microcalorimetric experiments, conduction and evaluation

To conduct the electrochemical microcalorimetric experiments, the cell is assembled as previously described. As noted, the cyclic voltammetry experiments were performed under an argon flow. For illustration, the cyclic voltammetry measurements for the calibration solution, $K_3[Fe(CN)_6]$ / $K_4[Fe(CN)_6]$, are explained here as an example. After completing the CV measurements, the argon flow is stopped, the lid is securely tightened, and the setup is sealed with a wooden cover. The microcalorimetric pulse measurements, detailed in section 3.2.2 of this chapter, are then carried out.

After the experiments, the brass lid was opened and replaced with a glass-brass lid to perform the laser measurements. Before the laser pulses, the RE was removed from the pathway to ensure that the sensor detected the heat from the laser.

Finally, after the laser pulses, the electrolyte solution was removed, the cell was cleaned with ultrapure water several times, and filled with the calibration solution, 0.1 M $K_3[Fe(CN)_6$ / 0.1 M $K_4[Fe(CN)_6]$. A Pt-wire was attached as a reference electrode, and the calibration measurement could start.

3.2.1 Cyclic voltammetry

Cyclic voltammetry is one of the most common methods for receiving information about the reactivity of an electrochemical system. The principle is based on measuring the current response as a function of the applied potential. The potential is swept linearly with time, from an initial value to a final potential and then back to the initial potential. That allows investigation of the influence of the potential and time on the current over a wide potential range.

In Figure *3-1*, the cyclic voltammogram, CV (current-potential curve), of the calibration solution 0.1 M $K_3[Fe(CN)_6]$ / 0.1 M $K_4[Fe(CN)_6]$ on Au(111) surface is shown as an example to illustrate a typical CV measurement result.

Starting from an initial cell potential, in this case, 0 V, where no electrode processes should take place (without an external current flow, known as open circuit potential, OCP), the potential reduces in the negative direction, with a fixed scanning

speed, in this case, that is 50 mV/s. If electrochemically active compounds are present in the investigation system, a cathodic current peak arises at a specific potential corresponding to the species reduction. From Figure 3-1, the peak with a minimum at –0.15 V can be attributed to the reduction of $[Fe(CN)_6]^{3-/4-}$. With the further decrease of the potential, the current increases towards a limiting current, which is attributed to the diffusion limitation of the reaction. After reaching the cathodic potential limit, in this case, at –0.37 V, the potential sweep direction is changed, and the anodic current is recorded. In this region, a peak occurrence corresponds to the oxidation of the reduced species. In the example, an anodic peak occurs at 0.15 V due to oxidation. With further increase in potential, the anodic limit is achieved at 0.37 V, and after that, the potential is reversed in a negative direction. The measurement of those cycles is repeated until the current potential curve stabilizes.

By changing the scanning speed, the CV provides information about the kinetic behaviour of the electrochemical process.

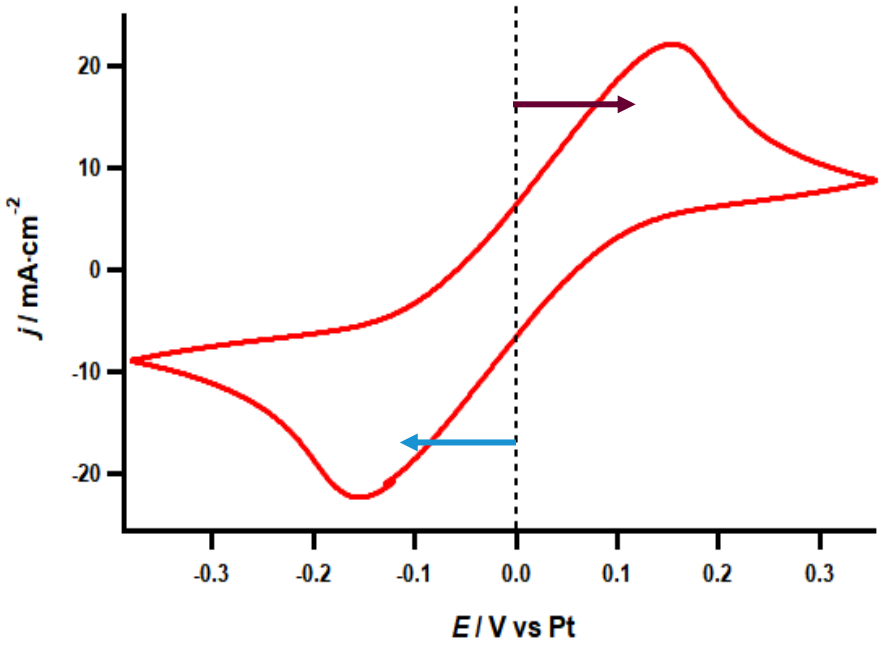

Figure 3-1 Cyclic voltammogram of 0.1 M $K_3[Fe(CN)_6$ / 0.1 M $K_4[Fe(CN)_6]$, recorded with a rate of 50 mV/s, on (111)-textured Au as working electrode, Pt wires as counter and reference electrodes, first scan. The black dashed line indicates the position from where the pulses were applied. Bordeaux arrow indicates the direction of the anodic (positive) pulses and the blue arrow of cathodic (negative) pulses.

In this work, the CVs are recorded at the beginning of each measurement to obtain information about the system's state under investigation and for surface characterization. This measuring method is also used as a cleaning or activation step

necessary for preparing the Pb surface for Pb OPD and characterizing the electrode surfaces.

3.2.2 Microcalorimetric pulse methods

Measurements of the (ir-)reversibly exchanged heat during the electrochemical processes in a half-cell are done by applying short, 10 ms pulse microcalorimetric experiments. Three types of experimental procedures, potential, current, and continuous current pulse procedures, can be used to achieve system deflection from equilibrium.

- Potential pulses: the 10 ms long potential pulse is applied starting from an initial potential state with varying potential amplitude. In Figure *3-2*, an exemplary potential pulse within the first 100 ms for the system of 1 mM pyridine in 0.1 M $NaClO_4$ is shown. The pulse begins at t = 10 ms after the start of the data recording. After the pulse, at t = 20 ms the cell is switched to open circuit potential (OCP) for 500 ms and then regulated back to the initial potential. In the Figure the respective transients are shown; the recorded potential (blue transient at the upper panel), the current (black, transient in the middle), and the temperature (red for a positive pulse and light blue for a negative) transients.

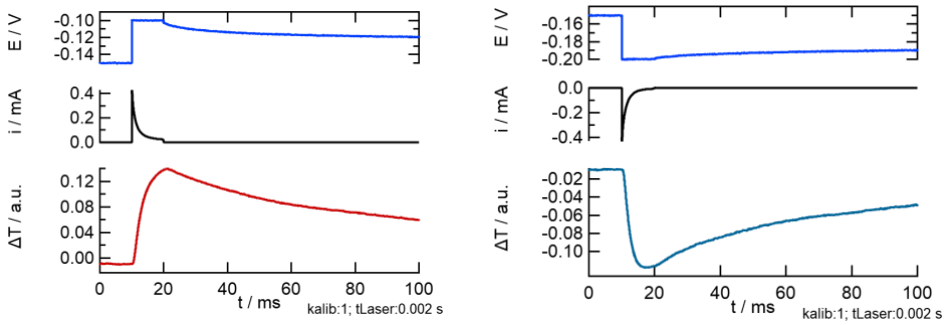

a. Positive potential pulse with amplitude 0.05 V, for anodic direction, pyridine adsorption

b. Negative potential pulse with amplitude –0.05 V, for cathodic direction, pyridine desorption

Figure 3-2 Potential (blue), current (black), and temperature (red A. and light-blue B.) transients of two 10 ms potential pulses of 1 mM pyridine adsorption (a; +0.05 V) and desorption (b; –0.05 V) on Au(111) in 0.1 M $NaClO_4$ supporting electrolyte.

Data is recorded for 1 s, but since the heat input for the processes considered in this work is completed within 100 ms, the data typically is shown until 100

ms. For the same amplitude, a series of several positive and negative pulses is applied, and then the amplitude is increased.

- Current pulses, either at a set potential state (i) or/and continuous (ii):

i. When applying current pulses, the cell is initially in OCP mode, i.e. I = 0. Starting from the OCP, 10 ms current pulses with a certain pulse amplitude are applied. After the end of the pulse at t = 20 ms, the cell is switched to OCP for the remaining data-recording period. When the data recording period ends, the cell rests in OCP for 1 s, and the next pulse starts. A series of alternating positive and negative current pulse amplitudes are applied. this measurement method is used to calibrate and investigate the Pb overpotential deposition in chapter 7. In Figure *3-3* below, exemplary current pulses from the experiment of the calibration system 0.1 M $K_3[Fe(CN)_6$ / 0.1 M $K_4[Fe(CN)_6]$ on Au(111) are shown. It can be seen that the maximum or minimum of the temperature transient coincides with the end of the pulse, and afterward, they relax towards zero.

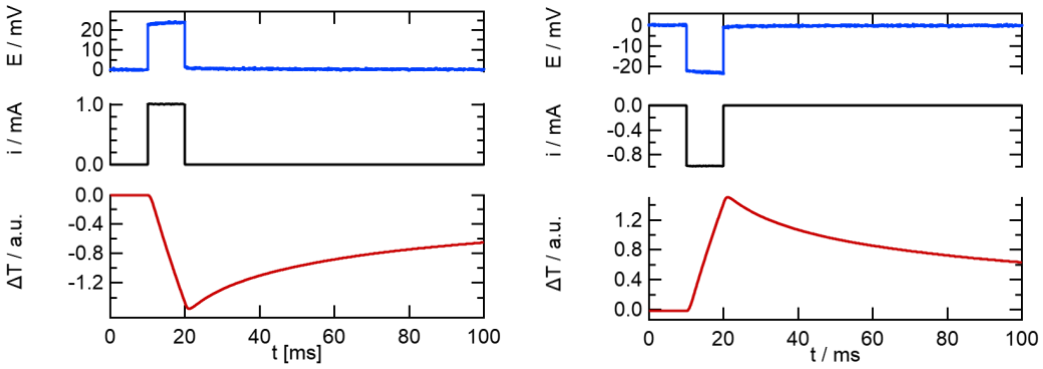

a. Positive current pulse with amplitude 0.001 A in anodic direction, for the oxidation reaction.

b. Negative current pulse with amplitude –0.001 V in cathodic direction, for the reduction reaction.

Figure 3-3 Potential (blue), current (black), and temperature (red) transients of two 10 ms current pulses for Fe complex oxidation (a; current amplitude of 0.001 A), and Fe reduction (b; current amplitude of –0.001 A) on Au(111). As solution is used 0.1 M $K_3[Fe(CN)_6$ / 0.1 M $K_4[Fe(CN)_6]$.

ii. The third experimental method is an application of a series of continuous current pulses. This method was used in all experiments except the calibration and the investigation of the Pb overpotential deposition. Starting from a defined potential, a series of 10 ms long current pulses are applied.

The cell is switched to OCP for 1 s, after each consequent current pulse. The subsequent current pulse starts from OCP. The rest potential is determined by the change in equilibrium state from the previous pulse. This allows an extensive potential range to be examined. For the experiments in this work, the starting potential is chosen outside the area of interest. Then, stepwise, the pulses are applied in the whole region, covering the area of interest. After this set of pulses is done, the current pulse amplitude is reversed. Exemplary pulses are shown in the chapter 5, section 5.1.1.

The crucial information from the microcalorimetric measurements is the change in the electrode's temperature. However, from the temperature transients, no absolute value can be given for the total heat exchanged after the end of the reaction. Therefore, the system is calibrated and the following subchapter 3.2.3 is describing the calibration and the evaluation of the results.

3.2.3 Calibration and Evaluation

Calibration of the measured temperature change data is needed because it is of interest to determine the reversibly exchanged heat for a certain electrochemical process. The calibration is done in two ways.

First, the measured temperature change data is reconstructed by laser pulses (in the text below it is written as “laser calibration”) because Bickel and Frittmann [24, 25] showed that in order to determine the heat input when the temperature changes, the heat response can be described as the sum of individual heat inputs. The determined heat would be named in the text as total, or accumulated heat, q, in arbitrary unit (a. u.).

Second, to get the heat per mol, q_{mol} (in unit $\frac{J}{mol}$), the accumulated heat needs to be divided by the pulse charge (leading to heat per charge, q_c in unit $\frac{a.\,u.}{C}$) and multiplied with the calibration factor. The calibration factor is obtained for each experiment individually. It can be determined by dividing the Peltier heat for an already known redox reaction (in this case, the $K_3[Fe(CN)_6$ / $K_4[Fe(CN)_6]$ that is 45,1 $\frac{kJ}{mol}$ [21]) with the extrapolated heat, at zero over potential, per charge for the same system, determined from the microcalorimetric measurements.

3.2.3.1 Determination of the accumulated heat

The experimental temperature response can be reproduced by using precisely defined "pulse responses":

$$T(t)= \sum_{i=1}^{n} A_i \, P(t-\Delta t\, i) \qquad (17)$$

Equation (17) presents the experimental temperature profile, T(t), that can be reproduced by *n* laser pulses, with pulse duration Δt and adjusted amplitude A_i of the pulses corresponding to the experimental one.

The transients of the defined pulse responses can be obtained by heating the electrode with 2 ms-long laser pulses. Due to the constant energy input during the laser pulse, these pulses lead to the heating up of the sensor while the electrode is irradiated. Considering the temperature relaxation due to heat dissipation in the electrolyte, the cell needs to be filled with ultrapure water during the laser pulse. For that, in all cases, after the primary measurement, the electrolyte was removed from the cell, and the reference electrode and the cell were rinsed several times with ultrapure water before being filled with it for the laser pulses. In the example of pyridine adsorption, by applying a 2 ms laser pulse, a maximum temperature change transient is at t = 12 ms, which can be seen in Figure *3-4* below. The maximum of the temperature change is specific for each cell assembly.

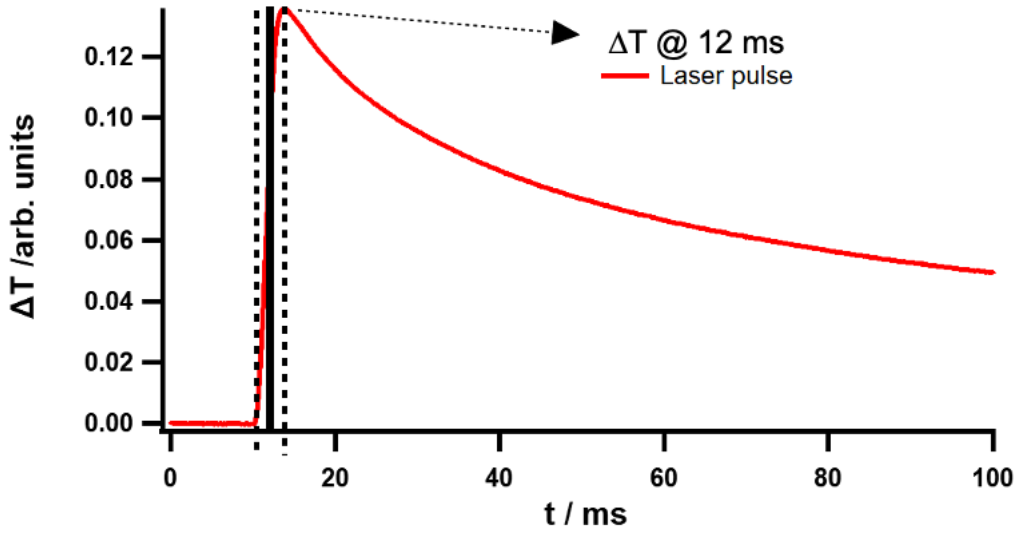

Figure 3-4 Temperature transient of a 2 ms long laser pulse (the red line) in ultrapure water on Au(111). Represented by the vertical dashed lines, the pulse starts at t = 10 ms and ends at t = 12 ms. The maximum temperature change occurs at the end of the pulse, t = 12 ms.

The total heat is obtained when the amplitudes of the individual laser pulses (A in equation (17)) are added over time. The total heat is called "accumulated heat", q,

in order to avoid later confusion. The amplitudes of the individual 2 ms laser pulses describe the average heat flux in 2 ms interval.

In Figure 3-5, exemplary transients for the redox reaction $K_3[Fe(CN)_6]$ / $K_4[Fe(CN)_6]$ on Au(111) are shown. Figure 3-5 A presents for the oxidation reaction, the signal-transients from a positive, anodic, current pulse, and B presents for the reduction reaction, the signal-transients from a negative, cathodic, current pulse. The signals are calibrated with the laser, where, in this case, 20 reconstructed pulses were taken for the calibration, and several new features are seen in the panels: the heat flux (presented with red circles in the second panel), the reconstructed temperature transient (presented with a black line in the third panel) and the accumulated heat (the ink-blue line in the third panel). In this example, the accumulated heat is determined until t ~ 50 ms. It is worth mentioning that a determination of the accumulated heat is possible until any time within the data recorded up to 1 s. However, as the measurement time increases, the accumulated heat becomes less precise because the higher the thermal drift, the higher the error. Therefore, all measurement results are presented on a scale of 100 ms.

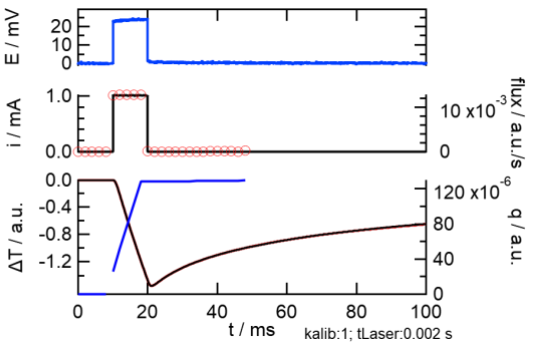

a. Current pulse, 0.001 A, for the oxidation reaction $K_3[Fe(CN)_6]$ / $K_4[Fe(CN)_6]$, fitted with 20 laser pulses.

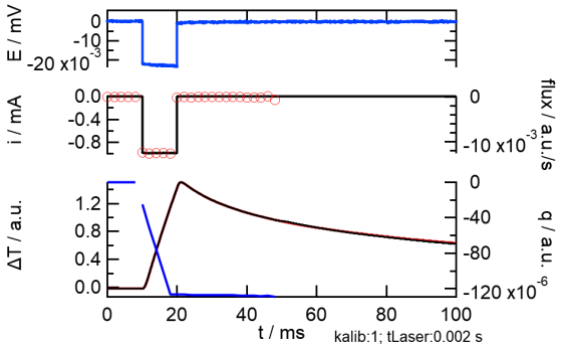

b. Current pulse, –0.001 A, for the reduction reaction $K_3[Fe(CN)_6]$ / $K_4[Fe(CN)_6]^+$, fitted with 20 laser pulses.

Figure 3-5 Potential, current, temperature transients, as well as the laser adjustment (black line in the third panel), the accumulated heat (ink-blue line in the third panel) and the heat flow (red dots in the second panel) of two 10 ms current pulses for Fe oxidation (a. anodic current amplitude of 0.001 A), and Fe reduction (b. cathodic current amplitude of –0.001 A) on Au(111) starting from the OCP at around 0 V. As solution is used 0.1 M $K_3[Fe(CN)_6]$ / 0.1 M $K_4[Fe(CN)_6]$.

The accumulated heat reaches its maximum at the end of the pulse at t = 20 ms and then continues with a flat top. It can be noted that all the heat was transferred

within the pulse duration, and that the reaction is completed within these 10 ms by looking at the heat flux, the reconstructed temperature and the steadiness of the accumulated heat after the pulse (third panel from Figure 3-5).

In case of a bad heat conduction (from a poor thermal contact) or a slow reaction continuing after the current flow, the maximum on the temperature transient will not be at t = 20 ms, and the heat flow will not be zero after the end of the pulse. Instead, the pulses will be delayed and the accumulated heat will not be constant after reaching t = 20 ms. If the heat is delayed by poor thermal contact, there would be a delay in the measured temperature transient but not in the reconstructed heat flux and the accumulated heat. This is an important indication because it allows us to know whether the process was completed by the end of the pulse, or there is an additional reaction that is slow.

In short, with the laser calibration a correct determination of the accumulated heat in absolute units is obtained, and it can be distinguished if the heat transported through the sensor-electrode structure originates from fast or slow electro(chemical) processes.

3.2.3.2 Determination of heat per charge and the calibration factor

To obtain the value for the heat per charge and the calibration factor from the simulated temperature transients, the accumulated heat, q, exchanged with the environment is firstly normalized to the charge, ΔQ, that is transferred during the pulse.

$$q_C = \frac{q}{\Delta Q}$$

In Figure 3-6 is shown the dependency of the heat per charge from the different pulses versus the respective applied overpotential for the calibration solution. The red dot represents the interpolated heat per charge at overpotential, η = 0 V, and its value is $q_C = 1.25\ 10^6 \frac{\text{a. u.}}{\text{C}}$. The positive sign indicates that the heat per charge is in anodic direction, meaning that positive pulse leads to heating.

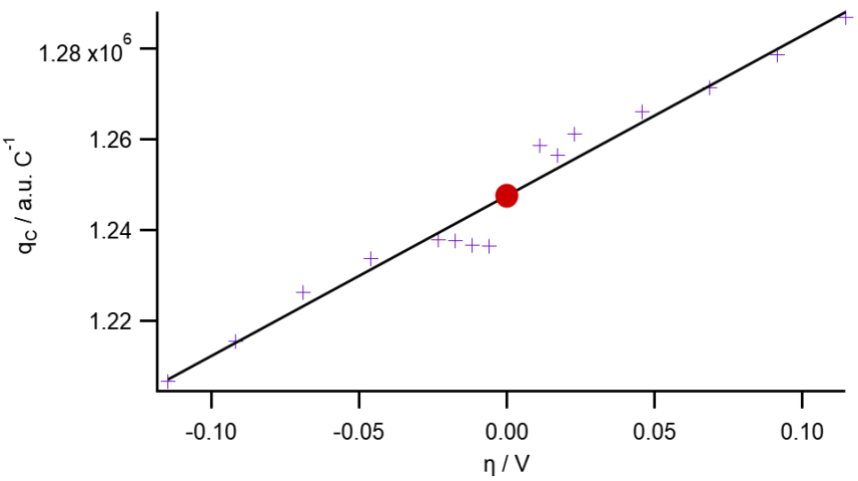

Figure 3-6 Plot of the heat per charge versus the overpotential from current pulses in 0.1 M $K_4[Fe(CN)_6]$ / 0.1 M $K_3[Fe(CN)_6]$ solution on Au(111). Interpolating the values to η = 0 V provides the reversible heat per charge, q_c (red dot). The calibration factor is obtained by dividing the Peltier heat for the redox reaction by qc.

Accordingly, the calibration factor is the ratio of the Peltier heat of the redox reaction, $K_3[Fe(CN)_6]$ / $K_4[Fe(CN)_6]$ and the q_C. To specify the value obtained in absolute units, the set-up is calibrated with 0.1 M $K_3[Fe(CN)_6]$ / 0.1 M $K_4[Fe(CN)_6]$, as already indicated several times, because for this solution, the electrochemical reaction results in a rapid electron transfer with high conversions, and the Peltier heat of this reaction is already known from the literature, –45.1 kJ mol^{-1} [28]. That means –45.1 kJ $mol^{-1}$for the reduction reaction in the cathodic direction. For the oxidation reaction, the value of the Peltier heat would be +45.1 kJ mol^{-1} for the anodic direction. This allows a direct comparison of the theoretical value with the experimentally determined one.

3.2.3.3 Determination of the reversibly exchanged heat of a reaction of interest

To obtain the reversibly exchanged heat for the electrochemical process of interest from the microcalorimetric pulse measurements, after the EC experiment a “laser calibration” is done, as described in section 3.2.3.1. Afterwards, the accumulated heat, q, exchanged with the environment as previously, is normalized to the charge, *Q*, that is transferred during the pulse, and lastly, this heat per charge, is multiplied with the calibration factor. The result of this multiplication is the so-called molar heat, q_{mol}, in absolute unit kJ mol^{-1}. The molar heat, q_{mol} is related to the heat of 1 mol of electrons flow in the outer cell circuit; the extent of the reaction, dξ, as defined in equation (15), $d\xi = \frac{dQ}{zF}$ is a function of the charge, and the contributions from the Joule’s heat z F can be neglected due to the short experiment times. From here, the molar heat, q_{mol}, would be:

$$q_{mol} = \frac{dq_{exch}}{dQ} z\,F = (T\Delta_R S - Q^*) - z\,F\,|\eta| \qquad (18)$$

Note that this equation is the same as equation (16) with slight rearrangement. Q^*represents the contribution from the heat of transport or the transport entropy, $\Delta_T S = \frac{Q^*}{T}$ [16, 29].

By measuring the heat at different pulse amplitudes and/or overpotentials, the molar heat values can be plotted against the respective overpotential. In order to eliminate the contribution of the polarization heat, the molar heat is interpolated to η = 0 V. The resulting value of the molar heat, now, corresponds to the reversibly exchanged heat during the electrochemical process, namely to the Peltier heat, that is directly connected to the reaction entropy.

3.3 Sources of errors in the measuring method

Microcalorimetric measurements are prone to errors due to various influences, which can be divided into systematic and statistical errors. These errors need to be considered for precise validation of the results.

The systematic errors are due to differences in the sensor-electrode assembly between the experiments. This error influences the thermal contact between the sensor and the working electrode and originates from several impacts. First would be the sensor assembly in the brass cylinder; while soldering it into the base, every slight tension from the wires can impact the quality of the heat transients. However, since not every measurement has a new sensor assembled before, this error can have the same impact on several experiments. Second, the assembly of the sensor-electrode, namely, delayed heat input, can occur depending on how precise the design is due to poor heat transfer between the electrode and sensor. This error, as discussed in the section above, can be detected. However, the adjustment of the temperature response using laser pulses is less precise, and the longer the delay of temperature maximum is, the poorer the thermal contact that deviates between comparable measurements from two different experiments. Third, the surface of the working electrode: since for every experiment, a new working electrode is used, the different surface roughness can influence the active surface area and thus the temperature transient in two different experiments, meaning that the size of the temperature transient will be different. It is worth noting that systematic error can arise from applying the thermal-conductive oil, meaning that if there are micro-bubbles formed between the sensor and the sapphire plate or sapphire plate and the working electrode, the thermal signal can drift within pulses. To account for the different thermal contact in the experiments the calibration is carried out whenever the sensor-WE setup is reassembled.

An experiment's statistical errors are due to external influences such as changes in pressure, temperature, and mechanical noise from the environment, and affect the temperature response of the sensor. As previously mentioned in section 2.1, the whole setup is placed in a wooden box with rubber legs that minimize the influence of further external mechanical vibrations. The temperature fluctuations lead to randomly occurring drift at the sensor signal. However, since these fluctuations are

statistically distributed across one experiment, the measurements are repeated several times within the experiment, especially in pulse measurements where the temperature response is small and the relative contribution of the drift is large. Therefore, the heat determined from temperature response fluctuates more strongly at small overpotentials. To assess the error within an experiment and between two experiments, the reproducibility of the molar heat within different measurements from the same experiment is observed, and the mean value of the measurements from several experiments and the respective standard deviation of the mean value is calculated. Besides the measurements, the determination of the calibration factor is prone to very small error originating from the different measured values for the Peltier heat of the redox reaction , $K_3[Fe(CN)_6$ / $K_4[Fe(CN)_6]$, ranging from –45.1 to –41.5 kJ mol^{-1} [26]. Therefore, a value of $\pm$ 2 kJ mol^{-1} can be taken as the error of the experimentally obtained molar heat. The additional errors connected to specific experiments are discussed within the respective chapters.

Chapter 4 Adsorption processes of organic molecules at an electrode surface

In this chapter the adsorption processes of organic molecules on the electrode surface are described to provide a basic understanding for two systems of interest in this work: pyridine and thymine adsorption on Au(111).

For a better understanding of the entropic contributions the process of adsorption of organic molecules on the electrode surface from aqueous solution is considered. For that, several aspects should be considered:

1. The polarity of the water molecules and their ability to form hydrogen bonds leads to relatively strong local ordering in the electrochemical interface.
2. When a foreign particle, in this case the organic molecule, is solvated, two processes are involved:

   2 a) Organic molecules interact with the water molecules, implying that the water molecules arrange themselves around the molecule due to their polarity. Both pyridine and thymine are polar molecules, and the formation of a hydration shell leads to a loss of entropy of the involved water molecules.

   2 b) On the other hand, for the formation of the hydration shell, the participating water molecules must be at least partially removed from their hydrogen bonding network before interacting with the organic molecule. Since this disrupts the ordered structure of water, this process is associated with an increased entropy.

   It cannot be assumed *a* priori which of the two opposing entropy processes will dominate the overall entropy because the concept of “structure–making” and “structure–breaking,” as introduced by Frank and Evans, needs to be considered: if the molecule is “structure–breaking", it increases the overall entropy when solvated. If the molecule is “structure–making” a decrease in the overall entropy will occur when solvated [30, 31].
3. When the solvated organic molecule starts to adsorb on the metal surface, in this case, the Au(111), several processes are involved when assessing the entropic contributions:

   3 a) The hydration shell around the organic molecule is partially or fully liberated. The entropy here is increasing or decreasing for structure-breaking or structure–making molecules, respectively.

3 b) At the interface, the adsorption of the organic molecule leads to a decrease of the local entropy as the organic molecules becomes attached to the surface.

Chapters 5 and 6 are dedicated to disentangling the entropy changes during pyridine and thymine adsorption on Au(111) from aqueous solutions.

Chapter 5 Pyridine Adsorption on Au(111) from Aqueous Solutions

Historically, most of the knowledge on molecular adsorption at metal electrodes was gained using mercury electrodes [32] because mercury is liquid at room temperature and has high surface tension. $KClO_4$ was mainly used as a supporting electrolyte because it does not adsorb specifically like other ions, such as Cl^- [33, 34].

Pyridine adsorbs in two different orientations on mercury, which strongly depend on the electrode's charge. From the Gibbs excess data of this system, reported by Lipkowski et al. [35], it is extracted that the pyridine molecule adopts a perpendicular or a flat orientation at the negatively or positively charged Hg surface, respectively, where the transition from the flat to the perpendicular orientation is gradual [35].

Most knowledge about the effect of the crystallographic orientation of gold electrodes on pyridine adsorption can be gained from the papers reported by Irish, Lipkowski, and Stolberg. They published data for pyridine adsorption on polycrystalline gold electrode surface [36], Au(100) [37], Au(110) [38], and Au(111) [27], where they used chronocoulometry to characterize the pyridine adsorption in $KClO_4$ on the respective electrode surfaces. The adsorption parameters, the relative Gibbs surface excesses, the Gibbs energies of adsorption, and electrosorption valencies were determined as a function of the electrode potential and surface charge density. They found out that pyridine adsorbs on polycrystalline, Au(111) and Au(100) surfaces in two different orientations, depending on the potential: for a negatively charged surface, pyridine adsorbs in a flat orientation, whereas for a positively charged surface, pyridine reorientates and is faced vertically, with the N-atom towards the gold surface. This observation confirms the earlier conclusions by Hamelin and Valette for the Au(111) surface [39]. Hamelin and Valette are the pioneers of a qualitative investigation of pyridine adsorption on an Au(111) single-crystal electrode by employing cyclic voltammetry [40] and differential capacity. By analyzing the surface-potential curves, Lipkowski et al. [27] found that the phase transition from flat to perpendicular pyridine on Au(111) is abrupt, contrary to the Hg electrode.

In Figure 5.1 a typical cyclic voltammogram of Au(111) in 1 mM pyridine / 0.1 M $NaClO_4$ is displayed with a scan rate of 50 mV/s, which was recorded as part of this work. The CV, obtained during the first cycle between –0.9 V and 0.3 V (vs SCE), is almost identical to that reported by Lipkowski [27], and it is shown here for completeness.

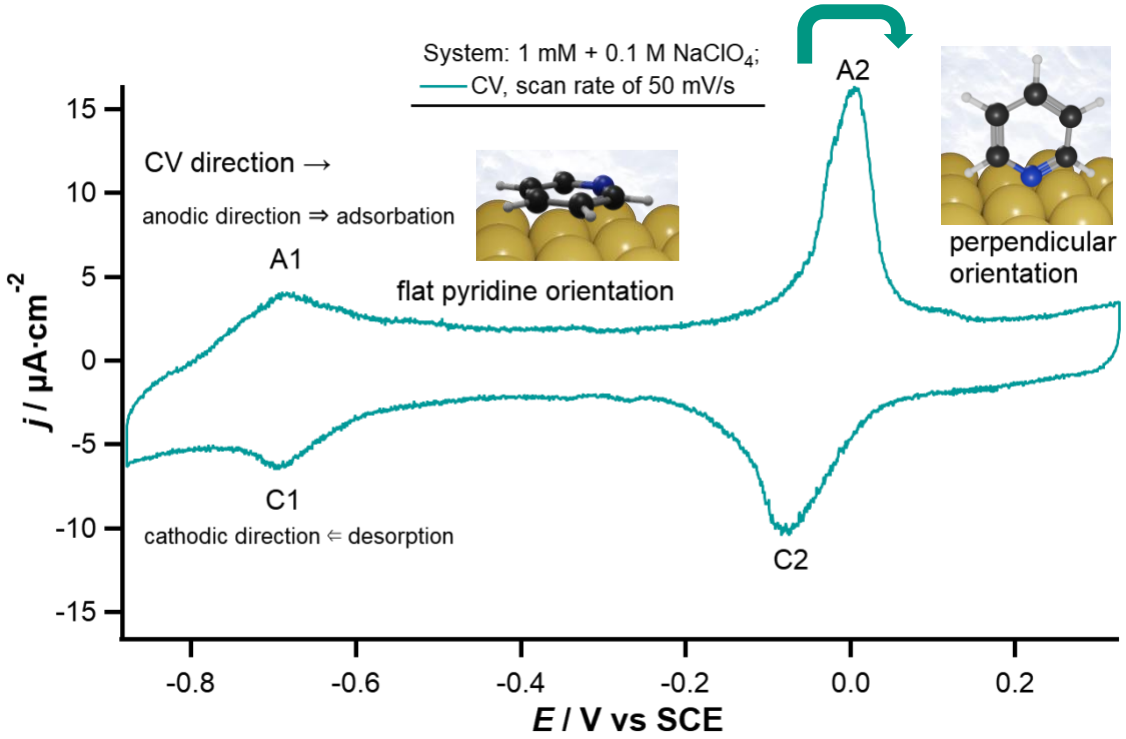

Figure 5-1 Cyclic voltammogram of (111)-textured Au electrode in 1 mM pyridine in 0.1 M $NaClO_4$ as supporting electrolyte, scanned with a rate of 50 mV/s. A1 and A2 correspond to the pyridine adsorption peaks in flat (A1) and perpendicular (A2) orientation; C2 and C1 are the counter peaks for the desorption.

The electrode potential is presented against the saturated calomel electrode, SCE; therefore, for potentials more negative than –0.9 V, the hydrogen evolution reaction on Au(111) begins, and for potentials more positive than 0.4 V, the gold surface oxidation takes place. For better representation, the CV is divided into two regions:

i) Region 1: The adsorption of pyridine starts in the anodic direction at approximately –0.7 V (vs SCE), giving rise to a small, broad peak, A1. Its counter peak, C1, in the cathodic direction, represents the desorption. As introduced at the beginning of Chapter 5, pyridine molecules adsorb on the Au surface in a flat orientation [27]. About 2.5 10^{-10} mol cm^{-2} pyridine molecules are adsorbed per cm^2 on the Au surface for the studied concentration [27]. The pyridine molecules stay adsorbed in a flat orientation on the Au surface at the electrode potential from –0.6 to –0.2 V [41].

ii) Region 2: The phase transition of pyridine molecules from flat to perpendicular orientation occurs at 0 V vs SCE, giving rise to a sharp peak, A2. A2 is assigned to additional adsorption of about 4.5 10^{-10} mol cm^{-2} pyridine molecules [27].

The adsorption of further pyridine molecules is only made possible by transitioning from the flat orientation to a perpendicular mode in which the nitrogen atom of the aromatic ring of the pyridine molecule interacts with the Au surface [35]. The driving force for adsorption on Au(111) involves mixing the nonbonding orbital with the electronic states of the metal. The perpendicularly adsorbed pyridine molecule is bounded by the N-atom and oriented with the negative pole of the permanent dipole towards the surface and the positive pole of the solution. The dipole field interaction stabilizes this type of coordination at the positively charged surface [35]. By increasing the anodic electrode potential, the perpendicularly standing pyridine molecules form a full monolayer. The first scanning tunneling microscopy, STM, image for pyridine adsorption of Au(111) from neutral solutions that confirms the different potential-driven orientations on the surface was reported by Osawa et al. [41]. In their report [41] they did an IR and STM study for 10^{-6} to 10^{-3} M pyridine in 0.1 M $NaClO_4$ on a highly ordered Au(111) surface. For IR, they used surface-enhanced IR adsorption spectroscopy (SEIRAS), which allowed them to obtain high-quality IR spectra. They concluded that pyridine is adsorbed flat on the surface at negative potentials.

The nonspecific coadsorption of the perchlorate anions happens positive to 0.2 V, as Schönig indicated in [42]. Pettinger [43] studied the reconstruction of the Au(111) surface in perchlorate solutions containing pyridine using second harmonic generation (SHG) measurements, and indicated that pyridine adsorption has only a minor influence on the degree of reconstruction of the Au(111) surface. In the section 5.5 is presented the CV for the supporting electrolyte, $NaClO_4$, which confirms the indication from Schönig et al. [42, 44]. Note: the CV shown in Figure 5.1, is limited to the positive range up to ~0.3 V in order to prevent oxidation of the Au substrates, which would lead to desorption of the adsorbed pyridine molecules and disrupt the signals in the cathodic direction. When sweeping in the cathodic direction, two peaks, C2 and C1, are observed, which are assigned to the reorientation and the desorption of the pyridine molecules, respectively.

The CV peaks are slightly broader than those reported by Iqbal et al. [4], likely due to the use of a (111)-textured Au film as a working electrode. However, they are in agreement with the literature CV of a single-crystalline Au(111) electrode [4]. The peaks A1, A2, C1 and C2 of both directions arise at similar electrode potentials,

indicating the reversibility of the process. Another confirmation for this finding is obtained by varying the scan rate. The CVs recorded for different scan rates are shown in Figure 5.2, with clear evidence that the peak current rises with increasing the scan rate.

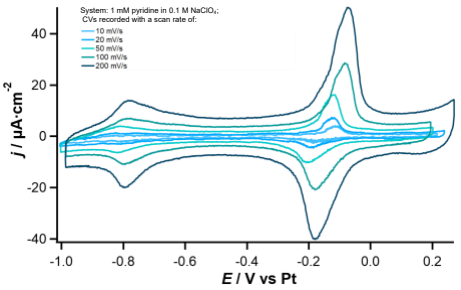

Figure 5-2 Cyclic voltammograms of pyridine in 0.1 M $NaClO_4$ on Au(111) recorded with various scan rates, ranging from 10, 20, 50, 100 and 200 mV/s.

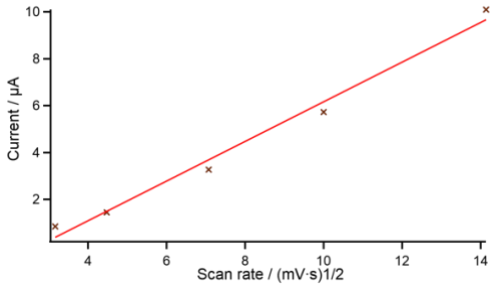

Figure 5-3 Effect of the scan rate of the peak, A2, current, ip, for the CV experiment →Randles-Shevchik equation. The linear dependency indicates that the process is reversible.

Applying the Randles—Ševčík equations (19) and (20) for A2, at –0.1 V, and looking at the plot of the A2 peak current versus the square root of the scan rate, a linear trend is observed, confirming the system's reversibility (Figure 5.3).

$$i_i = 0.4463\, A\, c \left(\frac{n^3 F^3 v D_0}{R T}\right)^{1/2} \qquad (19)$$

$$i_p = 2.69\, 10^5\, n^{3/2}\, A\, c \sqrt{D v} \left(\frac{n^3 F^3 v D_0}{R T}\right)^{1/2} \qquad (20)$$

The maximum current in amps is represented with i_i (or i_p current at the peak); A is the electrode surface area, in this case 0.2 cm^2; c is the bulk concentration of the pyridine molecules; n is the number of electrons transferred in the redox processes; F is the Faraday's constant; v is the scan rate; D_0 is diffusion coefficient of the oxidized analyte ($cm^2\ s^{-1}$); R the ideal gas constant and T is the absolute temperature in K.

Pyridine adsorption was also thoroughly studied by cyclic voltammetry, differential capacity, and chronocoulometry on other metal surfaces, such as different faces of Ag, including Ag(210) [45], Ag(110) [46], Ag(311) [47] and by spectroscopic techniques [48]. From those studies, the character of pyridine coordination is the same as that of gold. Pyridine adsorption has also been examined on various Cu electrodes, such as Cu (110) [49] and Cu(110) [50], where pyridine is tilted towards the surface.

From the electrochemical and spectroscopic studies of pyridine adsorption on Pt(111) [35, 51], it is extracted that in that system, the molecule is only oriented in one configuration, as N-bonded. These studies contributed to understanding pyridine adsorption on metal surfaces over the years.

Conway and Gordon were the first to calculate the entropic effects during adsorption processes on mercury [52]. They studied the thermodynamic properties of pyridine adsorption on mercury, using $KClO_4$ as a supporting electrolyte. They applied electrocapillary measurements at different temperatures to gain information about the enthalpic and entropic contributions. From their research, two key points are extracted:

1. Enthalpic contributions – the heat of adsorption of pyridine, independent of the charge state and the coverage, is always negative;
2. Entropic contributions – From their work [52], the second conclusion can be extracted by tracking the isosteric standard entropies of pyridine adsorption as a function of the charge for various coverages. It becomes evident that in almost all cases, the entropy of pyridine adsorption is negative, indicating that it is not favored entropically. It can be estimated that the average standard entropy of pyridine adsorption is on the order of –6 cal $mol^{-1}K^{-1}$, giving rise to about –25 J $mol^{-1}K^{-1}$, at a charge of 8 µC cm^{-2}. Deviations from a negative entropy of adsorption are observed in the case of low coverages. For coverages less than 0.2 ML and a charge state smaller than 1 µC cm^{-2}, the entropy of adsorption of pyridine becomes positive with a maximum of about 10 cal/mol K, corresponding to about 42 J $mol^{-1}K^{-1}$ for a coverage smaller than 0.1 ML and a charge state of about –5 µC cm^{-2}.

Motivated by the thorough research on pyridine adsorption on Au(111), its vast application for fundamental studies, and its technological relevance as a potent cocatalyst for CO_2 reduction, this system is further examined by the electrochemical microcalorimetry. This work provides data on the entropic contributions during pyridine adsorption on Au(111) from aqueous solutions.

5.1 Results from the Microcalorimetric Measurements

In this Chapter, the data from the microcalorimetric measurements on 1 mM pyridine adsorption on a (111)-textured Au electrode from an aqueous 0.1 M $NaClO_4$ solution at 298.15 K is presented. A pyridine concentration of 1 mM is chosen due to the following two reasons: a) for pyridine concentrations higher than 5 mM, pyridine desorption overlaps the cathodic hydrogen evolution reaction; b) for concentrations smaller than 0.1 mM, the additional adsorption and phase-transition peak occurs at almost the same potential as the peak for anion adsorption. Another reason is that in $NaClO_4$, the pyridine molecule is not charged, implying that the amount of pyridinium, the conjugated acid of pyridine, is less than 5%. The influence of the different concentrations is discussed in the subchapter 5.5.

5.1.1 Microcalorimetric pulse experiments

The microcalorimetric pulse experiments were performed for the potential range between –0.7 V and 0.2 V (cf. Figure *5-1*). Two types of microcalorimetric experiments were carried out: continuous current and potential pulse experiments.

5.1.1 a Continuous current pulse experiments

A series of continuous current pulses was applied by scanning the whole adsorption region, starting from –0.7 V and ending at ~0.2 V. In Table *5-1*, exemplary pulse transients with a current pulse duration of 10 ms and constant pulse amplitude are presented. For different sets of pulses, the continuous amplitude varied from 30 µA to 60 µA, with increments of 5 µA. Afterwards, the desorption region, starting from ~0.2 V and ending at –0.7 V was scanned by applying 10 ms long continuous current pulses with negative amplitudes (–30 to – 60 µA with an increment of 5 µA).

Table 5-1 Potential, current and temperature transients of four 10 ms long continuous current pulses of 1 mM pyridine adsorption (a; +40 μA) and desorption (b; –40 μA) on (111)-textured Au in 0.1 M $NaClO_4$. The pair of anodic and cathodic pulses correspond to the pair peaks A1/C1 and A2/C2.

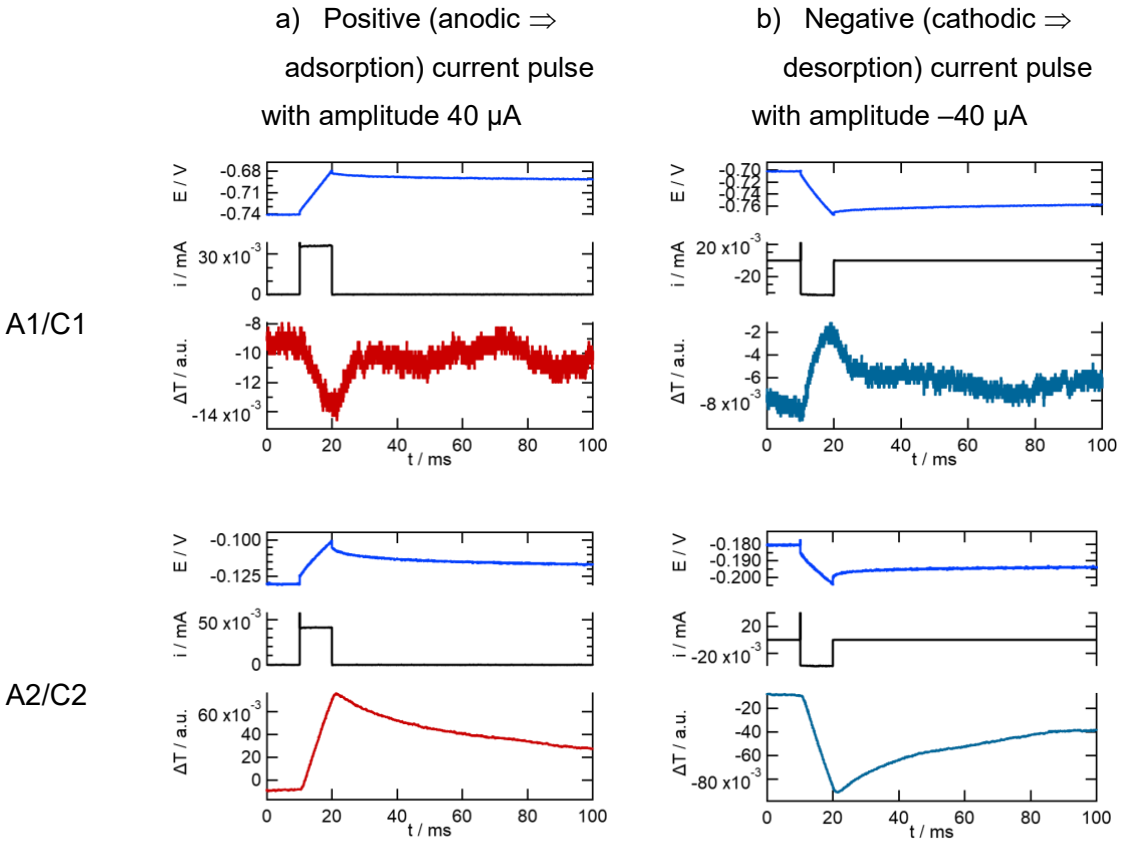

Based on Table *5-1*, the potential transients (the ink-blue line in the upmost panel) are linearly increasing (positive pulse) or decreasing (negative one) from the beginning of the pulse at t = 10 ms until the end of the pulse at t = 20 ms. After that, the cell is switched back to open circuit conditions, and the potential transient slowly relaxes.

Regarding the current transients (the black line in the second row from each panel in Table *5-1*), an immediate increase (or decrease) is observed at the pulses start at t= 10 ms, where the current value reaches a maximum (or minimum), rated to the applied amplitude. The features at the beginning of the pulse are caused by electronic artefact. The current amplitude stays at the same height until the end of the pulse at t = 20 ms, and when the cell is switched back to open circuit conditions, the current drops immediately to zero.

The temperature of the electrode, indicated by red and blue colours for positive and negative pulses, respectively (shown in the third row of each panel in Table *5-1*), decreases for the positive and increases for the negative pulse at potentials around A1/C1 peak pair. At the potentials around A2/C2, the opposite is encountered. Generally, the electrode temperature reaches its maximum, or minimum, at t = 22 ms and afterwards relaxes to the value before the pulse due to thermal equilibration with the surrounding cell and the electrolyte.

Figure *5-4* below shows the change of the electrode temperature transients from a set of positive continuous current pulses (during the pyridine adsorption).

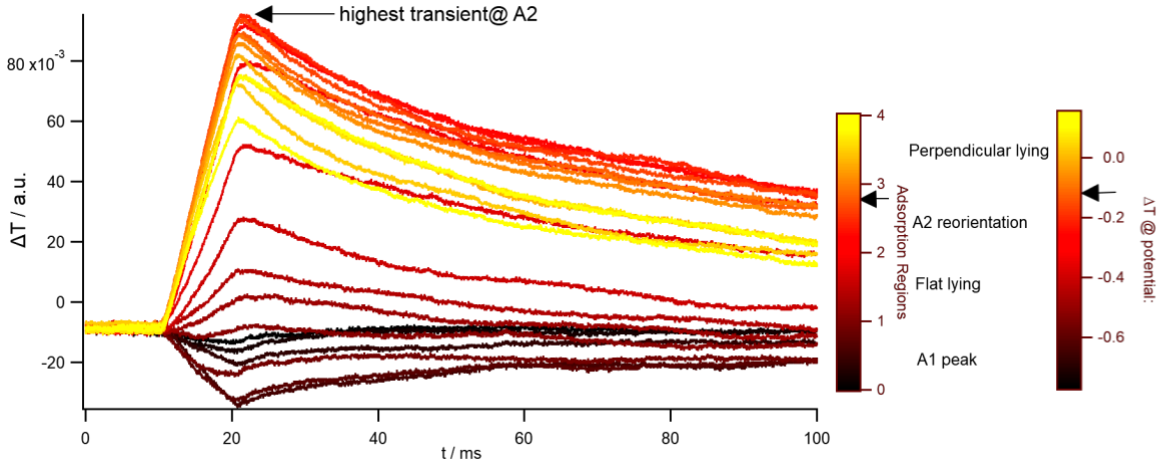

Figure 5-4 Temperature transients from anodic (positive) current pulses over the adsorption region. The scales on the right-hand side indicate for which region (the first one) and potential (the second one) the respective temperature transient belongs to. The numbers (0– 4) on the adsorption region scale have no intrinsic meaning; they simply serve as markers to separate the different adsorption regions.

Figure *5-4* shows that at the adsorption peak A1 (transients coloured with dark brown, as indicated on the colour panel on the right-hand side), at a potential of around –0.7 V, the temperature transient decreases and reaches a minimum at the double-layer area, where the pyridine molecules are adsorbed in the flat position. With pulsing more towards positive potentials, the temperature transients increase and reach a maximum at about the peak, A2. Afterwards, the transient height decreases; again, a slight increase is noted at –0.05 V.

This trend indicates that a change in the sign of the heat should be expected. As described in Chapter 3, the data needs to be calibrated to disentangle the heat behaviour from these current pulses.

Table *5-2* shows exemplary pulses of the fitted temperature transients of the pulses from Table *5-1*.

Table 5-2 Potential, current, temperature transients, as well as the laser adjustment (black line in the third panel), the absolute heat (ink-blue line in the third panel) and the heat flow (red dots in the second panel) of two 10 ms long continuous current pulses from 1 mM pyridine adsorption (+40 µA) on Au(111) in 0.1 M $NaClO_4$ as supporting electrolyte, at potentials at A1/C1 and A2/C2 peak pairs.

Region	Positive (anodic ⇒ adsorption) current pulse with amplitude 40 µA, fitted with 40 mp	Region	Positive (anodic ⇒ adsorption) current pulse with amplitude 40 µA, fitted with 40 mp
A1/C1	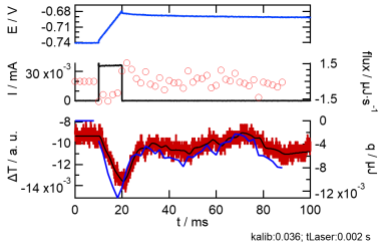	A2/C2	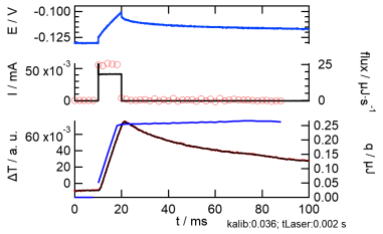

The text below discusses the observations made in the anodic direction because a positive pulse series drives the pyridine adsorption.

At the potentials at the A1/C1 peak pair, the heat flux (red dots in the second row in the panel) and the heat transient (the ink-blue line at the third row from each panel) for the pulse from the region of the peak A1, are wobbly. That is because there is very little heat involved in this region.

At the potentials at the A2/C2 peak pair, the heat flux is correlated with the current flow during the pulse and goes back to zero after the pulse. The heat transient increases and stays at the same height, implying that all the heat was transferred during the pulse.

For the positive current pulse, the temperature at the electrode starts to rise, signaling the evolution of heat around A2/C2 peak where the phase transition and the additional adsorption of pyridine molecules occurs.

5.1.1 b Potential pulse experiments

For the potential range between –0.7 V and 0.2 V, a series of 10 ms long positive and negative potential pulses is applied, varying the potential amplitude starting from the same base potential. In Table *5-3*, example transients from a positive and a negative potential pulse at an initial potential of –0.15 V are shown.

Table 5-3 Potential, current, temperature transients, as well as the laser adjustment (black line in the third panel), the absolute heat (ink-blue line in the third panel) and the heat flow (red dots in the second panel) of two 10 ms long potential pulses (with pulse amplitude of (a) +0.05 V and (b) –0.05 V) from 1 mM pyridine on Au(111) in 0.1 M $NaClO_4$ as supporting electrolyte. The pulses are at the region where maximum molar heat was observed, for the anodic direction, that is around the region where additional pyridine molecules adsorb and the phase transition from flat to perpendicular occurs.

	a) Positive potential pulse with amplitude 0.05 V, fitted with 40 mp	b) Negative potential pulse with amplitude –0.05, fitted with 40 mp
A2 at –0.15 V	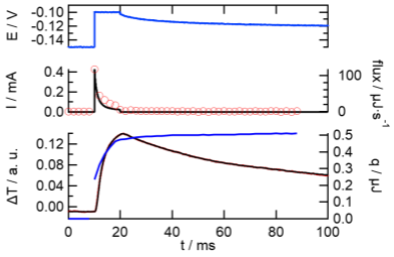	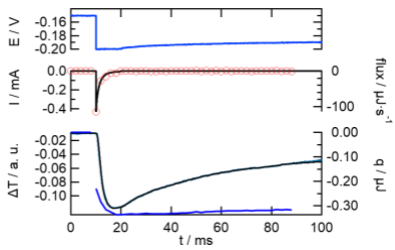

Table *5-3* reveals that the applied potential amplitude (ink-blue transient in the first row, with a potential amplitude of ±0.05 V) is increasing or decreasing, depending on the pulse direction, and it reaches its maximum or minimum height at the start of the pulse at t = 10 ms. The potential is kept constant during the pulse, while after the pulse at t = 20 s, the potential slowly relaxes. The current (black transient in the second row in the panel) reaches its maximum or minimum height when the pulse is applied at t = 10 ms and exponentially decreases or increases to zero current at the end of the pulse (t = 20 ms). The heat flux (red dots in the panel's second row) strongly correlates with the current flow. Lastly, the electrode temperature (red or blue transient in the third row in the panel) increases (a) or decreases (b) during the positive or negative potential pulse. This finding implies that the system becomes warmer or colder in the anodic or cathodic direction, respectively. The heat transient (ink blue transient at the third row in the panel) increases (a) or decreases (b) and stays constant until t = 90 ms.

The molar heat from the potential pulses is determined from the temperature transients following the same procedure described in Chapter 3. It does not contain contributions from the Joules heat because the Joules heat is explicitly excluded by the methodology applied. Figure *5-5* shows an example of the molar heat determined

at a base potential of –0.15 V versus the applied potential pulse amplitudes, at t = 40 ms. At higher pulse amplitude, the overpotential is larger; thus, the contribution of the heat from irreversible processes becomes larger. For smaller overpotentials, the errors of the molar heat values become larger due to lower electrochemical conversion during the potential pulse [42].

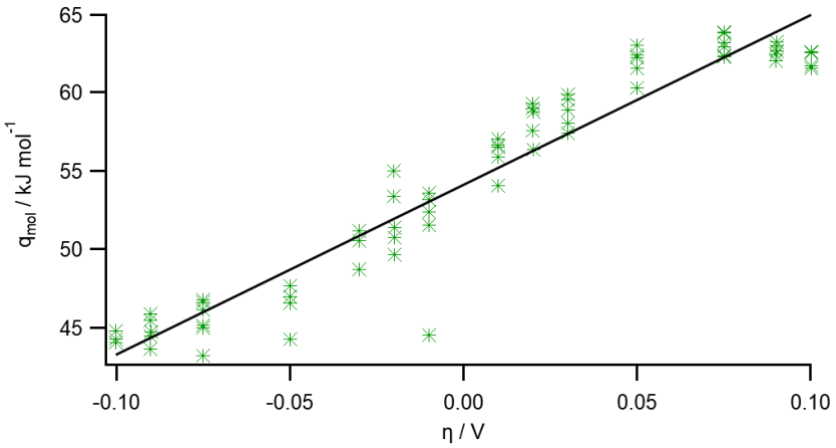

Figure 5-5 Linear adjustment of the molar heat of potential pulses measurement (@ t = 40 ms) in 1 mM pyridine in 0.1 M $NaClO_4$ on Au(111). Starting from an initial potential of –0.15 V (vs Pt) potential pulses are applied with amplitudes: ± 0.01, 0.02, 0.025, 0.05, 0.075, 0.09 and 0.1. The Peltier heat is determined by interpolating the molar heat to 0 V (to an equilibrium) and in this example is 54 ± 2 kJ mol^{-1}.

The Peltier heat (the reversible molar heat) is determined by interpolating the molar heat values to zero overpotential.

5.2 Molar Peltier Heats of Pyridine Adsorption on (111)-textured Au film from $NaClO_4$

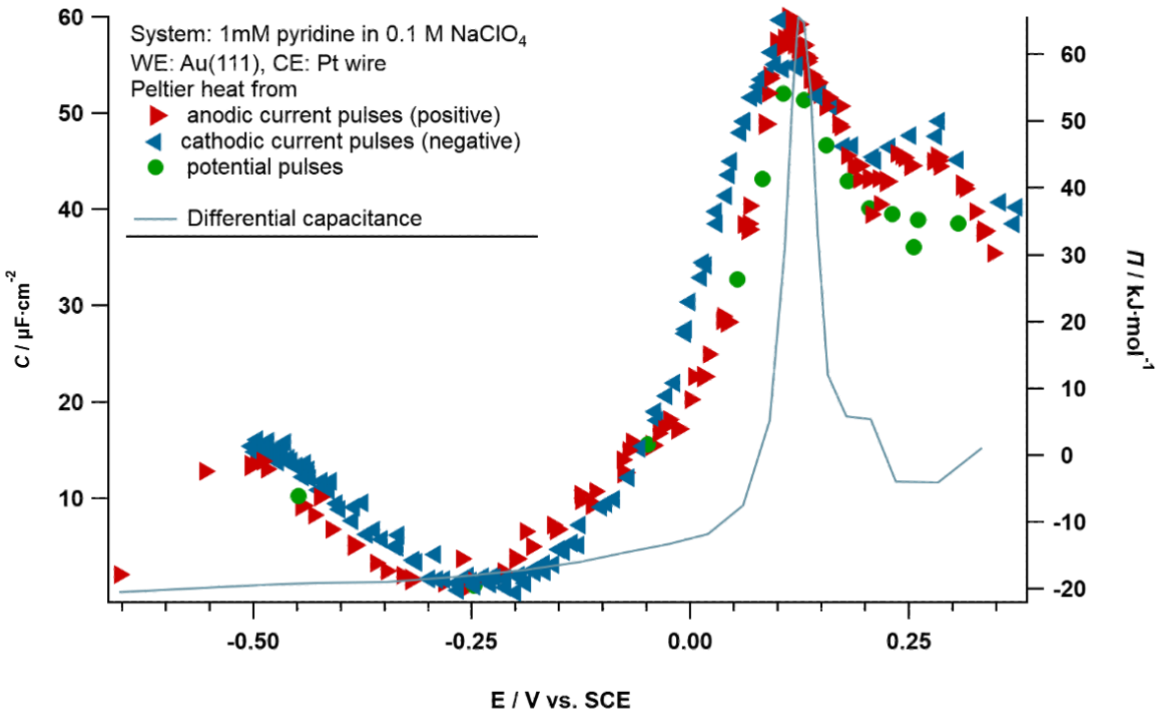

Figure 5-6 Plot of the capacitance data and the Peltier heat from all different experimental procedures versus the electrode potential. The red triangles represent the heat from the anodic current pulses with amplitude of 40 µA, the blue triangles are representing the heat from the cathodic current pulses with amplitude –40 µA, and the green dots are from the Peltier heat from the potential pulse measurements. The blue line is the differential capacitance (determined from the current pulse measurements of the anodic direction).

Figure *5-6* displays the Peltier heat from the different experimental procedures, plotted with the differential capacitance. The differential capacitance exhibits one sharp peak at 0.125 V vs SCE with a shoulder-like peak at positive potential. According to Lipkowski [27], the main peak corresponds to the additional adsorption of pyridine molecules and the reorientation of pyridine, namely peak A2 from the CV. The smaller shoulder-like peak in the capacitance data appears for pyridine concentrations of at least 1 mM in highly ordered Au(111) single-crystal electrodes [4]. That confirms that the surface was highly ordered even for this thesis, where (111)-textured Au electrodes were used. In the capacitance data in Figure *5-6*, a peak from the pyridine

adsorption, A1, is not observed, probably because a small charge is involved with the pulses at that region.

In Figure *5-6*, the experimental data of the Peltier heat from the current pulses is indicated with red for the positive and blue for the negative pulses. The deviation of the molar heat values for both pulse directions is small, ca. 2 kJ mol^{-1}, signaling high reversibility of the processes involved. The molar Peltier heat slightly decreases and reaches its minimum at about –0.22 V. Afterwards, the molar heat increases and reaches a maximum of about 65 kJ mol^{-1}, at ca. 0.1 V. Going towards more positive electrode potential, the molar heat decreases slightly before a shoulder-shaped pattern emerges.

The Peltier heat from the potential pulses, green circles in Figure *5-6*, follow the same trend as the Peltier heat from the current pulses, reaching a maximum heat of 55 ± 2 kJ mol^{-1} at about 0.1 V.

Figure *5-6* shows that the maximum Peltier heat of 60 ± 5 kJ $mol_{e^-}^{-1}$ is about at the same potential as the peak A2 (0.11 V vs SCE). It can be concluded that heat is evolving and transferred towards the surroundings for additional adsorption of pyridine molecules and reorientation.

In order to explain the Peltier heat per molecule of pyridine and to be able to explain the reaction entropy of pyridine adsorption, it is necessary to determine the number of adsorbed molecules per mole of electrons that flowed in the outer cell circuit. This can be achieved by considering the work of Lipkowski. Lipkowski [27] obtained the surface concentration-charge density curves for several pyridine concentrations in 0.1 M $KClO_4$ on Au(111). The slope of the respective curve corresponds to the increase of the amount of pyridine molecules per charge increment. By multiplying it with the Faraday constant, 9648 C per $mole_{e^-}$, the number of pyridine molecules per mole of electrons can be determined. Figure *5-7* presents the digitized

surface concentration-charge density curve data for 1 mM pyridine from reference [27]. The data points are digitized using the *Engauge Digitizer* program.

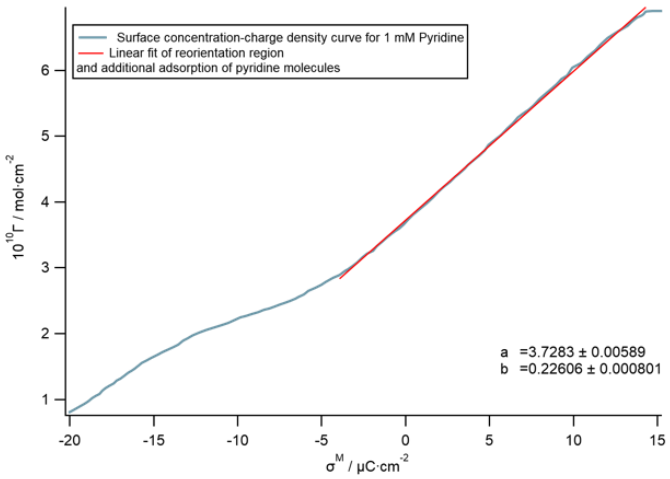

Figure 5-7 Digitized data of surface concentration-charge density curves for 1 mM pyridine and the slope taken for calculating the amount of adsorbed pyridine molecules per electron adapted from [27].

The most significant change in the Peltier heat is in the region of additional adsorption of pyridine molecules and reorientation, at a surface charge between –2 to 12 μC cm^{-2}, as seen in Figure *5-7*. Therefore, the slope from that region is taken for the conversion from moles of electron to moles of pyridine. From the conversion, it is calculated that about 1.7 pyridine molecules adsorb to the electrode per electron in the outer circuit.

5.3 Determination of the experimental Reaction Entropy

From the microcalorimetric experiments, a maximum Peltier heat of 60 ± 5 kJ mol_e^{-1} is measured for adsorption of pyridine molecules and reorientation (at T = 298.15 K). According to (5) in Chapter 2:

$$\Pi = T\,(\Delta_R S - \Delta_T S)$$

$$\frac{\Pi}{T} = -\,(\Delta_R S + \Delta_T S)$$

$$-201\ \text{J mol}_e^{-1}\ \text{K}^{-1} = (\Delta_R S + \Delta_T S)$$

The Peltier heat corresponds to the sum of the reaction entropy and the entropy of transfer. The entropy of transfer, $\Delta_T S$, arises from the charge transfer across the boundaries of the half-cell, where $\Delta_T S$ is determined by (9). For the system of 1 mM pyridine with 0.1 M $NaClO_4$. The Eastman entropies of transfer (for the perchlorate, –3.1 J $mol^{-1}K^{-1}$ and the sodium, 7.1 J $mol^{-1}K^{-1}$ [18]), the molar limiting conductivities (for the perchlorate, 67 S $cm^2\,mol^{-1}$ and the sodium 50 S $cm^2\,mol^{-1}$ [53]) and the Hittorf transfer number of the predominant ions were taken for the calculation. The contribution of the pyridine is neglected because it is very small. Accordingly, the determined value for the entropy of transfer is –4.5 J $mol^{-1}K^{-1}$.

Consequently, the reaction entropy amounts to $\Delta_R S \approx -196$ J $mol_e^{-1}\ K^{-1}$. To interpret the reaction entropy change, it is necessary to convert it to the amount of pyridine molecules adsorbed per transferred electron as measured in the outer circuit. That is done by dividing the reaction entropy value (deduced from the microcalorimetric experiments) with ca. 2 pyridine molecules that are adsorbed to the electrode per electron in the outer circuit (c.f. Figure 5-7). This amount to a value of $\Delta_R S \approx -98 \pm 20$ J $mol_{py}^{-1}\ K^{-1}$, referred to the amount of pyridine molecules additionally adsorbing in the scope of the second adsorption step (peak A2 in the CV). The previously deduced value should be quantitatively compared with the literature data to disentangle the entropic contributions to the overall reaction entropy.

5.4 Quantitative comparison of the experimental reaction entropy with the literature

Two models of the pyridine adsorption process were built for a quantitative comparison of experimental measured reaction entropy.

5.4.1 Thermodynamic Cycle

Scheme 5-1 represents the thermodynamic cycle of pyridine adsorption. The cycle is used as a first model to estimate the reaction entropy quantitatively.

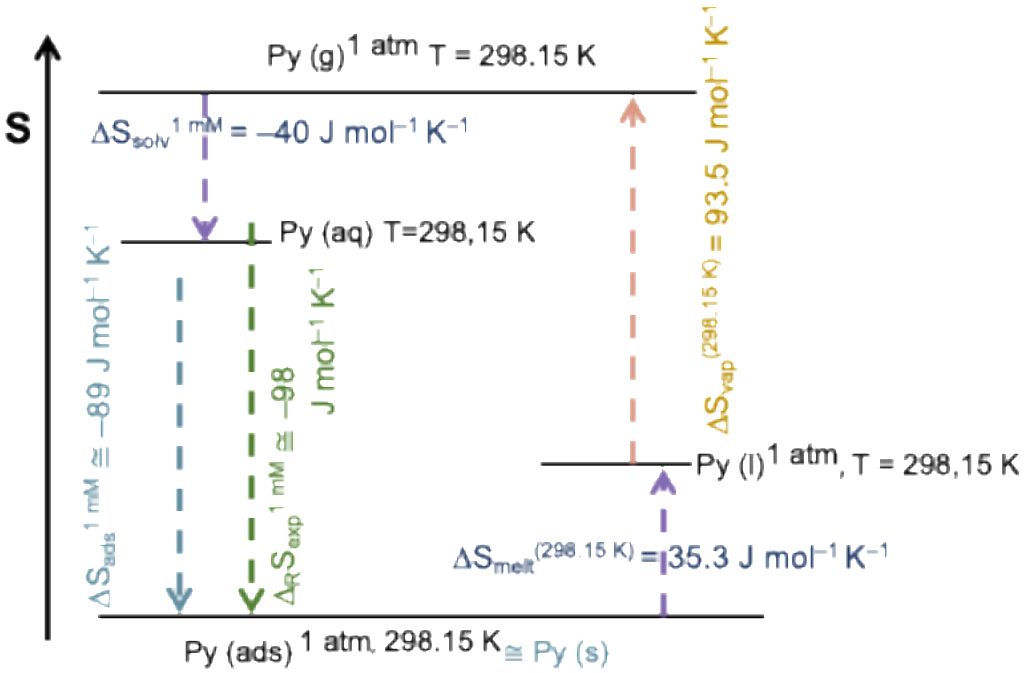

Scheme 5-1 Thermodynamic cycle of pyridine adsorption and desorption. The upper most horizontal line represents pyridine in gaseous state, the second horizontal line (on the left-hand side) represents the pyridine in aqueous state. The lowest horizontal line represents the pyridine adsorbed on the Au(111) surface, and it is assumed that that is equal to pyridine in solid state. The second line (from the right-hand side) represents the pyridine in liquid state. The arrows in between are the transition processes.

1. The thermodynamic cycle (right-hand side of Scheme *5-1*), involves the entropy of melting of the pyridine from a solid to a liquid state. The entropy of melting, $\Delta S_{py,melt}$ for pure pyridine solution is 35.7 J mol_{py}^{-1} K^{-1} [54] at 231.5 K, and needs to be

adjusted for room temperature, 298.15 K. The conversion can be done by using Kirchhoff's law:

$$\Delta S_{py,melting}(298.15\ K) = \int_{298\ K}^{T_m} \frac{(c_{p,l} - c_{p,s})}{T} dT + \Delta S_{py,melting,\ Tm}$$

where $c_{p,l}$ and $c_{p,s}$ are heat capacities of the liquid and solid state, respectively. Their variation with the temperature according to the experimental values for pyridine from [54] is linearly approximated, which could lead to an error. The values are summarized in the Table below:

	Pyridine
T_m / K	231.5
$\Delta S_{py,melting,Tm}$ (J $mol^{-1}K^{-1}$)	35.74
$c_{p,l}$ (T_m) (J $mol^{-1}K^{-1}$)	133.3
$c_{p,s}$ (T_m) (J $mol^{-1}K^{-1}$)	101.2
$c_{p,s}$ $(298.15)^{1atm}$ (J $mol^{-1}K^{-1}$)	133.3
$\Delta S_{py,melting,298.15\ K}$ (J $mol^{-1}K^{-1}$)	35.32

The calculated entropy of melting pure pyridine at 298.15 K is 35.32 J mol_{py}^{-1} K^{-1}.

2. The next step is vaporizing the liquid pure pyridine solution (right-hand side of Scheme *5-1*). The entropy of this transition can be estimated from the entropy of vaporization of pyridine known from the literature (–90.32 J $mol^{-1}K^{-1}$ at T = 388.2 K [55]). This value has to be translated to the room temperature, too. The conversion can be done, as in the above, by using Kirchhoff's law:

$$\Delta S_{py,vap}(298.15\ K) = \int_{T_b}^{298\ K} \frac{(c_{p,g} - c_{p,l})}{T} dT + \Delta S_{py,vap,Tb}$$

where $c_{p,g}$ and $c_{p,l}$ are heat capacities of the gaseous and the liquid state, respectively. Their variation with the temperature according to the experimental values for pyridine from the literature [55] is linearly approximated and the values are summarized in the table below:

	Pyridine
T_b / K	388.2
$\Delta S_{py,melting,Tb}$ / (J $mol^{-1}K^{-1}$)	90.32
$c_{p,g}$ (T_b) / (J $mol^{-1}K^{-1}$)	146.9
$c_{p,l}$ (298.15)^{1atm} / (J $mol^{-1}K^{-1}$)	134.93
$\Delta S_{py,vap,298.15\ K}$ / (J $mol^{-1}K^{-1}$)	93.43

The estimated values for the temperature correction of the entropy of freezing and condensation can have an inevitable error because of the approximations made regarding the heat capacitance value. The calculated entropy of vaporizing pyridine at 298.15 K is 93.5 J mol_{py}^{-1} K^{-1}.

3. The solvation of the pyridine is presented in the left-hand side of the cycle, starting from the gaseous pyridine state (left side of Scheme *5-1*). A calculated literature value for the entropy of transfer of pyridine from the gas phase to aqueous solution exits. Warshel and Florian [56] build a theoretical model to evaluate hydration entropies of neutral and ionic molecules at 298.15 K. The calculated hydration entropies, enthalpies, and free energies were defined as total entropy, enthalpy, and free energy changes associated with the transfer of a solute from a fixed position in the gas to a fixed position in an infinitely diluted aqueous solution. This definition corresponds to the 1 M aqueous solution in standard states. In their work, they calculated $-T\Delta S_{hydration}$= 7.1 kcal mol^{-1} for the hydration entropy of neutral pyridine, which corresponds to ≈ –100 J $mol^{-1}K^{-1}$ at T = 298.15 K. They

compared this value with the experimentally evaluated one, $-T\Delta S_{hydration}^{e}$ = 6.6 kcal mol^{-1}, or $\Delta S_{hydration} \approx -94$ J mol^{-1}K^{-1}, from the hydration-free energies and enthalpies reported by Cabani et al. [57], with previously transforming the hydration enthalpies to 1 M gas standard state. An averaged value from these theoretical and experimental works amounts to –97 J mol^{-1}K^{-1}, and it is taken for further usage. The entropy of solvation of 1 mM pyridine from a gaseous to an aqueous state can be estimated by taking the average of –97 J mol^{-1}K^{-1} that is calculated for 1 M pyridine concentration in standard state and correcting it for the concentration (in this example case for 1 mM pyridine) by using the relation:

$$\Delta S_{sol,1mM\ py} = s^{0}_{py(aq)nWater} - s^{0}_{py(g)} - R\ln c_{py(aq)nWater} + R\ln c_{py(g)} = (-97 + 57.4 + 0)$$
$$\text{J mol}^{-1}\text{K}^{-1} \approx -40 \text{ J mol}^{-1}\text{K}^{-1}$$

Where it is assumed that activities are equal to the concentrations of the products and reactants (1 mM for the product and 1 M for the educt), the value calculated for the solvation entropy, corrected for the concentration effect, is about –40 J mol^{-1}K^{-1}. The assumption of the ideal dilution of pyridine from 1 M to 1 mM could lead to error.

4. The last transition for completing the thermodynamic cycle presented in Scheme *5-1* is the adsorption of the solvated pyridine on the Au(111) surface. Since the entropy changes of all other steps of the TD cycle are known, the adsorption entropy can be readily calculated:

$$\Delta_R S_{py,ads,calc} = -(\Delta S_{py,melting,298\ K} + \Delta S_{py,vap,298\ K}) + \Delta S_{sol,1mM\ py} =$$
$$= (35.3 + 93.5 - 40) \text{ J mol}^{-1}\text{K}^{-1} \approx -89 \text{ J mol}_{py}^{-1}\text{ K}^{-1}$$

The calculated value for the adsorption entropy of –89 J mol$_{py}^{-1}$ K^{-1}aligns with the reaction entropy obtained from the measurements in this work, –98 J mol$_{py}^{-1}$ K^{-1}, leading to a conclusion that the entropy reduction upon the pyridine adsorption is a consequence of pyridine desolvation and its fixation on the Au(111) surface.

The difference in the calculated and measured reaction entropy is within the experimental error. However, several other influences contribute towards the reaction entropy:

i) The effect of the neutral pyridine molecules' adsorption from their solvated state in the solution to their final position on the surface includes structural changes of the water by releasing the solvation shell in the solution and eventual structural

changes of water in the interface. The latter ones would be probably small if the surface is only pyridine-covered; suggesting that pyridine retains its solvation shell upon the adsorption. In addition, the "configurational" entropy contribution from lifting the flat-lying molecules is considered negligible.

ii) The charging of the double layer, DL, by solvated ClO_4^-. Since the perchlorate anion is non-specifically adsorbed, the ClO_4^- adsorption is probably in the outer Helmholtz plane, on top of the pyridine layer. Therefore, this contribution is also expected to be relatively small.

It is hereby assumed that the entropy of the adsorbed pyridine corresponds to that of frozen pyridine, with similarly restricted translational and rotational degrees of freedom.

5.4.2 Alternative simple model

An alternative attempt for quantitative estimation of the reaction entropy is presented in Scheme *5-2*. This simpler model assumes that the pyridine precipitates from an aqueous solution to solid pyridine with restricted translational and rotational degrees of freedom. The right-hand side of Scheme *5-2* represents the transitions of pyridine in aqueous solution to pyridine liquid and later to solid pyridine. These transitions are calculated by diluting pure pyridine solution to 1 mM aqueous solution, with opposite sign, and later freezing the pure pyridine. The entropy change of freezing is the same as melting with the opposite sign, i.e.,

$$\text{Py(1 mM, l)} \rightarrow \text{Py (12.4 M, 198.15 K, l)} \rightarrow \text{Py (s, 298.15 K)}$$

$$\Delta S_{py,melting}(12.4\ \text{M}, 298.15\ \text{K}) = 35.3\ \text{J mol}_{py}^{-1}\ \text{K}^{-1}$$

The amount of the entropy of melting can be corrected for the concentration of 1 mM by considering that the concentrations are equal to the activities, which results in precipitation entropy of $\Delta S_{py,prec}(1\ \text{mM}, 298.15\ \text{K}) = 113\ \text{J mol}_{py}^{-1}\ \text{K}^{-1}$, from which –35.3 J $\text{mol}_{py}^{-1}\ \text{K}^{-1}$ belongs to the freezing, and the rest to concentrating from 1 mM to 12.4 M liquid pyridine.

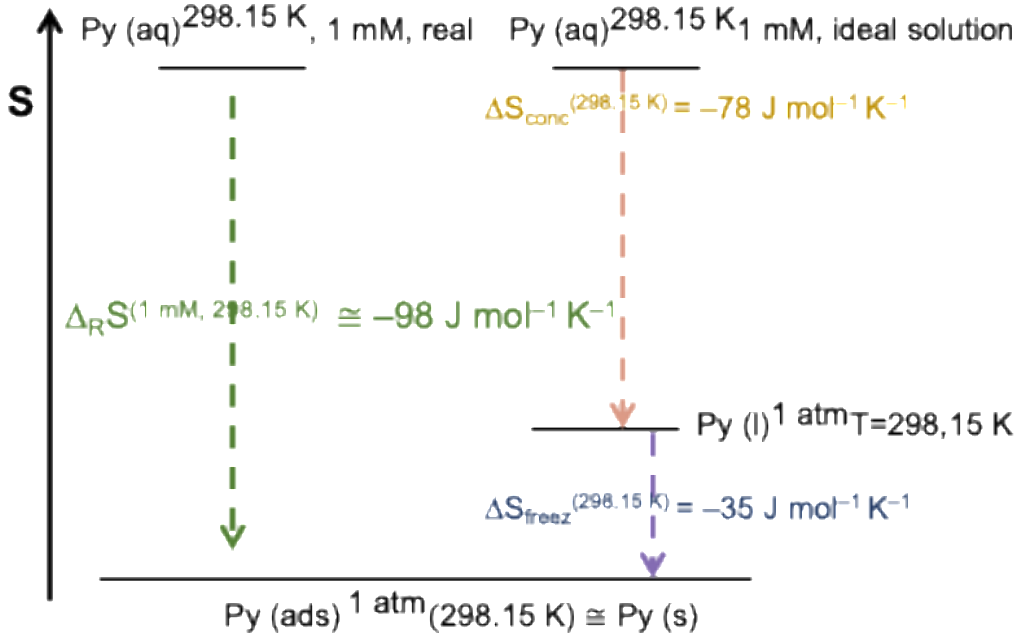

Scheme 5-2 Simplest model for interpretation of the entropy. Left: measured reaction entropy. Right: hypothetical freezing process of pyridine from a 1 mM aqueous solution.

Despite the coarse approximations of the model, the approximated entropy of the hypothetical freezing process of pyridine from a 1 mM aqueous solution is in good agreement with the reaction entropy of the electrochemical pyridine adsorption, –98 J mol_{py}^{-1} K^{-1}.

The dominant contribution towards the adsorption process originates from the fixation of the pyridine. Regarding the solvation, the results suggest that pyridine might remain solvated during the adsorption. The difference of 15 J mol_{py}^{-1} K^{-1} is within the experimental error bar or it could originate from the DL charging. Additionally, the assumptions made for the ideal solutions could deviate since concentrations are used instead of the activities, which are unknown for the components in the thermodynamic cycle.

5.5 Influence of the pyridine concentration on *Γ*

The last part of this chapter discusses the electrochemical microcalorimetric experiments performed with varying pyridine concentrations. Figure *5-8* depicts the typical cyclic voltammograms for Au(111) in 0.1 M $NaClO_4$, with pyridine absent or present in various concentrations (0.1, 1 and 10 mM). They were recorded at a rate of 50 mV/s.

The positive scan obtained only for the electrolyte solution, 0.1 M $NaClO_4$ (the green CV from the Figure *5-8*), displays a broad peak at around 0 V [27]. This peak is assigned to the adsorption of the perchlorate anion and a lifting of the ($p \times \sqrt{3}$) reconstruction [27]. In the cathodic direction, the counter peak for the anion desorption and the (partial) recovery of the surface in terms of the ($p \times \sqrt{3}$) reconstruction is observed at –0.1 V.

Figure *5-8* also includes the cyclic voltammogram for a concentration of 0.1 mM pyridine (the black curve). The anodic peak around –0.2 V is related from pyridine adsorption and its phase transition.

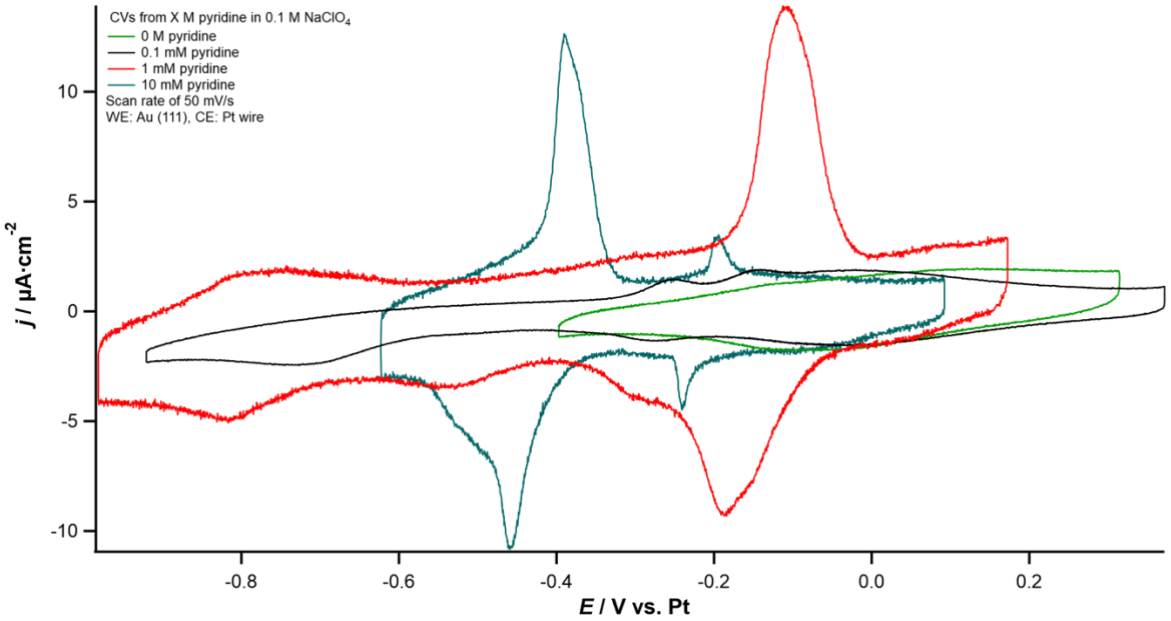

Figure 5-8 CVs from a Au(111) electrode in 0.1 M $NaClO_4$ solution without pyridine (green) and with pyridine at 0.1 mM (black), 1 mM (red) and 10 mM (blue-green). All CVs are recorded with scan rate of 50 mV/s. Note: The CVs presented in the figure are referenced against a Pt pseudo-reference electrode. Consequently, the observed peak potentials do not correspond to the absolute potential scale.

Two pairs of peaks are observed for a concentration of 10 mM (blue curve in Figure *5-8*). Besides the prominent peak pair, A2/C2, at –0.4 V that is assigned to pyridine adsorption and its phase transition, a second pair of peaks appears at 0.2 V, A3/C3. This peak is observed only for the 10 mM pyridine concentration on a highly ordered Au (111) electrode, and it was first reported in 2015 by Wandlowski et al. [58]. In this study, Wandlowski et al. combined electrochemical measurements with shell-isolated nanoparticle-enhanced Raman spectroscopy (EC-SHINERS). They used different pyridine concentrations (0.1, 1, and 10 mM) in a neutral solution, 0.1 M $NaClO_4$ on Au(111), Au(100), and Au(110) surfaces. They found that the $\nu 1$ ring breathing mode frequency and intensity are due to Au surface structure transitions and flat π-bonded to vertical N-bonded pyridine reorientation. In that study, the formation of the 3rd peak in the anodic direction (note: the peak A1 cannot be observed in the CV at this concertation) was observed at more positive potentials for higher pyridine concentration (10 mM pyridine). The group could not describe the origin of the peak, but they suggested that it might be a formation of a second pyridine adlayer. A few months later, while Iqbal et al. [4] were obtaining friction force microscopic, FFM, studies for several pyridine concentrations (1, 2, 5 and 10 mM) in 0.1 M $NaClO_4$ on Au(111) surfaces – confirmed the appearance of the 3rd peak at the adsorption region and concluded that it neither originate from 2nd pyridine adlayer formation nor from further phase transition. In 2018, Jacob et al. [59], while studying the enhanced electrocatalytic oxidation of formic acid on Au(111) in the presence of pyridine, ascribed the 3rd adsorption peak, A3, as coadsorption of perchlorate anions, that is in accordance with the conclusions from this chapter.

5.5.1 Microcalorimetric investigations on different pyridine concentrations

Figure *5-9* displays the effect on the Peltier heat from varying the pyridine concentrations: 0, 0.1, 1, and 10 mM.

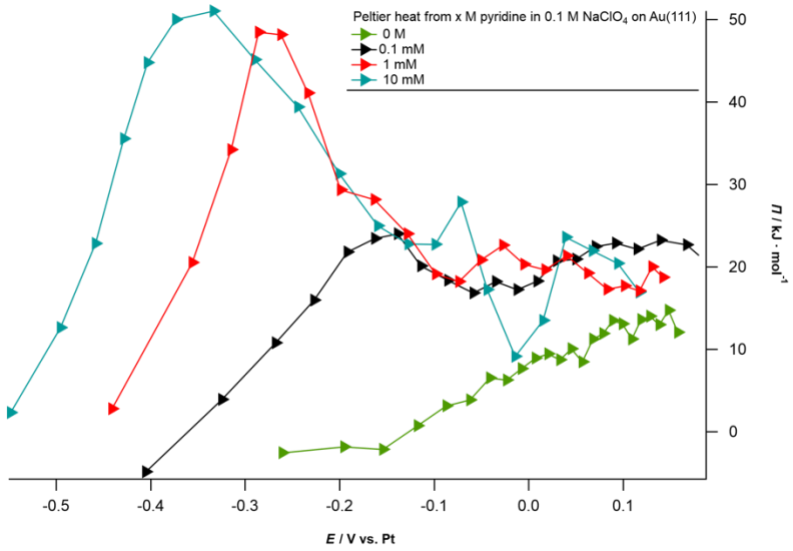

Figure 5-9 Influence of the different pyridine concentrations: 0 M (green triangles), 0.1 mM (black triangles), 1 mM (red triangles) and the 10 mM (turquoise triangles) over the Peltier heat.

By applying equation (7), it can be extracted that the change in the Peltier heat due to concentration changes, is in order of ±5 kJ mol^{-1}, by increasing or decreasing the concentration by a factor of 10. The large deviation of the Peltier heat when increasing the concentration from 0.1 mM to 1 mM originates probably from the small pyridine concentration and a larger amount of perchlorate anions in the double layer.

In Figure *5-9*, the red line refers to the pyridine concentration of 1 mM and the blue one for 10 mM. The maximum Peltier heat differs for 5 kJ mol^{-1} by increasing the concentration from 1 mM to 10 mM. However, for the concentration of 10 mM, an additional feature is observed at more positive potentials; the Peltier heat displays two maxima at –0.4 V (52 ± 5 kJ mol^{-1}) and at 0.03 V (25 ± 5 kJ mol^{-1}), and one minimum at 0 V, which was not observed for the lower concentrations.

From the data reported in this chapter, it is not possible to explain the behaviour of the heat for the 10 mM pyridine concentration. One can speculate that it is following the process that is happening for the 3rd anodic peak from the CV. To include or exclude that the process that happens more positively from the additional pyridine adsorption and phase transition peak, originates from anion co-adsorption, additional experiments are carried out with different electrolyte solutions.

5.6 Influence of the anion on pyridine adsorption

Additional microcalorimetric experiments in a solution of 0.1 M NaF on Au(111) were conducted to comprehend the influence of the anion towards the adsorption process of 10 mM pyridine on Au(111). The F^- anion was chosen because fluoride, like perchlorate, does not specifically adsorb [44, 60, 69]. Figure 5-10 depicts the cyclic voltammogram for an Au(111) electrode in a solution of 0.1 M NaF containing 10 mM pyridine. The CV curve displays one prominent peak at 0.1 V (vs Pt) in the anodic direction, as per the literature, and it is assigned to pyridine adsorption [61]. It is noteworthy that Terashima and Ikezawa performed reflection adsorption spectroscopic and differential capacity measurements to investigate the effect of halide anions on pyridine adsorption at the Au(111) electrode in neutral solutions, and they reported that the F^- anion does not interfere with the adsorption of pyridine [61].

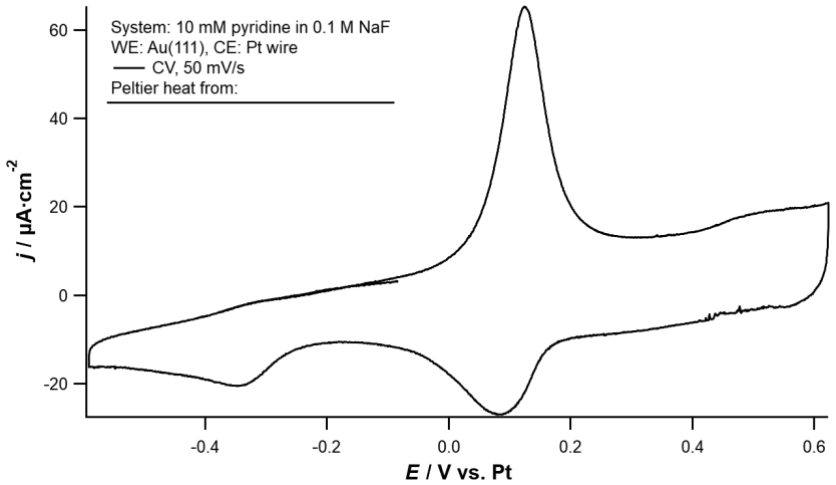

Figure 5-10 Cyclic voltammogram of Au(111) in 10 mM pyridine in 0.1 M NaF as supporting electrolyte, scanned with a rate of 50 mV/s. The main sharp peak at the anodic direction is assigned as pyridine adsorption and its phase-transition. The peaks at the cathodic side are counter peaks.

After the electrochemical measurements, microcalorimetric current pulse experiments were carried out by covering the whole adsorption region (from –0.4 V to 0.5 V vs Pt) on Au(111) in 10 mM pyridine in 0.1 M NaF.

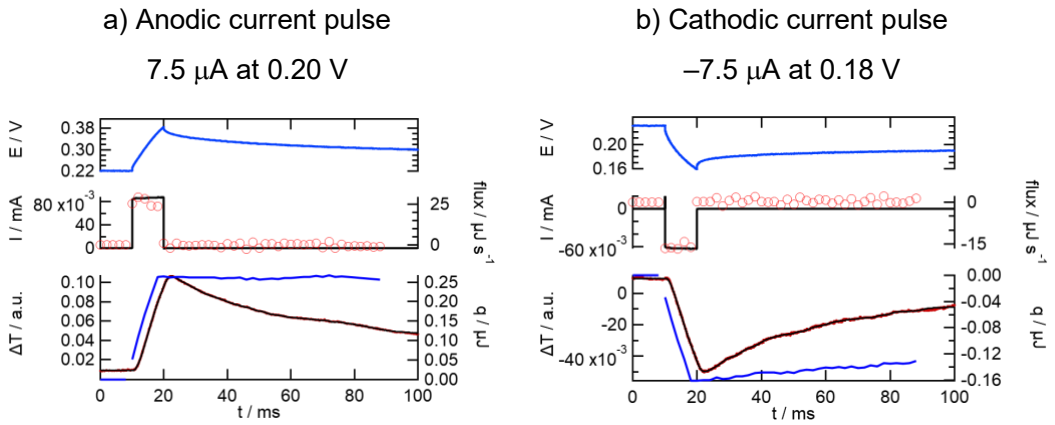

Figure 5-11 Potential, current, temperature transients, as well as the laser adjustment, the total heat and the heat flow of two current pulses of 10 mM pyridine adsorption (a; +7.5 μA) and desorption (b; –7.5 μA) on Au(111) in 0.1 M NaF as supporting electrolyte.

In Figure *5-11*, positive and negative current pulses from a series of continuous current pulses are displayed. The pulses represent the maximum or minimum molar heat observed. The application of a positive or negative current pulse leads to increasing or decreasing of the temperature transient, respectively. By applying a positive or negative pulse, the system heats up or cools down, in the given order.

Figure *5-12* displays the Peltier heat from the current pulses in anodic (red triangles) and cathodic (blue triangles) directions. The system heats up at a potential of about 0.22 V (vs Pt), where additional pyridine molecules adsorb on the Au(111) electrode. As a consequence, a maximum Peltier heat of 22 ± 5 kJ mol^{-1} is reached at about 0.22 V. In the NaF electrolyte consisting of 10 mM pyridine, a 3rd maximum at more positive potentials as a shoulder-like peak is not observed as seen for the perchlorate solution (cf. Figure *5-9*). Therefore, the shoulder-like peak can be related to the adsorption of the perchlorate anion on the Au(111) electrode.

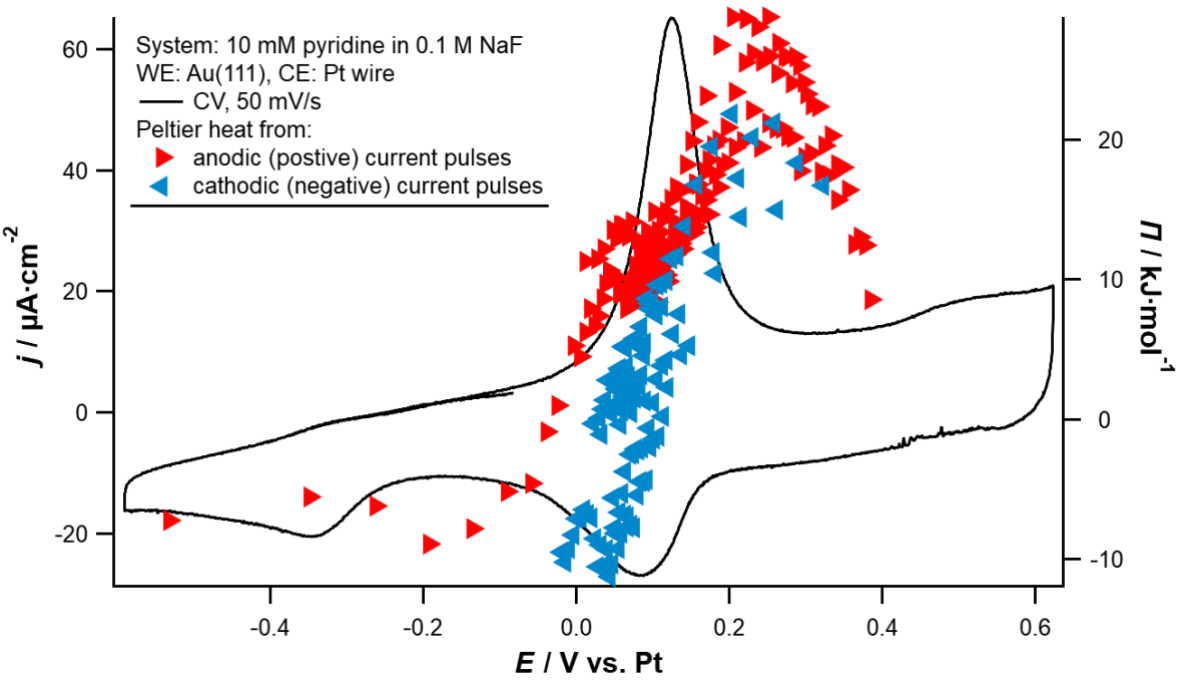

Figure 5-12 Plot of the CV and the Peltier heat from the consecutive current pulses versus the electrode potential for the system of 10 mM pyridine in 0.1 M NaF as electrolyte solution on Au(111) electrode surface. The red triangles represent the heat from the anodic current pulses with amplitude of 75 µA, the blue triangles are representing the heat from the cathodic current pulses with amplitude –75 µA. The black line is the CV recorded with a scan rate of 50 mV/s.

The maximum Peltier heat is much lower for the system consisting of 10 mM pyridine in 0.1 M NaF compared to 0.1 M $NaClO_4$ for the Au(111) electrode. The difference amounts to about a factor of two, considering that the maximum Peltier heat in $NaClO_4$ is in order of 50 kJ mol^{-1}. Towards the Peltier heat of the 10 mM pyridine in NaF, there is, as well, a contribution from the entropy of transfer, and it is calculated to be 2.4 kJ mol^{-1}. It is calculated by using the equation (9). The values needed for calculating the transfer number and the transfer entropy for each of the ions are presented below:

Ion	s_i^0 / J mol^{-1} K^{-1} [31]	$\hat{s}_i$ / J mol^{-1} K^{-1} [31]	λ_0 / S cm^2 mol^{-1} [55]
Na^+	36.8	7.10	50
F^-	56.5	11.4	55

According to the previous results, the Peltier heat would be approximately 20 ± 5 kJ mol^{-1} per mole per electron. Because of the lack of literature data for this

system, it is not easy to render concrete conclusions. However, this experimental data corroborated that a third peak for the system 10 mM pyridine in 0.1 M $NaClO_4$ solution most likely originates from the perchlorate.

5.7 Conclusions

By using electrochemical microcalorimetry, it was demonstrated that the Peltier heat could be measured for adsorption of an organic molecule, pyridine.

The microcalorimetric pulse experiments confirmed the reversible adsorption/desorption processes. The adsorption of pyridine on Au(111) occurs in the anodic direction of the potential scan. The positive or negative pulses lead to heating or cooling, respectively.

The differential capacitance data were obtained from the continuous current pulse experiments and the peaks are present as in the CV. Maximum Peltier heat that is observed coincides with the process of adsorption and phase-transition. The maximum Peltier heat for 10 mM is about 60 $\pm$ 5 kJ mol_e^{-1}. For the anodic direction, Positive Peltier heat leads to negative reaction entropy, therefore the total entropy is –201 J mol_e^{-1} K^{-1}. This entropy contains the contributions from the reaction entropy and entropy of transfer. The entropic contributions from the entropy of transfer are small, –6 J mol_e^{-1} K^{-1}. The determined reaction entropy seems to be rather low, –195 J mol_e^{-1} K^{-1} and refers to mole per electron.

By using the chronocoulometric data from Lipkowski, on the surface coverage changes with current density, it was estimate that around 2 mol of py per mols of electrons are involved. Therefore, it could be calculated the reaction entropy for pyridine adsorption process per moles of pyridine, $\Delta_R S \approx -98 \pm 20$ J mol_{py}^{-1} K^{-1}.

In order to disentangle the entropic contributions involved in the process, two cases were built: a thermodynamic cycle and a simpler model, where for both, it is assumed that the observed entropy change, in both sign and magnitude, is considered to arise primarily from the fixation of the pyridine molecules on the surface. Only a negligible contribution arises from effects such as coadsorption or conformational rearrangements. Regarding the solvation, the results suggest that pyridine remains solvated during adsorption, since complete desolvation would produce a substantially greater entropy loss.

Chapter 6 Thymine Adsorption on Au(111) from Aqueous Solutions

Thymine and the other DNA bases, adsorb on Au(111) by applying an electrode potential and form a well-ordered condensed monolayer to Au [8]. Au(111) electrodes coated with thymine are technologically very relevant for the future of the bio-nano sensors [10]. Therefore, this chapter is dedicated to the adsorption of thymine on Au(111) from aqueous solution. The chapter begins with a short literature review on the adsorption types of thymine on various metal electrodes.

In 1996, Kolb, Chosovich, and their co-workers examined the adsorption of thymine, uracil, 6–methyluracil, and 5,6–dimethyluracil from aqueous solutions on Au(111) and Ag(111) [62] by cyclic voltammetry, capacity measurements, and current transients to further explain the role of the electrode surface and intermolecular forces in the formation of ordered adlayers. From their study, they reported that the DNA bases adsorb on the Au(111) electrode surface in random, flat, and perpendicular orientations. According to their research, the flat adsorbed DNA bases form a physisorbed adlayer that is influenced by intermolecular forces, and the perpendicularly adsorbed molecules form a chemisorbed adlayer.

One year later, in 1997, Baumgaertel and his co-workers [63] examined the adsorption of thymine in $KClO_4$ as a supporting electrolyte, on gold single-crystal surfaces, Au(111), Au(100) and Au(210) by electrochemical methods (cyclic voltammetry and capacitance–potential measurements), *in situ* scanning tunneling microscopy (STM) and *ex situ* photoelectron spectroscopy (XPS). They varied the pH by the addition of concentrated $HClO_4$ or KOH. They confirmed the three different adsorption states: the random, the condensed, and the chemisorbed adlayer. The random and chemisorbed adsorption states occur on all electrodes, while the condensed state exists only on the reconstructed Au(100) and (111) surfaces. They also confirmed by XPS measurements that the transformation from condensed to chemisorbed state takes place via charge transfer from deprotonated thymine molecules on the gold surface. Additionally, the STM measurements showed two different ordered adsorption layers of thymine for the condensed and chemisorbed state. In the condensed state, the thymine molecules are flat-lying on the surface and in the chemisorbed state, the thymine molecules are upright standing connected via N(3) atoms to the surface. As well, they reported that in this second state, the thymine molecules form rows connected with hydrogen-bonded water molecules, and a

surface excess of 5.0 10^{-10} mol cm^{-2}, implying that the water molecules are coadsorbed in this region. It is worth mentioning that the above-mentioned behavior is pH-dependent. The higher the pH the less favored the chemisorbed adlayer is. That is because the preferred enol form of the thymine at higher pH. Confirmation on these conclusions was provided by Baumgaertel and co-workers [63]. They reported that the formation of chemisorbed film at positive potential is linearly dependent on the electrolyte pH, which indicated that the formation of this state is connected with the deprotonation of the adsorbed thymine presented with the following Mechanism 1:

$$R\text{–}NH_{(adsorbed)} \leftrightarrow RN^{-}{}_{(adsorbed)} + H^{+}(aq) + e^{-} \qquad \text{Mechanism 1}$$

This mechanism was confirmed by Zuman [64] by measuring the anodic polarographic activity of thymine and uracil only for their anionic form, and assigned the anodic polarographic wave to transfer about one electron.

Nichols and co-workers [65] investigated the adsorption of 10 mM thymine in acidic media, in 10 mM $HClO_4$, on Au(111) with *in situ* infrared spectroscopy. They reported that the physisorbed thymine shows no IR bands in the studied spectral region, consistent with a flat-lying adsorption geometry. The in-situ IR spectra of chemisorbed thymine were compared to IR spectra of metal coordination complexes of thymine and uracil, providing evidence that chemisorbed thymine bonds to the Au(111) surface through both carbonyl functionalities and a deprotonated N3 atom.

Kirste and Donner [66] studied the influence of the electrolyte resistance on the transient response in non-faradaic phase transition experiments of thymine on mercury and Au(111) electrodes by potentiostatic and impedance measurements. They have concluded that the adsorption and condensation current on a mercury electrode is only of capacitive nature and that on Au(111) is not possible to obtain negative adsorption/condensation currents because the formation of a condensed physisorbed thymine film on Au(111) is accompanied by a faradaic reaction forming the chemisorbed layer.

In the current contribution, electrochemical microcalorimetry is applied to provide knowledge about the heat generation in the electrode/electrolyte interface and the reaction entropy, where possible.

6.1 Cyclic voltammetry

In Figure *6-1*, a typical cyclic voltammogram of Au(111) in 10 mM thymine in 0.1 M $NaClO_4$ as a supporting electrolyte, recorded with a scan rate of 50 mV/s, is displayed. The CV obtained during the first cycle between –0.85 V and 0.40 V is almost identical to that reported by Roelfs et al. [63]. Following their interpretation, the thymine adsorption takes place in the anodic direction where two peaks are observed (c.f. Figure *6-1*). At electrode potential of –0.85 V, the thymine molecules are already randomly adsorbed on the Au(111) electrode surface and this region represents the adsorption Region I. The first T1 peak appears in the anodic direction as a small, broad peak at a potential of -0.63 V. T1 is assigned to the adsorption of thymine molecules and reorientation from randomly adsorbed to flat lying molecules on the Au(111) electrode surface [63].

The region between –0,55 V and –0.30 is the second adsorption region, II, where the thymine molecules are lying flat on the electrode surface, forming a condensed physisorbed adlayer. The molecular coverage at this region was investigated by Roelfs et al. [63] by *in situ* scanning tunneling microscopy, STM, and by Wandlowski [67] by *ex situ* photoelectron spectroscopy, XPS. Both groups have reported about 7.4 % of an ML is covered with thymine molecules. The coverage of thymine on the Au(111) surface has been determined to be around a densely packed monolayer, with the adsorption structure and bonding characterized using a combination of electrochemical, spectroscopic, and microscopic techniques.

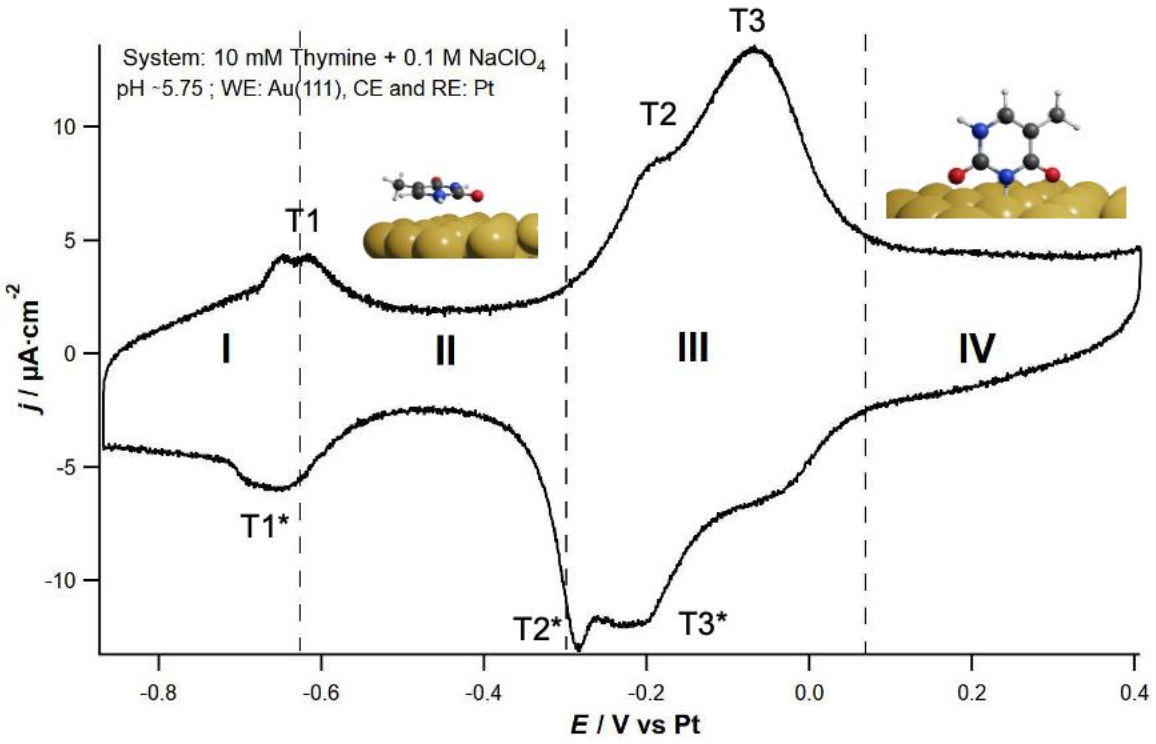

Figure 6-1 Cyclic voltammogram of Au(111) in 10 mM thymine and 0.1 M $NaClO_4$ as a supporting electrolyte in aqueous solution. The sweep rate is 50 mV s–1, and the pH is around 6. Adsorption occurs in anodic direction. The adsorption is divided into three regions, namely Region I) random adsorbed thymine molecules on the surface; Region II) physisorbed thymine molecules, flat-lying on the surface. The transition from region I to II is represented by the peak T1 – disordered phase transition. Region III) chemisorbed thymine molecules and 2D phase transition of the thymine molecules from flat-lying to perpendicular (Peaks T2 and T3); and lastly, chemisorbed thymine molecules at the Au(111) surface. In cathodic direction the reverse processes occur.

By positively increasing the electrode potential, in Figure *6-1* a broad, large peak, with two maxima is observed: the T3 maximum is more pronounced than the T2 maximum which is a shoulder-like peak of T3. The broad peaks cover the potentials from –0.3 V to 0.08 V, and represent the region III at the CV. This region III, is related to an additional adsorption of thymine molecules and lifting of the already flat adsorbed molecules in perpendicular orientation. The lifting of the thymine molecules is accompanied by a deprotonation reaction, where the thymine is chemisorbed on the Au(111) electrode surface. The coverage in Region III is increasing with increasing the potential, and 22% of an ML is occupied with perpendicularly chemisorbed thymine molecules [63]. The critical potential where the layers from region II to region III change is around the potential of zero charge, PZC (in this case is around –0.31 V vs Pt).

The last region observed from Figure *6-1* is the region that spreads between the potentials from 0.08 V and 0.40 V, and it represents a stable chemisorbed film, where the adsorbed thymine molecules are positioned perpendicularly on the Au(111) surface. A further increase of the electrode potential, above 0.4 V, leads to the oxidation of the gold.

In the cathodic direction, the opposite processes are taking place, giving rise to the cathodic peaks T3*, T2* and T1*. Donner et al. [68] concluded that the processes that are occurring on the anodic and cathodic side are reversible. The further decreasing of the electrode potential, below –0.9 V, leads to evolution of hydrogen.

6.2 Results from the Microcalorimetric Experiments

For the scope of this work, microcalorimetric pulse experiments were carried out for 10 mM thymine in 0.1 M $NaClO_4$, on Au(111) surfaces. The pH of the examined system was 5.75. For this system, sequences of continuous current pulse experiments were performed. The results are presented with a thymine concentration of 10 mM because if a lower concentration was used the peak of the transition from random adsorption to an ordered condensed layer on the surface, would not appear because the molecules at c < 1 mM cannot form a hydrogen-bonded network on the Au(111). For the concentration higher than 1 mM and lower than 10 mM, this transition peak is observable on single-crystal Au(111). The appearance of this peak in lower concentrations was not consistent since (111)-textured Au surfaces were used in the present work. Also, the intensity of other peaks in the CV will not be present at 0.5 mM thymine. As a supporting electrode, 0.1 M $NaClO_4$ is used because the anions do not specifically adsorb on the electrode surface.

6.2.1 Continuous current pulses

A series of continuous current pulses was applied, scanning the thymine adsorption region, starting from –0.85 V to 0.30 V and the desorption region from 0.30 V to –0.85 V. The duration of the pulses was 10 ms and the current amplitude was constant. For different sets of pulses, the current amplitude varied from ±30 to ±100 μA, with increments of ±10 μA. These current amplitudes are changing the surface coverage by only a few % of a monolayer per pulse. Before applying each set of positive pulses,

at an initial potential of –0.85 V, the cell was held for 5 minutes to ensure the maximum adsorption of thymine molecules at Region I.

In Table *6-1* the transients of a positive and negative current pulse with an amplitude of ±50 µA, respectively are shown. The pulses start from an initial potential around –0.62 V. These pulse transients represent the maximum temperature change in the region of –0.85 V to –0.30 V. The thymine adsorption is driven by the positive current pulses in the anodic direction, and the opposite process is driven by the negative current pulses in the cathodic direction.

Table 6-1 Potential, current, and temperature transients, as well as the laser adjustment (black line in the third panel), the accumulated heat (ink-blue line in the third panel) and the heat flow (red dots in the second panel) of two 10 ms long current pulses for the system 10 mM thymine / 0.1 M $NaClO_4$ on Au(111), with current amplitude of ±50 µA. The adsorption is driven by the positive pulses and the desorption by the negative pulses.

	a) Positive (anodic ⇒ adsorption) current pulse with amplitude 50 µA, flat lying thimine @ –0.62 V	b) Negative (cathodic direction) current pulse with amplitude –50 µA, @ –0.62 V
Region between I and II (T1/T1*)	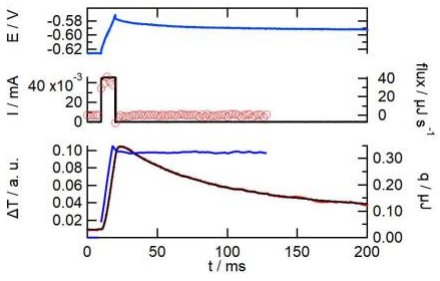	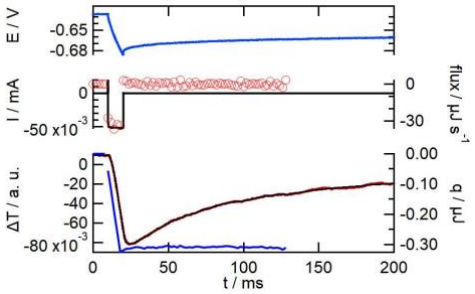

The potential (the ink-blue line in the upmost panel) and the current (the black line in the second row from each panel) transients represented in Table *6-1* follow the "standard" pulse shape, described in chapter 3. The electrode temperature transients (the red line in the third row from each panel) presented in Table *6-1* are linearly increasing or decreasing starting from the beginning of the pulse at t = 10 ms and are reaching a maximum or a minimum at around t = 22 ms, 2 ms after the end of the pulse at t 20 ms. The latter behavior is an indication that the process involved is reversible. In this case, the process involved in the peak pair T1/T1* is assigned as the adsorption of thymine molecules in flat orientation and reorientation of the already randomly adsorbed molecules.

The calorimeter was calibrated by following the procedure described in Chapter 3 to determine the total heat involved during the adsorption, reorientation and the opposite process. Table *6-1* displays exemplary calibrated data for the current pulses that were described above.

Table *6-1* also presents the heat flux (red dots in the second row in the panel) from the anodic current pulse at –0.62 V, following the current transient, and the heat transient (the ink-blue line at the third row from each panel) reaches its maximum shortly before t = 20 ms, and afterward stays at the same height. For the pulse in the cathodic direction, the reverse is encountered. Conclusions that can be made for this region are that the process is reversible, the 10 ms pulse was enough to drive the reaction, and that this process is fast. By applying the anodic pulse, the heat increases, i. e. the system heats up. By applying the cathodic pulse, the heat decreases, i. e., cooling of the system for the cathodic process. The molar heat obtained from the current pulses at this region is plotted in Figure 6-2, together with the results at other initial potentials.

6.2.1.b Perpendicular adsorption

In Table *6-2*, the transients of a positive and negative current pulse that represent the region from –0.30 V to 0.10 V are displayed.

Table 6-2 Potential, current, and temperature transients, as well as the laser adjustment (black line in the third panel), the accumulated heat (ink-blue line in the third panel) and the heat flow (red dots in the second panel) of two 10 ms long current pulses for the system 10 mM thymine / 0.1 M $NaClO_4$ on Au(111), with current amplitude of ±50 μA. The adsorption is driven by the positive pulses and the desorption by the negative pulses.

	a) Positive (anodic ⇒ adsorption) current pulse with amplitude 50 μA, flat lying thimine @ –0.20 V	b) Negative (cathodic direction) current pulse with amplitude –50 μA, @ –0.16 V
Region III (T2/T2* and T3/T3*)	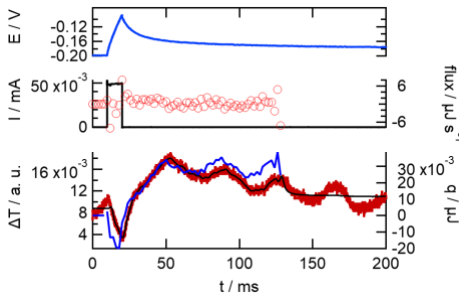	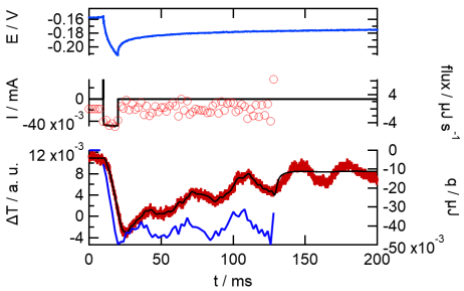

The potential (the ink-blue line in the upmost panel) and the current (the black line in the second row from each panel) transients represented in Table *6-2* are increasing (for positive pulse) or decreasing (for negative pulse) at the beginning of the pulse at t = 10 ms. The potential transient increases or decreases linearly during the pulse duration of 10 ms and reaches a max or a min at the end of the pulse at t = 20 ms, respectively. Afterwards, the potential transient relaxes. The current transient increases or decreases abruptly at the beginning of the pulse at t = 10 ms and stays at the same height during the pulse length of 10 ms. After the pulse, at t = 20 ms, the current transient reaches zero. The electrode temperature transient (the red line in the third row from each panel) presented in the same Table *6-2* for the positive pulse, is slightly decreasing and afterwards increasing. The total heat involved is much smaller compared to the one at –0.6 V. This can be an indication that in the anodic direction beside the process of thymine molecules adsorption, an additional process is taking place. This is in line with the explanation from Donner that parallel to the adsorption process, the deprotonation reaction of thymine is occurring.

To get the total heat involved during the adsorption and (desorption), the system was calibrated by following the procedure described in section 3.2.3. In the same Table *6-2* the calibrated data is presented. The heat transients follow the temperature one. The noise within them is due to a low signal-to-noise ratio. The molar heat obtained from the current pulses at this region is plotted in Figure 6-2 at section 6.3.

6.3 Molar Heat from the Microcalorimetric Measurements

In Figure 6-2 the CV and the molar heat obtained from both, anodic (red triangles) and cathodic (blue triangles) continuous current pulses are displayed. The Peltier heat is obtained by following the procedure from chapter 3. The values for the molar heat between the anodic and cathodic pulse series, are almost consistent with the exception of a slight deviation at the maximum area around –0.6 V. This consistency is a proof for the reversibility of the system and shows that the irreversible heat contributions are small. The slight deviation is probably originating from the fact that the anodic process is faster (transition from random to flat adsorbed thymine is a fast process) compared to the cathodic process (desorption of thymine molecules and the changing of thymine adsorption orientation).

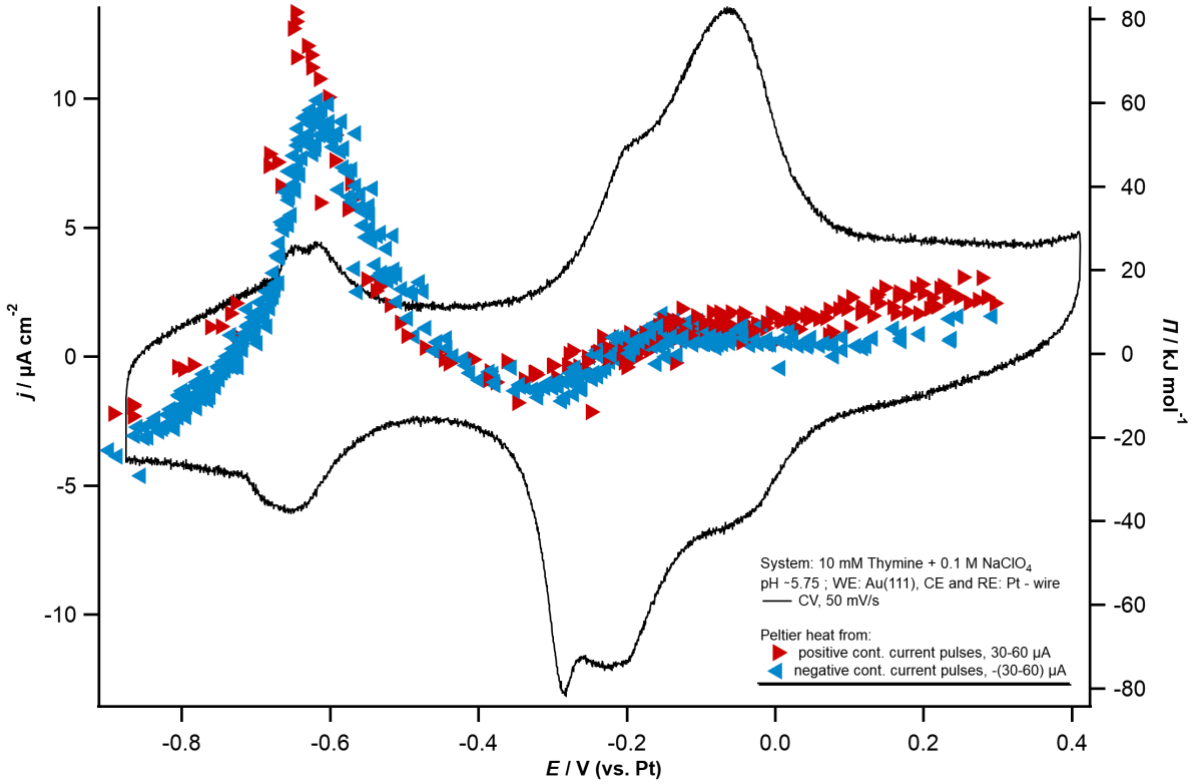

Figure 6-2 P Cyclic voltammogram of Au(111) in 10 mM thymine and 0.1 M $NaClO_4$ and the Peltier heat from the anodic (red triangles) and the cathodic (blue triangles) versus the electrode potential.

A maximum molar heat, of 70 ± 5 kJ mol^{-1}, is observed at around –0.6 V, i.e. at the transition region from I to II. It has to be stressed out that this molar heat refers to the moles per electron, and not to the moles of thymine molecule involved. At the

broader potential region between –0.4 V and 0.3 V, the molar heat is constant and it is around 10 ± 10 kJ mol^{-1}.

The potential scale in Figure 6-2 is given versus Pt pseudo-reference electrode. The potential axis of the CV was adjusted according to [68] so that the T1 peak matches the peak in the differential capacitance. The individual current pulse series were recorded consecutively over time which proves that there was no shift in the potential during the experiment.

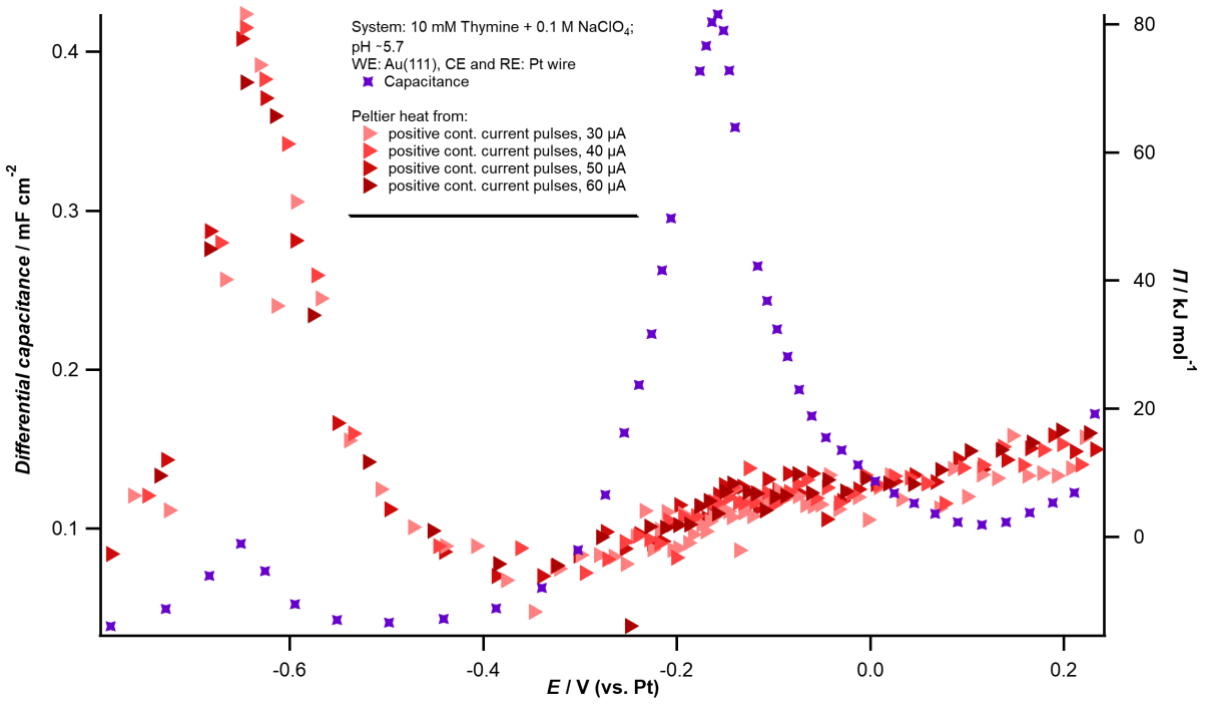

Figure 6-3 plot of the differential capacitance (the lilac stars: obtained from the difference in the current and the potential jump between two consecutive current pulses) and the Peltier heat (red triangles: current pulses with different pulse amplitudes) against the electrode potential.

In Figure *6-3* the Peltier heat from current pulse experiments, plotted versus the differential capacitance is displayed. The differential capacitance is obtained from the relationship of the difference between the current in the two consecutive current pulses and the resulting potential jump. The differential capacitance exhibits two maxima. The first one is at –0.63 V and the second one is at –0.18 V. The maximum Peltier heat of 70 ± 5 kJ mol_e^{-1}, is about at the same potential as the peak T1 (–0.63 V).

6.4 Experimental Reaction Entropy of the process

A maximum Peltier heat of about 70 ± 5 kJ $mol_{e^-}^{-}$ is encountered in the region between the thymine adsorption and the phase-transition between the randomly adsorbed thymine and the formation of the condensed physisorbed ad-layer where thymine is lying flat on the Au(111) surface. That would lead to an assumption that for the process of thymine reorientation with additional adsorption of thymine molecules, heat is transferred to the surroundings, which implies a reduction of the entropy upon the adsorption/reorientation processes. That conclusion aligns with the one for pyridine adsorption and its phase-transition.

The entropy determined from the Peltier heat is around –235 ± 15 J K^{-} $mol_{e^-}^{-}$, from which approximately –5 J K^{-} $mol_{e^-}^{-}$ belong to the entropy of transport. The significant reduction of about –230 ± 15 J K^{-} $mol_{e^-}^{-}$ refers to entropy per mole of electrons.

To determine the contribution per thymine molecule, the number of adsorbed molecules per transferred electron is needed. Up to current literature, there is no detailed information on the surface concentration on the charge density available for this system. Alternatively, the number of molecules of thymine adsorbed per electron, at the physisorbed region, can be estimated by using the charge density involved at that region.

The calculation is done by considering the charge density of 11 µC cm^{-2}. the potential of –0.6 V, the surface area of 0.2 cm^{-2} and the surface excess of 1.7 10^{-10} mol cm^{-2} [63]. It is assumed that the coverage increases from 0 to 7 % of a ML referenced to Au, for a potential increase from –0.5 V to –0.6 V with a corresponding charge density of 11 µC cm^{-2}. The charge density and the surface excess are taken from the capacitance data and the STM studies from [8] for the adsorbed thymine molecules at the physisorbed region, respectively.

According to the calculations ca. 4 molecules of thymine are adsorbed per transferred electron, which would lead to an approximate reaction entropy of $\Delta_R S \approx$ –60 J mol_{Thy}^{-1} K^{-1} referenced to the additionally adsorbed thymine.

6.5 Quantitative comparison of the experimental reaction entropy with the literature

Similarly, from the first glance, as in the discussion of pyridine adsorption, the reduction of the entropy would be expected because when the organic molecule is adsorbed in an ordered dense ad-layer, the molecular degree of freedom is expected to be lower compared with the dissolved ones.

To understand the reaction entropy calculated from the measurements, it is necessary to quantitatively compare it with a model built from the literature values. The most probable entropic contributions to reaction entropy (considering Chapter 4) are considered for the model, i.e.,

$$\Delta_R S = \Delta S_{Thy,adsorption} + \Delta S_{reorientation} + \Delta S_{waterstructure}$$

$\Delta S_{Thy,adsorption}$ refers to the entropy from the adsorption of thymine and $\Delta S_{reorientation}$ refers to the entropic contribution from the phase transition of the already adsorbed thymine molecules. This entropic contribution is most likely small, as it was the case for pyridine. And lastly, the contribution of the $\Delta S_{waterstructure}$. This contribution originates from the entropy involved in the change of the water structure upon adsorption of the thymine molecules. Towards the entropic contribution from $\Delta S_{Thy,adsorption}$ the process 6-1 is assumed:

$$\text{Thymine (aq)} \approx \text{Thymine (l)} + \nu H_2O \rightarrow \text{Thymine (s)} \qquad \text{Process 6-1}$$

Process 6-1, implies that the thymine adsorption occurs in two steps. The first step is the transfer of thymine from the dissolved state to a condensed liquid state, and the second step is the adsorption of the thymine molecule. Because in adsorbed state the molecules, in general, have a lower degree of freedom it might be safe to assume that when thymine is adsorbed, the molecules behave as in solid. Analogously, the entropy changes when going from liquid to solid state is known from the literature and is the entropy of freezing. As in the case for pyridine, this value has to be corrected for the room temperature and for the concentration. Starting from thymine in the liquid state (right-hand side of Scheme *6-1*), Scheme *6-1* involves the freezing of pure thymine from the liquid to the solid state.

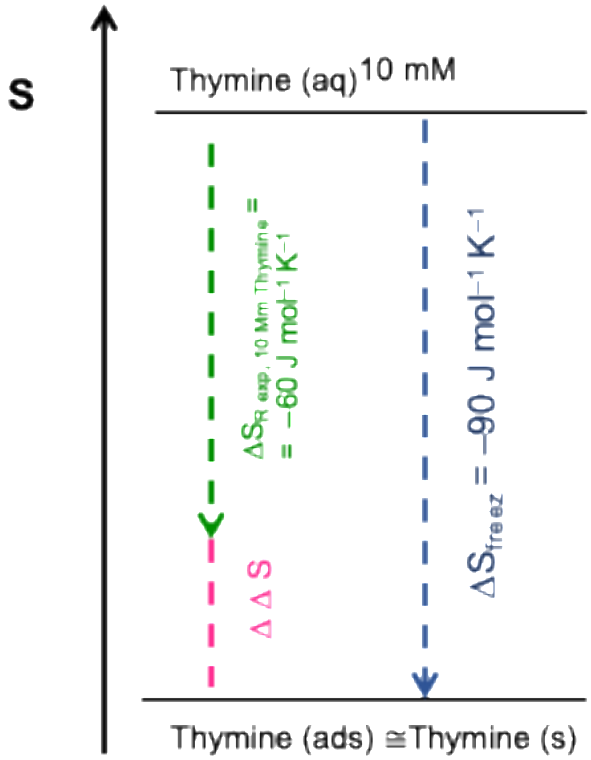

Scheme 6-1 Schematic model of the entropic state for the system of 10 mM thymine adsorption on Au(111). The blue arrow facing down indicates the entropy of freezing that is corrected for the temperature and concentration, $\Delta\ S_{freeze}^{298\ K} \sim$ –90 J mol_{Thy}^{-1} K^{-1}. The green arrow facing down, represents the entropy of reaction that is calculated from the microcalorimetric measurements. The pink line indicates the discrepancy of 30 J mol^{-1} K^{-1}. In all cases the pressure is 1 atm at 298.15 K.

The entropy of freezing, $\Delta S_{thymine,freez}$ for pure thymine solution is –54.5 J $mol^{-1}_{thymine}$ K^{-1} [54], and needs to be adjusted for room temperature, 298.15 K. The conversion can be done by using Kirchhoff's law:

$$\Delta S_{thymine,freezing}(298.15\ K) = -\int_{298\ K}^{T_m} \frac{(c_{p,l}-c_{p,s})}{T} dT + \Delta S_{thymine,\ freezing,\ Tm}$$

where, $c_{p,l}$ and $c_{p,s}$, are heat capacities of the liquid and solid state, respectively. Their variation with the temperature according to the experimental values for thymine from [54] is linearly approximated, which could lead to an error. However, this error is very small. The values are summarized in the Table below:

	Thymine
T_m / K	321.3
$\Delta S_{thymine,melting,Tm}$ (J $mol^{-1}K^{-1}$)	54.5
$c_{p,l}$ (T_m) (J $mol^{-1}K^{-1}$)	198
$c_{p,s}$ (T_m) (J $mol^{-1}K^{-1}$)	150
$c_{p,l}$ $(298.15)^{1atm}$ (J $mol^{-1}K^{-1}$)	163
$\Delta S_{thymine,\ freez,\ 298.15\ K}$ (J $mol^{-1}K^{-1}$)	–53.5

The correction from the concentration is ambiguous since thymine itself is a solid compound at standard conditions, and the term "pure solution" typically refers to a homogeneous mixture. Therefore, it could be assumed that the change in the entropy from the change of the concentration comes from setting free of the thymine in solid state and its dilution:

$$\Delta S_{sol,10\ mM\ thymine} = s^0_{thymine(s)} - s^0_{thym(aq)nWater} + R\ln c_{thyminey(s)} + R\ln c_{thymine(aq)nWater}$$

$$= (-53.5 + 0 - 38.3)\ J\ mol^{-1}\ K^{-1} \approx -93.8\ J\ mol^{-1}\ K^{-1} \approx -90\ J\ mol^{-1}\ K^{-1}$$

By applying those corrections, the entropy of freezing is $\Delta\ S^{298\ K}_{freeze} \sim$ –90 J mol^{-1}_{Thy} K^{-1}. The negative sign of the estimated entropy is expected because upon freezing the thymine molecules, they lose the degree of freedom and become more ordered.

There is a discrepancy of ca. –30 J mol^{-1}_{Thy} K^{-1} between the reaction entropy from the microcalorimetric experiments and the entropy of freezing estimated from the literature data. Considering the rather rough approximations for estimating the entropy

of reaction per mole of thymine this discrepancy seems acceptable. Other effect that may contribute are:

- The reorientation entropy should have a small impact on the overall entropy because the thymine molecules at the double layer are already randomly adsorbed.
- The entropic effects of thymine on the water are not known. The thymine molecule has a hydrophobic and a hydrophilic part. This implies that upon entering the thymine molecules into the water solution, the effect towards the surrounding water molecules could lead to a decrease or increase of water structure entropic contributions.
- The approximation that the adsorbed thymine losses the degree of freedom. The adsorbed thymine maybe does not lose the rotational degrees of freedom while physisorbed on the surface.

Despite the differences, this rough model agrees with the experimental one, and endorses the conclusion on the entropic contributions to pyridine molecule adsorption. From here, it can be extracted that the dominant contribution to the reaction entropy for the process of thymine adsorption on Au(111) originates from the fixation of the adsorbed thymine molecules on the metal surface.

Quantitative comparison of the experimental reaction entropy with the literature at the region of thymine chemisorption is not easy. From Figure *6-3*, a Peltier heat of about 5 $\pm$ 10 kJ $mol_{e^-}^{-1}$ is encountered in the region between the thymine adsorption and the phase transition of the flat-laying thymine molecules to perpendicular thymine orientation. This region is covered in the potential of –0.35 V to 0.40 V. The formation of the chemisorbed phase is a complex process that occurs alongside the lifting of the surface reconstruction [68]. The irreversible contribution towards the measured heat, calculated according to Chapter 2, is of the order of 5 kJ $mol_{e^-}^{-1}$. This implies that no net heat contributions are present, and therefore there is not net contribution towards the reaction entropy change. That is not expected because in this region (II $\rightarrow$ III) there is an increase of the thymine molecules from 7% to 22% of a ML (referenced to Au). However, it is known that no net reaction entropy indicates that the entropies of the processes involved in that region are either small or cancel each other.

Possible entropic contributions to reaction entropy are:

i. Thymine molecules are adsorbed in this region in a perpendicular orientation. This process is the fixation of the thymine molecules and leads to decreasing the entropy, as already seen by the example of pyridine adsorption, and thymine adsorption at lower potentials.

ii. Already adsorbed thymine molecules reorient from flat-lying to a perpendicular orientation on Au(111). It can be expected that the sign of the entropy change for the reorientation is slightly positive and this contribution is rather small as it was already seen in the region I→II and for the pyridine adsorption.

iii. The thymine molecules are deprotonated upon the adsorption. It is not known whether the deprotonation reaction leads to decrease or increase of the entropy [6]. Evidence that this region is accompanied by a chemical reaction is provided by the behavior of the total heat from the positive current pulses that were applied for this region (cf. Table *6-2*). It indicates the presence of parallel processes.

iv. From my data, it is not possible to get information about the sign and the entropic effects from water on the surface and in between the chemisorbed deprotonated thymine molecules, or from the surface reconstruction.

v. However, the reaction entropy of the adsorbed thymine for this region can be estimated. This can be done if it is considered that the charge in region III is 4 times larger than the charge involved in the transition from I to II region; and the change of the coverage of the adsorbed thymine molecules in region III is 15 % of a ML (referenced to Au), compared with 7% in I→II. This would lead to an entropy of ca. –30 J mol_{Thy}^{-1} K^{-1}.

6.6 Conclusions

Electrochemical microcalorimetry has been used to assess the Peltier heat and the reaction entropy upon thymine adsorption on Au(111) -textured films from aqueous solutions. The adsorption of thymine occurs in anodic direction and the desorption in cathodic one.

From the microcalorimetric experiments heating upon the adsorption and cooling for the reverse process has been observed. This behavior is a confirmation that the adsorption and the desorption of thymine on Au(111) is a reversible process.

The maximum Peltier heat of about 70 kJ mol^{-1} was observed at the adsorption region II. The Peltier heat corresponds to a net entropy of –235 ± 15 J K^{-} $mol_{e^-}^{-}$. The negative sign of the entropy is expected because there is a formation of a densely packed condensed layer at this region. The entropy of transfer is rather low, –5 ± J K^{-} mol^{-1}. Therefore, the reaction entropy is –230 ± 15 J K^{-} $mol_{e^-}^{-}$.

There are 4 thymine molecules adsorbed per transferred electron and the reaction entropy per additionally adsorbed thymine is –60 J mol_{Thy}^{-1} K^{-1}.

In order to disentangle the entropic contributions in the reaction entropy a simple model was built for which it was approximated that the thymine molecules behave as solid when adsorbed on Au(111). The transition from liquid (solvated thymine) to solid thymine molecules is represented by the entropy of freezing, –90 J mol_{Thy}^{-1} K^{-1} at 298 K.

The rough model fits well with the experimentally determined reaction entropy. This leads to the conclusion that the adsorption of thymine molecules from aqueous solution dominates the entropy change of the process.

The discrepancy of 30 J mol_{Thy}^{-1} K^{-1} is acceptable considering the rather rough approximations for estimating the entropy of reaction per mole of thymine. However, there are several entropic contributions that could be taken into account: the changes of solvation of thymine upon adsorption, and the water structure effects on the adsorbed thymine molecule. There is a rather small contribution from the reorientation of the thymine molecules from randomly adsorbed to flat lying on the gold electrode.

At the regions III and IV, where thymine is chemisorbed to Au(111), there is no net heat contribution. Therefore, the reaction entropy is zero. Probably the entropic contributions from the processes cancel each other. The processes involved are:

- lifting of the adsorbed thymine molecules from flat to perpendicular orientation on Au(111). This process should slightly increase the entropy, as already confirmed for the reorientation at more negative potential;
- additional adsorption of thymine molecules, which should lead to negative entropy, as already observed at the more negative potential and for the adsorption of pyridine on Au(111);
- it is hard to access the entropy sign for the deprotonation of thymine upon the chemisorption and the influence of the water structure on the system. The deprotonation reaction of thymine decreases further the entropy.

  The charge involved in region III is four times larger than the charge involved in I→II. As well, the thymine coverage changes double, from 7% to 15%, in this region which would lead to a reaction entropy of –30 J mol_{Thy}^{-1} K^{-1}.

The entropic contribution of the adsorption of additional thymine molecules and the lifting of the already adsorbed ones' deprotonated reaction cancels each other.

Chapter 7 Overpotential and Underpotential Deposition of Pb on Au(111) – A Microcalorimetric Investigation

This chapter covers the microcalorimetric investigation of overpotential and underpotential deposition of Pb on Au(111) from aqueous solutions.

The initial step in the electrochemical deposition of a metal, in this case, Pb, is the formation of metal adatoms on the foreign substrate, in this study on Au(111). The potential-driven deposition of a surface monolayer at potentials positive to the electrode potential for the reversible bulk deposition of the adsorbate is known as underpotential deposition, UPD. This implies that a Pb monolayer is formed on the Au(111) surface. The bulk, or the overpotential deposition, OPD, occurs when an overpotential is applied at potentials negative to the reversible electrode potential of the Pb^{2+}/Pb couple in that solution. In this case, Pb is cathodically deposited on top of the Pb monolayer from a solution containing Pb^{2+}ions.

The electrodeposited Pb on Au(111) is a good example of a system that grows according to the Stanski-Krastanov mechanism [73]. Stranski-Krastanov growth mode happens when a 3D island is formed on top of a predeposited 2D metal monolayer [70]. For well-ordered 2D UPD metal adlayers to be formed, it is necessary for the metal-substrate interaction to be strong and the metal-substrate to have a high misfit, which is the case for Pb-Au. These 2D UPD metal adlayers can act as precursors for the subsequent nucleation and growth of a 3D metal phase in the OPD range [70].

The metal deposition and dissolution of metal atoms on foreign metal substrates is an interesting system for research in the frame of interfacial electrochemistry by both, scientists and engineers, because of its wide usage. One very attractive aspect of Pb UPD on Au(111) is its enhanced catalytic activity for oxygen reduction at submonolayer coverage [71]. The Pb OPD can be generally used as a calibration system. Therefore, the system Pb UPD and OPD on Au(111) is chosen for further microcalorimetric investigations.

7.1.1 Pb overpotential deposition on a monolayer of Pb from aqueous solution

The overpotential deposition, OPD, of lead on Au(111) surfaces, i.e., lead deposition at a more negative potential than the Nernst potential, has been studied much less than Pb UPD. In this case, Pb is cathodically deposited on top of the Pb monolayer from a solution containing Pb^{2+}ions. The substrate, Au(111), in this case, is completely covered by Pb adatoms, where only the interactions of solvent–Pb adatoms are present [72]. The electrodeposited Pb on Cu or Au is a good example of a system that grows in the Stranski-Krastanov mode [73, 74]. The Stranski-Krastanov mode is when the growth on the 2D layer formation from the UPD monolayer is followed by 3D island nucleation and growth. Henzler et al. [74] studied the epitaxy of Pb on Cu(111) at different temperatures with spot profile analysing LEED (SPA-LEED) in vacuum. For the Pb_{OPD}/Cu(111), they have reported that the growth is bulk-like in a layer-by-layer mode at low temperatures (T = 200 K) and in 3D islands at T>300 K. Schwarzacher and Wu [73]studied the effect of halide additives on the electrodeposition of Pb on polycrystalline Au by using ex situ AFM, SEM and in situ oblique incidence reflectivity difference (OIRD) measurements. By combining those techniques, the authors provided a detailed characterization of post-growth sample morphology and the morphological differences between films deposited in the absence or presence of strongly adsorbing halides during the film growth [73]. From their study, it can be concluded that the halide additives strongly modify the growth mode of the Pb OPD on polycrystalline Au and that in solutions containing weakly adsorbate F^- and additive-free electrolytes, a higher density of facetted sub-micron size islands formed. In a case, when the solution contains a strong adsorbate, such as Cl^- and Br^-, a low density of micron-sized irregularly shaped Pb islands or clusters of islands forms. The change in the growth mode could be related to the blocking of Pb nucleation sites by the strongly adsorbed anions.

In this thesis, the microcalorimetric investigation of the bulk deposition of Pb_{OPD}/Au(111) was conducted to enhance the understanding of the deposition process and serve as valuable calibration data for future studies in this field.

7.1.2 Pb underpotential deposition on Au(111) from aqueous solution

One of the first ever studied UPD systems is the deposition of radioactive Ag on polycrystalline Au and Pt by Rogers et al. [75]. Later on, Lorenz et al. [76] performed series of experimental studies on UPD of metals from which knowledge of the thermodynamic and kinetic properties of UPD in several substrate/adsorbate systems has been accumulated by a number of researchers [77–79]. Kolb and his co-workers were the first that provided a significant progress in the theory of UPD by introducing the concept of underpotential shift in order to describe the thermodynamic properties of UPD. The fundamental idea of UPD is of practical interest because it is crucial for various electrochemical fields, including electrodeposition, electrocatalysis, corrosion and supercapacitors. One of the most attractive aspects of UPD is its influence over the electrocatalysis of organic substances. Already half a century ago, Beden et al. [80] showed that the underpotentially deposited metal atoms such as Pb and Bi enhance the electrocatalytic activity of the Pt electrode for the oxidation of methanol, making the system Pb UPD even more interesting for further studies.

The UPD of Pb has been considered as a model system for understanding the earliest stages of metal electrodeposition, used to evaluate the crystal structure and surface area of Au substrates, and employed in calibrating many electrochemical techniques [81]. The Pb UPD process has been extensively studied by electrochemical, STM, SHG, X-ray adsorption spectroscopy, X-ray scattering, and UHV techniques such as low-energy electron diffraction and Auger electron spectroscopy, on various electrodes, such as: Au(h,k,l) electrodes [82–88], as well on Ag(h, k, l) [89–96], on Cu(111) [97], and on Pt(111) [98, 99]. The Pb UPD on different surfaces exhibits different thermodynamic and kinetic characteristics. Regarding the catalytic activity, Juettner [12] studied the oxygen reduction on Pb UPD-modified Au electrodes and showed that the three low Miller index faces of Au electrodes catalyze the peroxide electroreduction at different rates. The modified surfaces of Pb_{UPD}/Au(111) and Pb_{UPD}/Au(100) exhibited larger electroreduction than Pb_{UPD}/Au, and Pb_{UPD}/Au(110) and Pb_{UPD}/Au(111) had the largest degree of enhancement. Regarding the cyclic voltammetric measurements, the Pb_{UPD} depends strongly on the substrate and the crystallographic orientation [100]. The Pb_{UPD}/Au(100) [84], Pb_{UPD}/Au(110) [101], Pb_{UPD}/Cu(111), or Pb_{UPD}/Ag(111) [102] is reversible and does

not form islands. Conversely, the Pb_{UPD}/Au(111) voltammetry exhibits is irreversible. The irreversible nature of this system has been linked to:

i) Surface reconstruction processes that lead to more stable adsorbate states [100];
ii) Dissolution of Pb atoms from Au(111) terraces [101];
iii) Stripping of the irreversibly deposited Pb from Au intracrystalline boundary sites [103];
iv) Change in Au d-band structure due to adsorption [104].

However, Vasiljevic and Szczepanska [81] demonstrated that the peak irreversibility comes from the surface structural changes due to the Pb dealloying from the top substrate layer by examining the surface alloying during Pb_{UPD}/Au(111). They reached this conclusion by applying two electrochemical approaches: extended polarization at high Pb coverage of 0.85 ML and repeated cycling 1150 times between the potentials where the surface is covered with 0.25 ML and 1 ML [81].

Even though thorough research is done for the Pb_{UPD}/Au(111), open questions remain. For example, there is no information on the heat involved during the deposition/dissolution of Pb on Au(111). Knowledge of the heat involved during this process is important for further study of the catalytic activity of the aqueous fuel cells. In addition, the Peltier heat provides direct access to the reaction entropy by applying electrochemical microcalorimetry. Disentangling the entropic contributions in this system will enrich the fundamental understanding and help build more precise models.

7.2 Results from Microcalorimetric Experiments

The results presented in this chapter are for the overpotential and underpotential deposition of 10 mM $Pb(ClO_4)_2$ in 1 M $HClO_4$ as supporting electrolyte, on Au (111)-textured films. The system is studied in acidic media because the catalytic activity is most pronounced [80]. Another reason for that is derived from the Pourbaix diagram of the studied system [105] – showing that only Pb^{2+} species are present for the potential region of our interest in aqueous solution in low pH, and at room temperature. The perchlorate anion was chosen because Schmidt et al. [100] demonstrated that there is no anion-coadsorption in the overall underpotential range of this system. The kinetics of electrodeposition/desorption, as well as the resulting structures, are dependent on the nature and the concentration of the anions. In the presence of weakly adsorbing anions, such as perchlorate, the kinetics of deposition/desorption is slow, and in the presence of specifically adsorbing anions, the kinetic is much faster, ascribed to the formation of coadsorbed metal-anion layers [100].

The results on Pb_{OPD} and Pb_{UPD}/Au(111) are presented in two subchapters. In chapters 7.2.1a and 7.2.1b, cyclic voltammetry is shown for the systems, respectively. Electrochemical measurements are obtained to corroborate the previous findings and for surface characterization. In the second subchapter, 7.2.2, the data obtained from the microcalorimetric experiments are presented.

7.2.1 Cyclic voltammetry

7.2.1a Cyclic voltammetry of Pb_{OPD}

Figure *7-1* presents the cyclic voltammogram for the Pb OPD from 10 mM $Pb(ClO_4)_2$ in 1 M $HClO_4$ aqueous solutions, in acidic media. The CV is recorded starting from the cathodic direction with a sweep rate of 50 mV/s. On the cathodic direction occurs the deposition, and at the presented CV, around 300 ML of Pb were deposited. That was done by holding the system at a potential of –0.08 V (vs Pb^o/Pb^{2+}) for several minutes. The equivalent thickness of the deposited Pb films was calculated by integration of the deposition current normalized by a charge of 302 μC cm^{-2} corresponding to an "ideal" ML of Pb(111) [81] at a potential of –0.08 V (vs Pb^o/Pb^{2+}) for several seconds. Afterwards, the scan continued, and the potential was swept towards the dissolution

site. By bulk depositing the Pb, the p.z.c. of the system was changed to –0.03 V, as indicated in the literature [70].

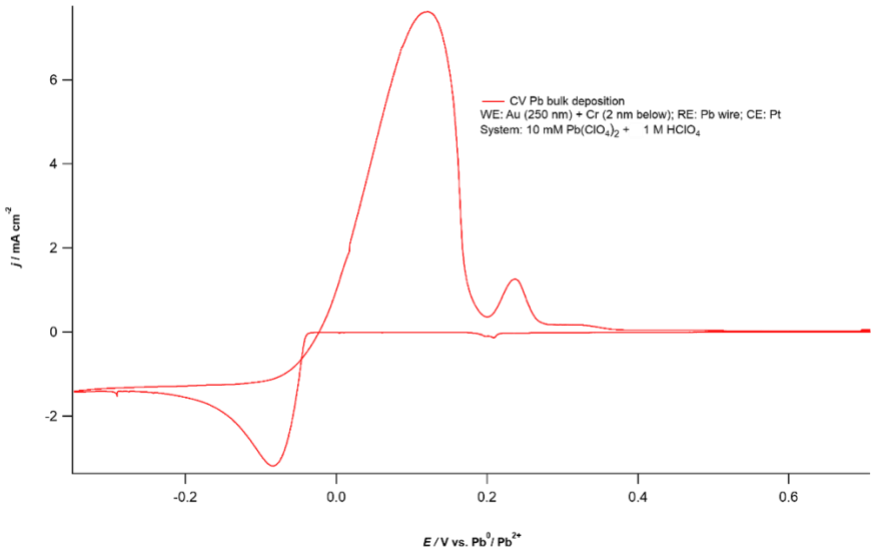

Figure 7-1 Cyclic voltammogram of Au(111) in 10 mM $Pb(ClO_4)_2$ / 1 M $HClO_4$ (recorded with a scan speed of 50 mV/s) versus the electrode potential (vs Pb^o/Pb^{2+}). The large cathodic broad peak at –0.08 V represents the bulk deposition. The large anodic peak, at 0.1 V is the dissolution of lead. The peak pair at 0.23 V, with a prominent anodic peak corresponds to Pb underpotential deposition.

From Figure *7-1* in cathodic direction, the small cathodic peak that occurs at 0.2 V (vs Pb^o/Pb^{2+}) is the deposition of Pb on Au(111), with the formation of a full monolayer of Pb on the Au surfaces at about 0.1 V. The monolayer formation was confirmed by STM and AFM measurements performed by Gewirth et al. [11]. They reported that the full monolayer of Pb adatoms forms a hexagonal closed-packed layer that is rotated by 4.5° relative to the Au(111) substrate. With further decrease of the electrode potential, a Moiré pattern rises, and a dominant broad peak is observed at –0.08 V. This peak is from the deposition of further lead atoms from the solution on top of the Pb monolayer, i.e., the deposition becomes diffusion-limited. The counter peaks corresponding to the bulk and Pb UPD dissolution are seen during the anodic scan. The loop between the cathodic and anodic current originates from the nucleation time needed for the bulk growth to start [106].

The cyclic voltammogram for the system Pb_{OPD}/Au(111) in Figure *7-1* is very similar to the one reported for Pb_{OPD}/Cu(111) and other single crystal substrates [106]. The CV reported by Schwarzacher and Wu [107] for the system of Pb_{OPD}/ polycrystalline gold has two pronounced bulk dissolution peaks for the solutions with

non-adsorbing anion present, and the CV has one pronounced bulk dissolution peak for the solutions containing specifically adsorbed ions. According to their study, the presence of the strong adsorbate Cl^- and Br^- affects the Pb_{OPD} growth.

7.2.1b Cyclic voltammetry of Pb_{UPD}/Au(111)

In Figure 7-2, a typical cyclic voltammogram recorded with a scan rate of 50 mV/s of Au(111) in 10 mM $Pb(ClO_4)_2$/ 1 M $HClO_4$ is displayed. The CV obtained during the first cycle between 1.4 V and 0.05 V is almost identical to that reported by Hamelin [82].

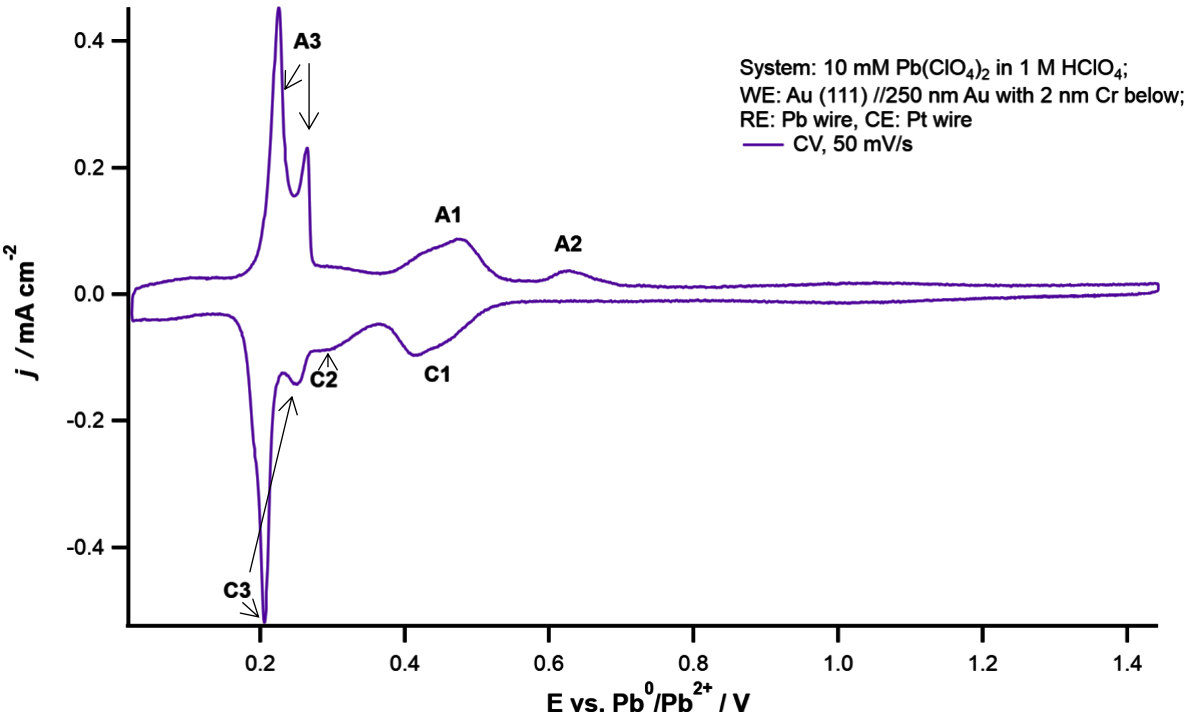

Figure 7-2 Cyclic voltammogram of Au(111) in 10 mM $Pb(ClO_4)_2$ / 1 M $HClO_4$ during Pb_{UPD} on (111)-textured Au film. CV is scanned with 50 mV/s. The deposition happens in cathodic direction and it is characterized by the peaks C1, C2 and C3 at 0.45 V, 0.30 V, and 0.22 V (vs Pb^o/Pb^{2+}), respectively. A full Pb ML is completed after the peak C3. In the anodic direction, the desorption / dissolution occurs, which is characterized by the peaks A3, A1 and A2 at 0.22 V, 0.45 V and A2 0.63 V (vs Pb^o/Pb^{2+}), respectively. A2 is the counter peak of C2 and is assigned as surface dealloying process.

The Pb UPD process takes place at electrode potentials where the hydrogen evolution reaction, HER, on gold, occurs. However, the presence of lead in the electrode surface greatly inhibits the HER, as would be expected given the high overpotential for the hydrogen evolution on bulk Pb electrodes [108]. The deposition of Pb happens in

the cathodic direction. Therefore, starting from a bare Au surface at 1.4 V (vs Pb^{o}/Pb^{2+}) with decreasing the potential the formation of the first pair peaks, C1 with its counterpart A1 (the small broad cathodic peak) is observed at 0.45 V (Pb^{o}/Pb^{2+}). The C1/A1 pair corresponds to Pb adsorption/desorption at step edges [82].

The second peak, C2, is not well defined. C2 spreads from 0.35 V to 0.22 V (vs Pb^{o}/Pb^{2+}) and has a counter peak, A2, at 0.62 V (vs Pb^{o}/Pb^{2+}) - a potential even more positive than the peak pair A1/C1. This pair of peaks exhibit irreversible behaviour. By conducting an STM study, Green and Hanson have shown that surface-alloying occurs at about this potential and the alloying is limited to a low coverage of Pb on Au(111) [109]. Vasiljevic and Szczepanska [81] demonstrated that, indeed, the peak A2 (@ 0.65 V) is Pb “dealloying” from Au(111), which occurs only for Pb_{UPD}/Au(111). With further decrease of the potential, at about 0.22 V a very sharp peak with a small shoulder-like shape, C3, appears. C3 is attributed to the Pb deposition on Au terraces. This conclusion was made based on the STM measurement done by Green et al. [86]. By further decrease of the potential, the nucleation and growth of hcp Pb islands, and the formation of a full Pb ML on Au(111) was observed by STM [110] and AFM [11]. The counter peak of C3 is A3. The A3 has a characteristic double-split peak structure, which is attributed to Pb dissolution from two energetically different sites of regions on the surface. Upon the completion of the Pb UPD, Crepaldi et al. [111] observed a Moire unit cell on the surface of around (5.77×5.77)R21.5° with respect to the Au(111) substrate by applying angle-resolved photoelectron spectroscopic (ARPES) and STM measurements.

Figure *7-3* shows CVs with a set of scans with different negative potential limits, which shows the irreversible nature of the surface alloy formation (the peak set C2/A2). This is intended to help the reader to observe the potentials at which the peaks and their counterparts appear. As well, the set of CVs is almost identical to that reported by Vasiljevic [81], with the same sweep rate.

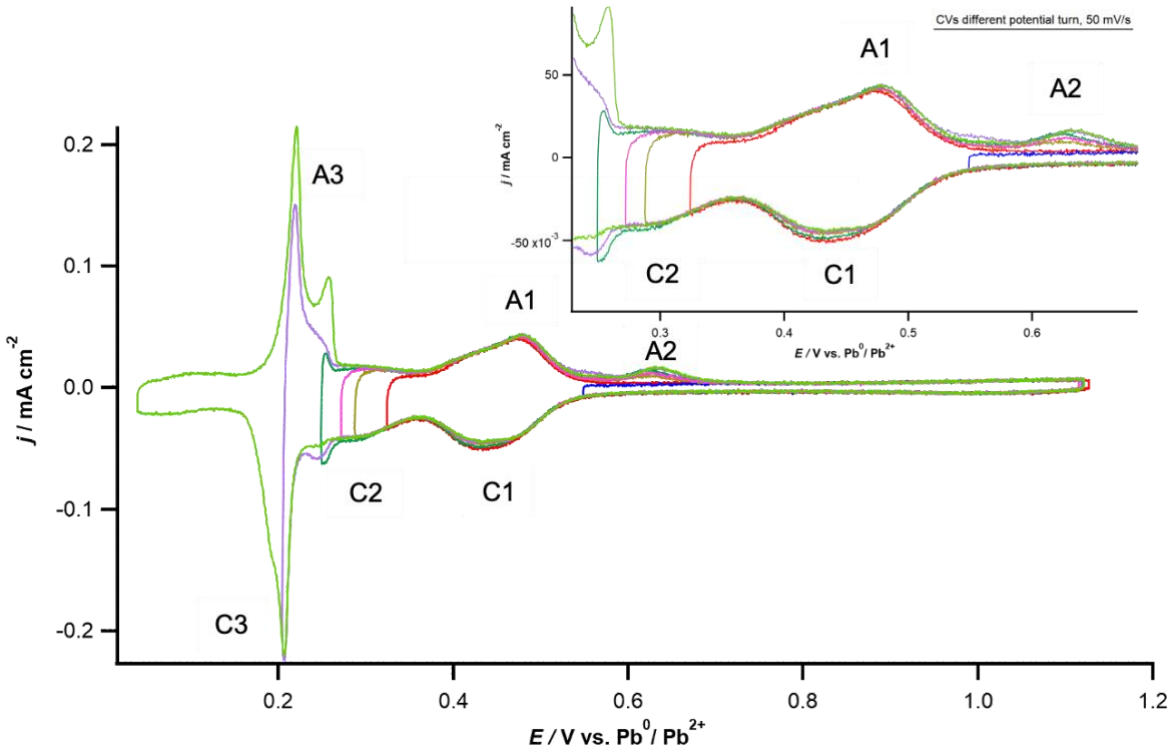

Figure 7-3 Cyclic voltammogram of Au(111) in 10 mM $Pb(ClO_4)_2$ / 1 M $HClO_4$ recorded with 50 mV/s, scans with constant positive potential limit (1.12 V) and varying negative limit until: 0.55 V (blue line), 0.32 V (red line), 0.30 V (olive-green line), 0.28 V (pink line), 0.25 V (forest green line), 0.22 V (lilac line) and 0.02 V (light green line), recorded sequentially.

From Figure 7-3, it can be clearly noticed that peak A2 appears only when the potential was swept to 0.3 V or lower before, i.e., when peak C2 was reached. Another conclusion is that peak A3 splits as soon as a complete ML is formed.

The CV peaks' height and shape strongly depend on the scan speed. Shin et al. [112] examined the stress response during Pb_{UPD}/Au(111) in perchloric acid and observed a scan rate dependence for the individual voltammetric waves and the stress response. They have attributed it to kinetically controlled surface alloying [$(\sqrt{3}\times\sqrt{3})$ R30°], which occurs at low coverage. A hexagonal close-packed, hcp, Pb ML has been formed at a high coverage while the surface alloy is removed. A particular change in the shape of the CV as a function of the scan rate happens with respect to the shape of the C3/A3 peak pair. In Figure 7-4, the CVs recorded with different scan rates are presented.

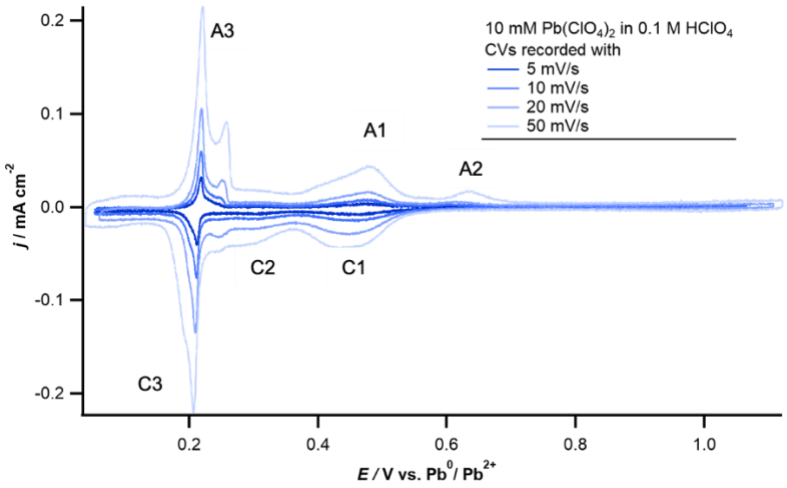

Figure 7-4 Cyclic voltammograms of Au(111) in 10 mM $Pb(ClO_4)_2$ / 1 M $HClO_4$ recorded with scan rates of: 5, 10, 20 and 50 mV/s.

From Figure *7-4*, it is evident that the shapes of the peak pairs C3/A3 and C2/A2 change with the scan rate. At slower scan rates, the peak C2 is not present and the peak A3 is a single peak. Shin et al. [112] found out that at slow sweep rates, most of the Pb atoms were already transformed into the alloy structure before they were oxidized back into the solution, indicating that the decrease of the cathodic peak, C2, is related to the small area of alloy-free Au(111) that exists between the alloyed areas and is available for hcp Pb deposition. The peak A3 splits with increasing the scan rate, indicating a kinetically controlled Pb stripping on the (111)-oriented features [81]. Figure *7-5* shows that the (111)-textured Au surface is roughened which can be observed by the sharpness of the peaks, A3, C2 and C3 [81], as a consequence of surface alloying and dealloying processes.

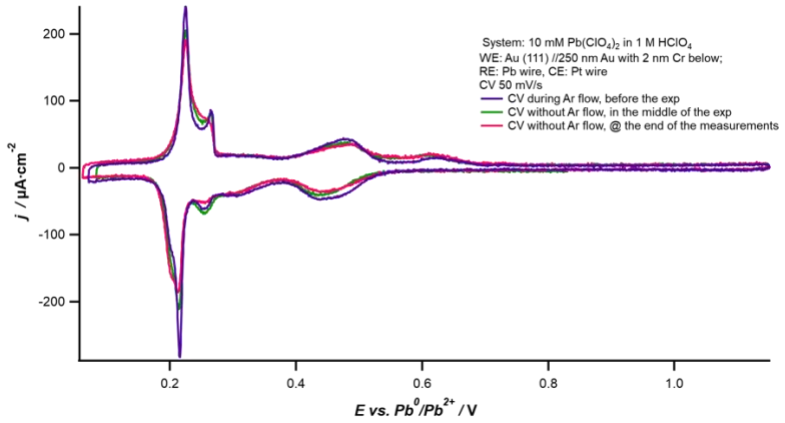

Figure 7-5 Cyclic voltammograms of Au(111) in 10 mM $Pb(ClO_4)_2$ / 1 $HClO_4$ (with scan rate of 50 mV/s) recorded before (lilac line), during (green line) and after (red line) the microcalorimetric experiments.

In the following chapter the results obtained from the microcalorimetric measurements are presented.

7.2.2 Microcalorimetric experiments

For the scope of this work, microcalorimetric pulse experiments were carried out for the Pb_{OPD} and Pb_{UPD} on Au(111) surface from aqueous solutions in acidic media. Three types of pulse experiments were performed:

- Current pulses
- Potential pulses
- Continuous current pulses

7.2.2a Current pulses

The current pulse experiments were performed because the aim of investigating the Pb OPD is to determine the Peltier heat for the bulk deposition of Pb on Au(111).

Before applying the current pulses, around 300 ML of Pb were deposited on the top of the Pb monolayer on Au(111) at –0.08 V, afterwards the cell was turned off, and, as expected, the system reached the OCP of zero V (vs Pb^o/Pb^{2+}). Starting from the OCP, 10 ms long current pulses were applied with different amplitudes (±50–400 µA). After each current pulse, the system was switched back to the OCP (0 V vs Pb^o/Pb^{2+}).

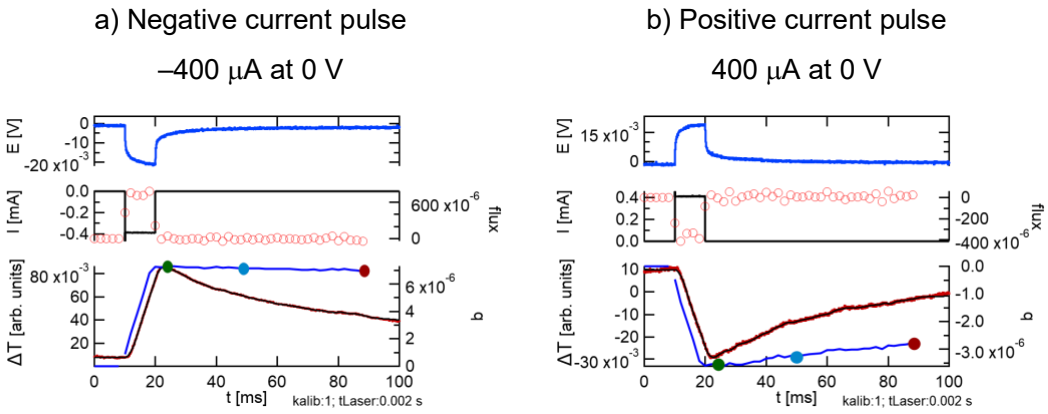

Figure 7-6 Potential, current, and temperature transients, as well as the laser adjustment (black line in the third panel), the accumulated heat (ink-blue line in the third panel) and the heat flux (red dots in the second panel) of two 10 ms long current pulses for the system 10 mM $Pb(ClO_4)_2$ / 1 M $HClO_4$ OPD on Au(111), with current amplitude of ±400 µA. The initial potential from which the pulses started is 0 V.

Exemplary pulses are presented in Figure 7-8. The potential (the ink-blue line in the upmost panel) and the current (the black line in the second row from each panel) transients represented show the typical "box-shaped" transient for metal bulk deposition, meaning that during the pulse, they stay at the same height and relax towards the initial potential after the pulse.

The temperature and heat transient (the ink-blue line at the third row from each panel) increases/ decreases linearly at the start of the pulse at t = 10 ms and reaches its maximum/minimum value at the end of the pulse. After that, the heat transient stays constant for the negative pulse. For the positive pulse the heat transient insignificantly increases. The steadiness of the heat transient indicates that no other process, such as a chemical reaction, is present. From the temperature and heat transients can be extracted that the electrode cools down for positive and heats up for the negative pulses.

As shown in Figure 7-7, for an exemplary measurement series, the obtained values of the molar heat were plotted vs the respective overpotential to determine the reversibly exchanged heat during the lead overpotential deposition for one set with three different integration times (25, 50 and 90 ms) for the heat. For the measurement series shown in Figure 7-7, the values for the reversibly exchanged heat are –4.6, –4.4 and –4.1 ± 2 kJ $mol^{-1}$of electron, respectively. Thus, the value of the reversible heat does not depend much on the time for which the temperature transient was fitted.

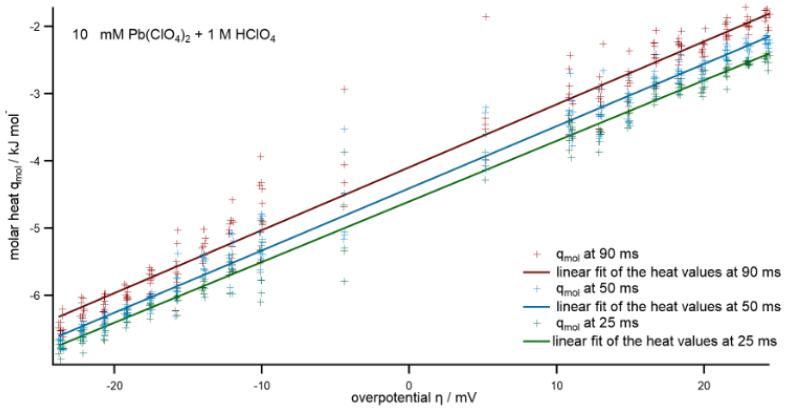

Figure 7-7 Linear fit of the molar heat of current pulses measurement in 10 mM $Pb(ClO_4)_2$ / 1 M $HClO_4$ on Au(111). Starting from an initial potential of 0 V (vs Pb^o/Pb^{2+}), current pulses are applied with amplitudes: ±50–400 μA. The Peltier heat is determined by interpolating the molar heat to 0 V (to an equilibrium) and in this example is –4.4 ± 2 kJ $mol^{-1}$of electron. This Peltier heat refers to the anodic process, the dissolution. The system is cooling by applying positive pulses and heating by applying negative pulses.

7.2.2b Potential pulses

Potential pulses were applied for the whole potential window for the system Pb UPD and dissolution on Au(111) in acidic media. Starting from a set initial potential, 10 ms long potential pulses were carried out. A series of alternating negative and positive potential amplitudes were applied. The amplitudes of the potential were ranging from ±0.03 V to ±0.20 V. After the end of each pulse at t = 20 s, the cell was switched back to the inititial potential.

An examplary negative and positive potential pulse are presented in Figure 7-8. The duration of the pulse is 10 ms with an amplitude of ±0.12 V, starting from an initial potential of 0.45 V (at peak C1/A1). The pulses correspond to 10 mM $Pb(ClO_4)_2$/ 1 M $HClO_4$ on Au(111).

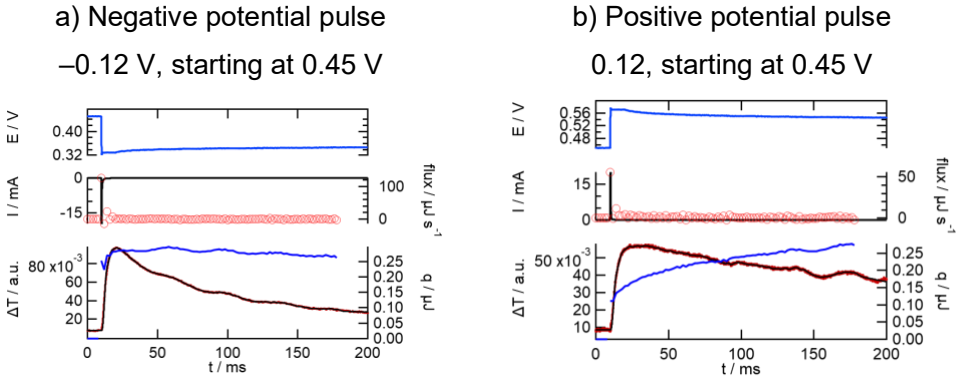

Figure 7-8 Potential, current, and temperature transients, as well as the laser adjustment (black line in the third panel), the accumulated heat (ink-blue line in the third panel) and the heat flow (red dots in the second panel) of two 10 ms long potential pulses for the system 10 mM $Pb(ClO_4)_2$ / 1 M $HClO_4$ on Au(111), with an amplitude of ±0.12 V. The initial potential from which the pulses started is 0.45 V (C1/A1).

Figure 7-8, shows that in the potential (the ink-blue line in the upmost panel) transient, the potential jump at t = 10 ms is followed by a slight relaxation in the direction of the initial potential after the pulse. The current (the black line in the second row from each panel) transients show a sharp peak at the beginning of the pulse (DL charging) and a small current during the pulse. At t = 20 ms, the current drops to zero since the cell was switched to OCP.

Qualitatively, the temperature changes and the heat resulting from the negative pulses correspond to the heating up of the electrode during lead deposition.

For the dissolution of lead, the temperature transient and the heat exhibit no standard behaviour. The heat transient should reach a constant value immediately after the pulse. However, in the exemplary pulse in Figure 7-8 b), the heat continues to rise. A possible reason for the latter can be that the dealloying process is slow or accompanied by another process.

As shown in Figure 7-9 for an exemplary measurement series, the obtained values of the molar heat q_{mol} were plotted against the respective overpotential to determine the reversibly exchanged heat. The Peltier heat from the potential pulses is determined following the procedure described in section 3.2.3. In order to derive the reversible contribution to the molar heat, the molar heat values obtained for the different pulse amplitudes are interpolated to zero overpotential. Figure 7-9 presents

the plot of the molar heat vs the applied overpotential for the potential pulses done at an initial potential of 0.45 V.

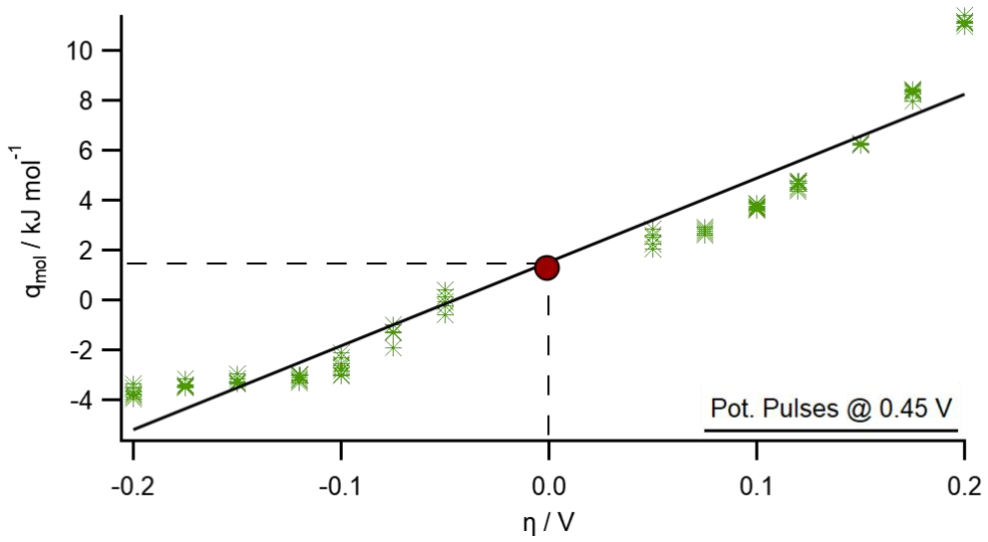

Figure 7-9 Linear adjustment of the molar heat of potential pulse measurement in 10 mM $Pb(ClO_4)_2$ / 1 M $HClO_4$ on Au(111). Starting from an initial potential of 0.45 V (vs Pb^o/Pb^{2+}), 50 sets of potential pulses are applied with amplitudes: ± 0.03, 0.05,0.075, 0.10, 0.12, 0,15, 0.18 and 0.2 V. The molar heat is determined by interpolating the molar heat (@ t = 180 s) to 0 V (to an equilibrium) and in this example is 1.5 ± 2 kJ mol^{-1}. This Peltier heat refers to the anodic process, the dissolution. The system is cooling by applying positive pulses and heating by applying negative pulses.

From Figure 7-9, the obtained positive Peltier heat refers to the anodic processes, meaning that the system is heating for the positive pulses. At this potential occurs the dealloying of Pb from the Au(111) surface at the anodic side which as an irreversible process with its counterpart at 0.25 V. Therefore, the history of the initial potential is very important, meaning whether previously the system was scanned from cathodic or from the anodic direction.

7.2.2c Continuous current pulses

A series of continuous current pulses were applied, scanning the Pb deposition region from 1.01 V to 0.05 V and the dissolution region from 0.05 V to 1.01 V. This procedure allows consecutive change to the state of the surface and the corresponding potential. The pulse duration was 10 ms, and the current amplitude was constant. For different sets of pulses, the current amplitude varied from ±200 to ±400 µA, with increments of

±35 µA. These current amplitudes change the surface coverage by only a few % of a monolayer, ML, per pulse. Because of the system's irreversibility (and the potentials at which the peaks and their counterparts appear in Figure 7-10), different sets of continuous current pulses were applied, varying the negative potential limit, i.e., the inflection point, for each series. Initially, the negative current amplitude pulses were applied until the respective deflection point, at which the current amplitude was then switched to positive (c.f. Figure 7-10).

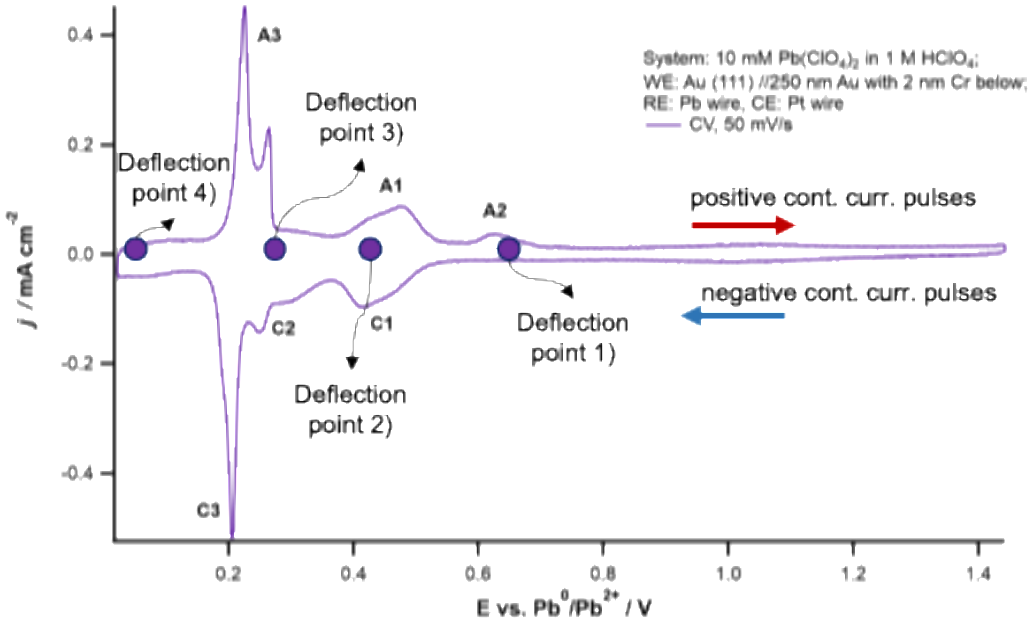

Figure 7-10 Cyclic voltammogram of Au(111) in 10 mM $Pb(ClO_4)_2$ / 1 M $HClO_4$ during Pb_{UPD} on (111)-textured Au film. CV is scanned with 50 mV/s. In the cathodic direction, continuous pulses with negative current amplitude were applied and in the anodic with positive one. The deflection points refer to the potential limits where the polarity of the amplitude was switched from negative to positive.

Example of the different sets depending on the deflection point are:

1) the DL region, between 1.01 V and 0.63 V, i.e., before the Pb UPD
2) between 1.01 V and 0.42 V, i.e., including peaks C1/A1
3) between 1.01 V and 0.23 V, i.e., including peaks C1/A1 and C2/A2
4) between 1.01 V and 0.05 V, i.e., including the whole potential region, as shown in Figure 7-10

In Table 7-1 exemplary potential, current and temperature transients of positive and negative continuous current pulses from each series are represented. The length of the current pulse is 10 ms, and the represented current amplitude is ±230 µA. The

Pb UPD is driven by the cathodic (negative) pulses and the dissolution by the anodic (positive) pulses. Additionally, the graphs in Table *7-1* include the result of the calibration and the laser adjustment, i.e., the fitting procedure.

Upon a purely qualitative examination of the results, the current transients (the black line in the upmost panel) in all graphs remain constant during the pulse and return directly to their initial values after the pulse ends. The potential transients (the ink-blue line in the upmost panel) reach min or max at the end of the pulse and afterwards slowly relax. That suggests neither a concentration gradient nor transport limitation arises in this system. Regarding the temperature (red line in the third panel) and the heat resulting during the negative pulse, it is observed that the electrode heats up, i.e., during lead deposition, and during the positive amplitude, where lead dissolution occurs, it cools down. As already described in section 3.2.3.1, the heat decreases (or increases) quickly during the pulse. However, upon closer examination of the heat transients from the representative pulses from the peaks C2 (surface along) and A3 (c.f. Table *7-1*, the third set), it is noticeable that after the pulse ends ($t > 20$ ms), the heat value is not constant but decreases or increases until $t = 200$ ms. In a fast and unhindered reaction, such a behaviour should not occur. Instead, the heat transient should reach a constant value immediately after the pulse ends. A possible cause that could influence heat development is either a parallel process in that region, the alloying itself, or simply a drift.

Table 7-1 Exemplary current pulses for the system 10 mM $Pb(ClO_4)_2$ / 1 M $HClO_4$ on Au(111). Potential, current, and temperature transients, as well as the laser adjustment (black line in the third panel), the accumulated heat (ink-blue line in the third panel) and the heat flow (red dots in the second panel) of several 10 ms long current pulses, with current amplitude of ±230 μA. The fitting procedure is done with 85 laser pulses, until t = 180 ms. The Pb UPD is driven by the cathodic (negative) pulses and the dissolution of Pb by the anodic (positive) pulses.

Sets depending on the deflection point	Negative current pulse with amplitude –230 μA, fitted with 85 mp	Positive current pulse with amplitude 230 μA, fitted with 85 mp
1) 1.02-1.20 V	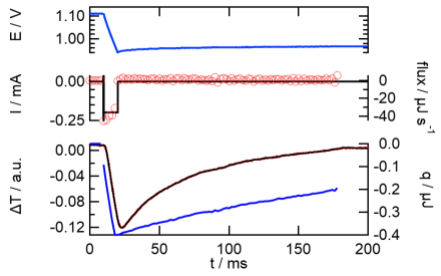	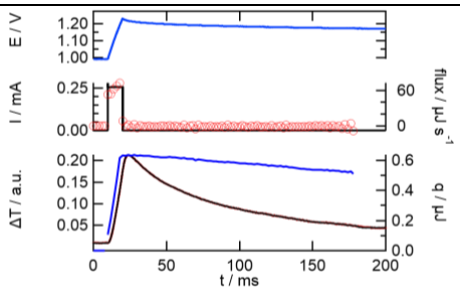
2) 0.52 – 0.66 V	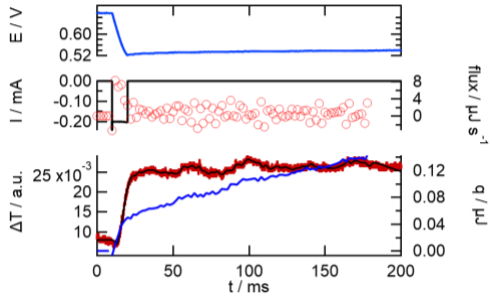	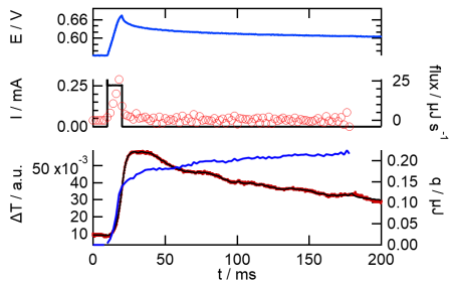
3) 0.34 – 0.27 V	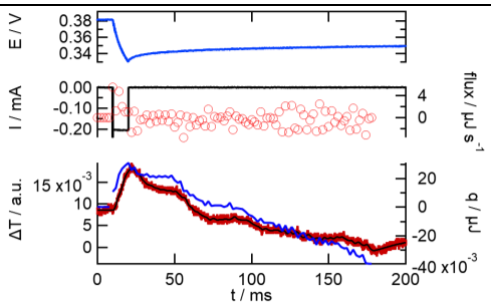	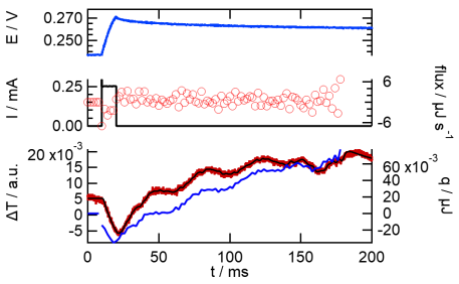
4) 0.20 – 0.22 V	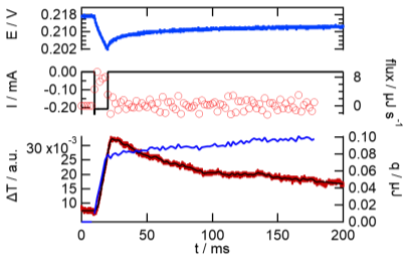	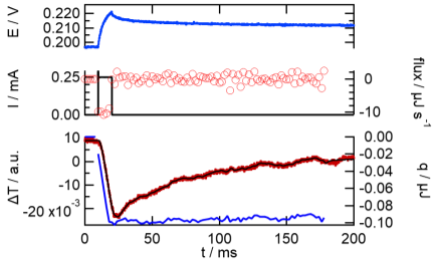

The obtained values of the molar heat q_{mol} for the exemplary measurement series, were plotted against the applied potential, and are shown in Figure *7-11*.

7.3 Molar Peltier Heats of Pb OPD and Pb UPD in Perchloric Acid

Figure 7-11 summarizes the results obtained from the microcalorimetric measurements of Pb_{OPD} and Pb_{UPD} on Au(111) from aqueous solutions in acidic (pH = 0) media, where the molar heats are plotted against the applied electrode potential.

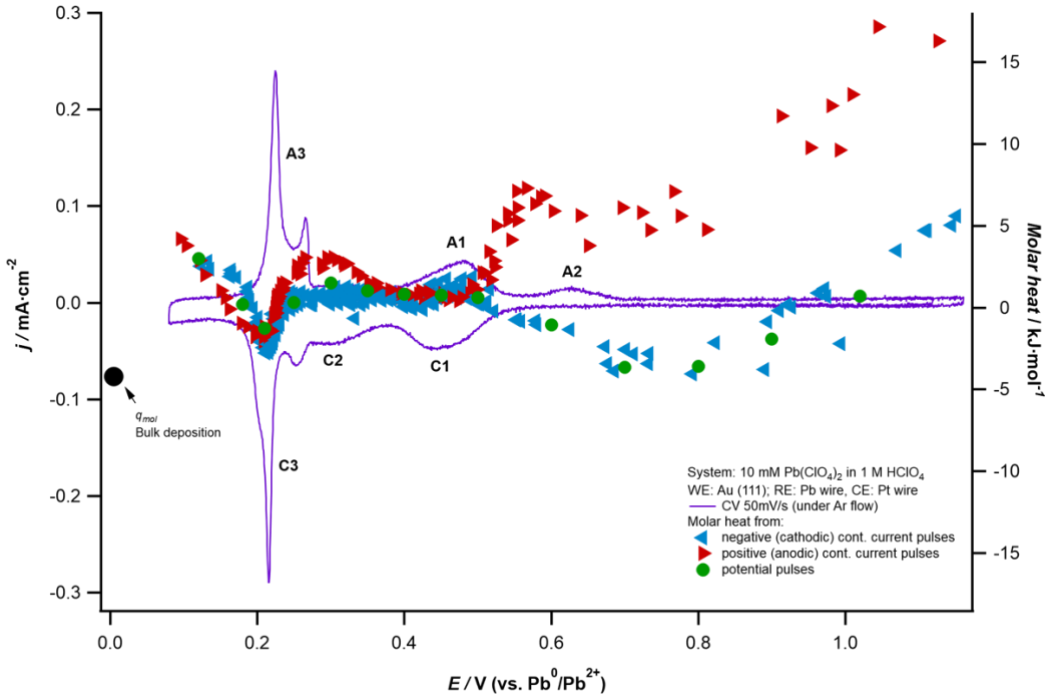

Figure 7-11 Plot of the cyclic voltammogram of Au(111) in 10 mM $Pb(ClO_4)_2$ / 1 M $HClO_4$ (with scan rate of 50 mV/s) and the Peltier heat (@ t = 180 s) from all different experimental procedures versus the electrode potential (vs Pb^0/Pb^{2+}). The red triangles represent the heat from the anodic current pulses, the blue triangles are representing the heat from the cathodic current pulses, and the green dots are from the Peltier heat from the potential pulse measurements.

In Figure 7-11, the black circle at 0 V represents the molar heat obtained by the current pulse measurements of the Pb_{OPD} and it is in order of -4.4 ± 2 kJ mol^{-1} of electron for the Pb dissolution. The reversibly exchanged heat from the well-defined potential pulses is presented with green circles in Figure 7-11. The peak-pairs in the UPD A3/C3 and A1/C1 are reversible. The value of the molar heat for A3/C3 is about the same as the measured molar reversible heat from the OPD, where the measured reversible heat from the A1/C1 is slightly larger than the OPD. The molar reversible heat at ca. 0.3 V (at peak C2) is about 0.

The red and blue triangles mark the molar heat values obtained by continuously charging the surface with small current pulses. The data sets marked with blue left-handed triangles were obtained by negative current pulses, starting at potentials positive of the Pb UPD. By the pulse sequence, the potential shifted negatively. The data points marked by red right-handed triangles were started at potentials positive of the Pb OPD with positive current pulses, causing positive potential shifts. The data points present the potential before the application of the current pulse. The data points become denser in areas with strong electrochemical conversion.

The red and blue data points achieved about the same molar heat at the deposition potential window (from 0.5 to 0.1 V). The slight deviation at C2, at 0.25 V, represents the slight irreversibility of the alloy formation. The deviations are the strongest for potentials larger than 0.5 V (around peak A2). Closer examination for this deflection is done by performing microcalorimetric continuous current pulse experiments as described in the subchapter 7.2.2c. Figure *7-12* presents exemplary data from four sets of continuous current pulses with different negative potential limits (deflection points). Note that the deflection point here are closer (regarding the negative potential limit) to each other and are different from the ones in Figure *7-10* because it was of interest at which electrode potential the deviation of the positive pulses occurs. From Figure *7-12*, it is seen that the deviations around A3 occur only when the polarity of the pulse series (from negative to positive current) deflects at potentials $\leq$0.5 V. This leads to a conclusion that the strong deviations are present only where the electrochemical conversion is small (around peak A2), which reflects the irreversibility of the (de-)alloying process and/or a slow desolvation.

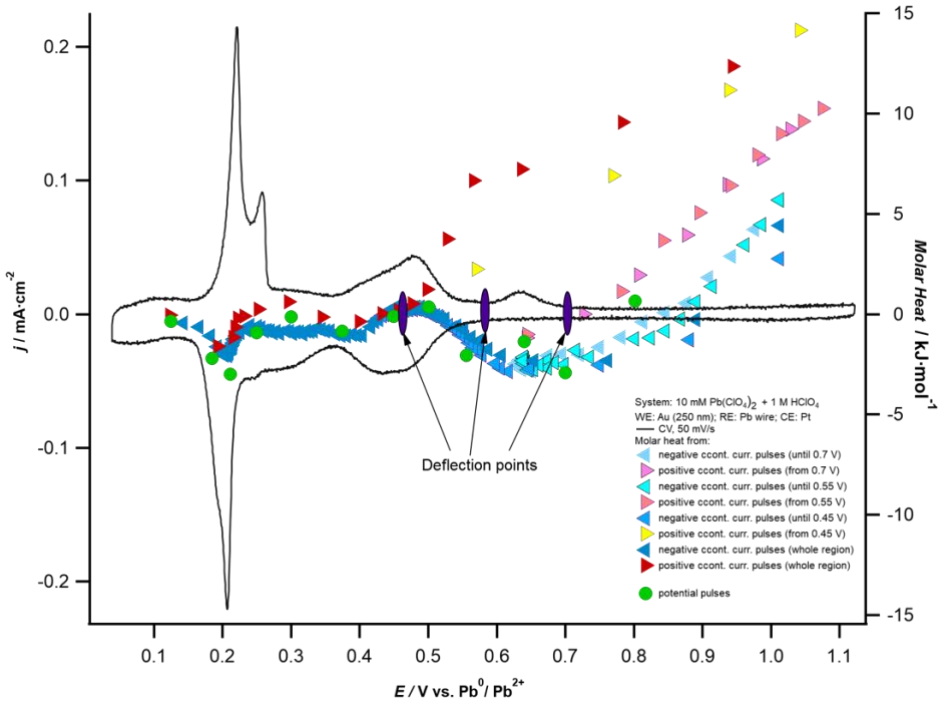

Figure 7-12 Plot of the cyclic voltammogram of Au(111) in 10 mM $Pb(ClO_4)_2$ / 1 M $HClO_4$ (with scan rate of 50 mV/s) and the Peltier heat from continuous current pulses versus the electrode potential (vs Pb^0/Pb^{2+}). The experiment pulses started from fixed cathodic potential, around 1.1 V, up until 0.70, 0.55, 0.45, and 0.12 V as anodic potential limit.

The deviations of the molar heat from the positive current pulses at potentials ≥0.8 V (DL region) might not be real because the currents are very small.

Figure *7-11* shows that the molar reversible heats measured by potential pulses, nicely corroborate the molar heats obtained by the negative continuous current pulse sequences.

Since the molar Peltier heat of the Pb bulk deposition operates as a reference for the discussion of the Pb UPD values, this data will be first discussed.

7.4 Molar Peltier Heat and Reaction Entropy for Pb Overpotential Deposition

The experimental molar reversible heat for Pb dissolution from the overpotential deposition, is negative in perchloric acid, –4.4 kJ mol^{-1} of an electron, which means that the system's entropy decreases with the anodic reaction, which is the dissolution of Pb.

$$Pb^0(s) \longrightarrow Pb^{2+}(aq) + 2\ e^-$$

The molar Peltier heat, Π, as introduced in the "Theoretical background" chapter, is given by the molar reaction entropy of the half-cell reaction, $\Delta_R S$, written as a reduction reaction, the temperature T, and the contribution from ion transport in solution, i.e., the entropy of transfer (c.f. equation (5) and equation (9)) and entropy of the electrons. The contribution of the electrons to the molar Pelter heat is very small for the overpotential deposition, as reported by Ozeki [20] and is neglected for the further calculations.

First, the Hittorf transference numbers are estimated from the contributions of the individual ions to the total ionic conductivity to calculate the transport contributions to the molar Peltier heat. It is important to note that the molar conductivities at infinite dilution from [18, 53] are employed, and it is assumed that the perchloric acid completely dissociates. Table 7.2 depicts the Eastman entropies of transfer, the molar limiting conductivities and the Hittorf transfer number of the predominant ions. The contribution of the Pb^{2+}ion is neglected because the t(Pb^{2+}) is very small (<1%).

Table 7-2 Eastman entropies of transfer, molar limiting conductivities and Hittorf transfer numbers of the respective ions.

ion	$\hat{s}_i$ / J $mol^{-1}K^{-1}$ [18]	λ_0 / S cm^2 mol^{-1} [53]	t
ClO_4^-	–3.1	67	0.16
H^+	43	350	0.84

As can be seen from the values reported in Table 7.2, the contribution to the molar Peltier heat from transport is mainly dominated by the proton transport and much less than the perchloric anion. This contribution is equal for the over- and underpotential deposition of Pb.

The calculated entropy of transfer, $\Delta_T S$, is $\Delta_T S = 35.6\ J\ mol^{-1}K^{-1}$ of an electron, which corresponds to 10.6 kJ mol^{-1}. Hence, the reaction entropy, $\Delta_R S$, of Pb dissolution from the overpotential deposition in 10 mM $Pb(ClO_4)_2$/1 M $HClO_4$ is $\Delta_R S_{exp,Pb,diss} = -50\ J\ mol^{-1}K^{-1}$ of an electron.

Further quantitative comparison of the experimental values with those from the literature is made in the following subchapter.

7.4.1 Quantitative comparison of the experimental reaction entropy with the literature

The net surface composition for the Pb overpotential deposition does not change with further depositing Pb, and the reaction entropy can be calculated from the entropy of metallic Pb, that of the electrons, and the absolute entropy of Pb^{2+} in solution. To quantitatively compare the experimental value, the calculations on the reaction entropy from the literature are done for the opposite process, the lead dissolution. Therefore, the theoretical entropy calculations start from lead in a solid standard state to a solvated Pb^{2+} ion in an aqueous state.

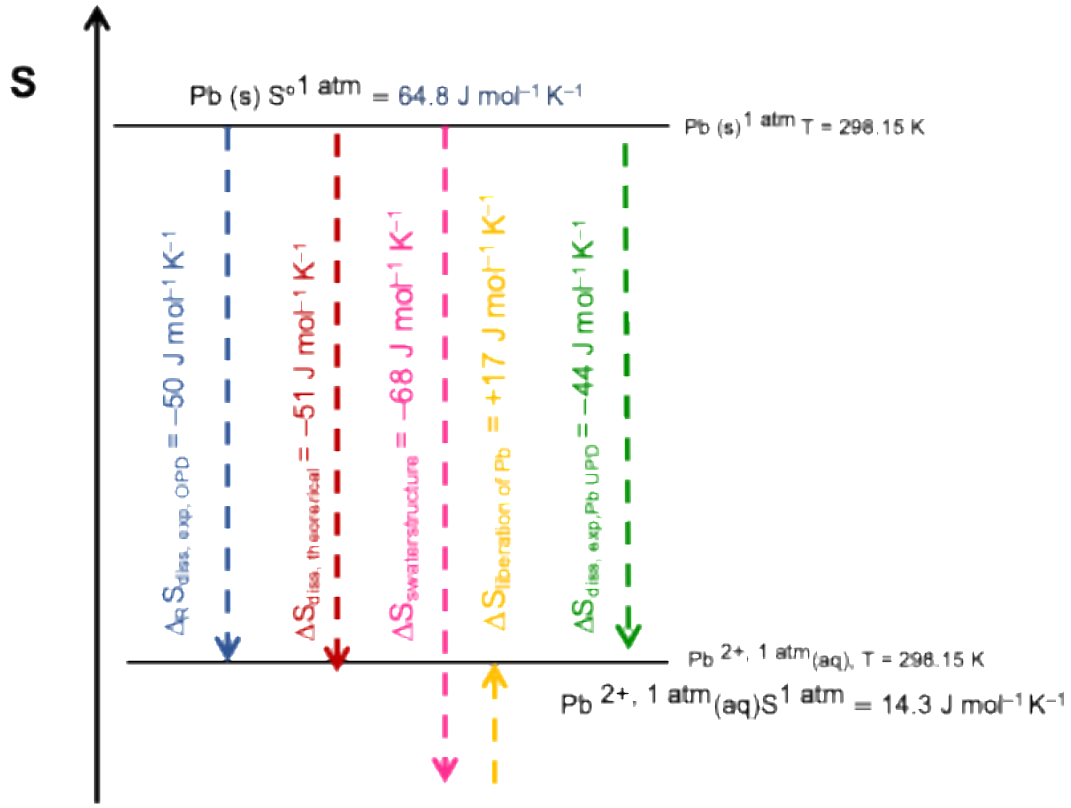

Figure 7-13 Entropic diagram for 10 mM $Pb(ClO_4)_2$/ 1 M $HClO_4$ on Au(111). The most left vertical arrow represents the entropy. The dissolution starts from the standard entropy of solid state (the middle vertical black line), $S^{o\,(298.15\,K)} = 64.8$ J mol^{-1} K^{-1}. The absolute partial entropy of the Pb^{2+} ion in aqueous solution, corrected for a concentration of 10 mM Pb^{2+} is 14.3 J mol^{-1} K^{-1}. This leads to theoretical value for the reaction entropy of the dissolution, $\Delta S_{diss,\,theoretical} = –50.5$ J $mol^{-1}K^{-1}$. The lead ion is a structure making ion, and the corresponding entropy is $\Delta S^{o}_{Pb}(str) = –68$ J mol^{-1} K^{-1}. The entropy for setting free the lead ion from the solid (pink arrow) is +16.8 J mol^{-1} K^{-1}($\Delta S^{o}_{Pb}(str) + \Delta S_{diss,\,theoretical}$).

Figure 7.13 represents the entropy diagram for the lead dissolution process. The standard entropy of solid Pb is taken from the literature [53], and its value is $S^{o}_{(298.15\ K)} = 64.8\ J\ mol^{-1}\ K^{-1}$. This state is represented by the vertical black line in the middle of Figure 7.13. The state where the Pb^{2+} ion is solvated is represented by the vertical, most down black line in Figure 7.13. The entropy value for the solvated Pb^{2+} ion is calculated by considering the absolute partial entropy of the Pb^{2+} ion in aqueous solution is $-33.9\ J\ mol^{-1}\ K^{-1}$ taken from Marcus [31].This value should be corrected for the concentration used, which can be done by using the activity of the ion in the solution concentration of interest. When the pH is strongly acidic, the activity of 10 mM Pb^{2+} is $3{\cdot}10^{-3}$. That is calculated using the program *PhreeqC Interactive 3.2.2.* When correcting the partial molar entropy of the ion, the following equation is used:

$$\bar{S}_{abs} - R\ln a_{Pb2+} = (-33.9 + 48.2)\ J\ mol^{-1}\ K^{-1} = +14.3\ J\ mol^{-1}\ K^{-1}$$

From here, the approximated theoretical value for the dissolution process, $Pb^{0}(s) \longrightarrow Pb^{2+}(aq) + 2\ e^{-}$, is calculated by extracting the partial molar entropy of the ion from the standard solid state:

$$\Delta_R S_{diss,theoretical} = S^{o}_{(298.15\ K)} - \bar{S}_{abs,\ corr} = -50.5\ J\ mol^{-1}\ K^{-1}$$

That implies that the dissolution process leads to entropy reduction, a result aligned with the experimental value obtained from the microcalorimetric measurements in this work.

The magnitude of the calculated reaction entropy $\Delta_R S_{diss,theoretical}$ is same as the experimentally determined one, $\Delta_R S_{exp,Pb,diss} = -50\ J\ mol^{-1}K^{-1}$ of an electron, and can be understood by examining the processes by which it is composed.

It is considered that in order the Pb to be dissolved from solid state to aqueous, two processes are involved; first, setting free of the Pb from the solid, i.e., liberation of Pb, and second, the solvation of the Pb, i.e., the entropy of the water structure calculated by Marcus [31], which for the lead is $\Delta S^{0}_{Pb^{2+}}(str) = -68\ J\ mol^{-1}\ K^{-1}$. The only unknown is the entropy of liberation of Pb.

$$\Delta S_{liberation} = -(\Delta S^{o}_{Pb}(str) - \Delta S_{diss,theoretical}) =$$

$$= -(-68 + 50.5)\ J\ mol^{-1}\ K^{-1} = 17.5\ J\ mol^{-1}\ K^{-1}$$

The minus sign before the substruction is taken because the setting free of the Pb from solid is occurring at the opposite direction. The liberation entropy change of Pb is +17.5 J mol^{-1} K^{-1}. This entropy change refers when Pb from solid state, Pb(s), goes to Pb in solution without hydration, Pb (mobile). Thus, the positive sign is as expected, considering that the ion in the mobile state has higher degrees of freedom.

From the calculated values for the entropy change during Pb dissolution, it can be deducted that the solvation of lead is the dominant process.

7.5 Molar Peltier Heat and Reaction Entropy of Pb UPD

From Figure 7-11, can be directly inferred that the molar Peltier heat in the UPD region (between 0.18 V and 0.23 V, A3/C3), –2.1 ± 2 kJ mol^{-1} of an electron, is comparable to that of Pb overpotential deposition, –4.4 ± 2 kJ mol^{-1} of an electron. The deviation of 2 kJ mol^{-1} is within the experimental error. That indicates that the Pb deposition is not accompanied by side processes. In addition, from the microcalorimetric investigation of Ag_{UPD} on Au(111), in the absence of coadsorption of anions, the Peltier heat of Ag overpotential deposition and Ag UPD processes are equal within the experimental errors [113] as in this case. The same is encountered for the Cu_{OPD} and Cu_{UPD} [22].

The measured reaction entropy change is in order of –44 J mol^{-1} K^{-1}(of electron), insignificantly lower than the one for the dissolution from Pb in the overpotential region, –50 J mol^{-1} K^{-1}(of electron) since it is within the experimental error. That demonstrates that, as in the case of OPD, the reaction entropy change is dominated by the solvation of the lead ions (c.f. Figure 7.13). As derived from the previous conclusions [113], perchlorate has no influence during this process in the potential region.

From Figure 7-11, can be observed that the molar Peltier heat in the deposition/dissolution region (C1/A1) is in order of 2.0 ± 2 kJ mol^{-1} of an electron. That is slightly higher than the Peltier heat of Pb overpotential deposition, –4.4 ± 2 kJ mol^{-1} of an electron. The slight deviation can be an indication that beside the dissolution another process takes place, such as the alloy formation.

7.5.1 Enthalpy change between Pb_{UPD} and Pb_{OPD}

Conclusions about the change in the reaction enthalpy can be drawn from the measured entropy changes in combination with the equilibrium potentials of the Pb_{UPD}/Au(111), in this case in 0.21 V. The change of the potential leads to a change of the Gibbs free energy changes, $\Delta\Delta_R G$. And the change in the reaction entropy is same for the Pb over- and under- potential deposition, and very small, as deduced from the calculated values in the previous chapter.

Further information on what drives the dissolution of lead at the UPD region on Au(111), it is calculated the reaction enthalpy, $\Delta_R H$, by using the equation (22):

$$\Delta\Delta_R H = \Delta E_{eq} z F + T\Delta\Delta_R S \qquad (21)$$

Where the E_{eq} is the equilibrium potential (in this case in 0.21 V), z is the charge, F is the Faraday constant, T the temperature in K and $\Delta\Delta_R S$ the change between the OPD and UPD process for the reaction entropy. By substituting the numbers into the equation (22), a change in the reaction enthalpy of $\Delta\Delta_R H$ = 21 kJ mol^{-1} is calculated. The change in the reaction enthalpy refers to the enthalpy change between the Pb_{UPD} and Pb_{OPD}. From the calculation it is concluded that the deposition process is enthalpy driven and that the interaction between of Pb-Au is by about –21 kJ mol^{-1} stronger than Pb-Pb.

7.6 Conclusions

Electrochemical microcalorimetry has been used to assess the Peltier heat and the reaction entropy of lead over- and underpotential deposition on (111)-textured Au-films from aqueous solutions in acidic media.

The deposition is driven by the negative pulses and the dissolution by positive. From the microcalorimetric experiments several conclusions were made:

i. The molar Peltier heat of the Pb bulk deposition operates as a reference for the discussion of the Pb UPD values. The molar reversible heat for the bulk deposition reaction of lead on Au(111) is in order of 4.4 ± 2 kJ mol^{-1}. The contribution of the entropy of transfer towards this molar heat is $\Delta_T S$ = 35.6 J $mol^{-1}K^{-1}$ per electron. Consequently, the reaction entropy for bulk lead deposition was determined and it is $\Delta_R S_{exp,Pb,dep}$ = +50 J $mol^{-1}K^{-1}$ of an electron. This value was quantitatively compared the one estimated from the literature, $\Delta_R S_{dep,theoretical}$ = 50.5 J mol^{-1} K^{-1}, and was concluded that the dominant contribution towards the entropy change is the desolvation of lead.

ii. In the lead UPD region a molar heat of 2.1 ± 2 kJ mol^{-1} was measured for the underpotential deposition, whose difference from the lead OPD is within the experimental error bars. Hence, the reaction entropy is of the same order as the reaction entropy of overpotential deposition. Further calculation on the enthalpy changes between the change in the reaction enthalpy for the OPD and UPD was done, and it was concluded that the interaction between Pb-Au is much stronger than Pb-Pb interactions.

iii. There is a smaller and larger discrepancy between the molar heat from the positive and negative continuous pulses at two regions. The smaller one showed up around 0.3 V, and it originates from the slight irreversibility of the alloy formation. The larger deviations were observed around A3 and this deviation occurs only when the polarity of the pulse series (from negative to positive current) deflects at potentials ≤0.5 V. This leads to a conclusion that the strong deviations are present only where the electrochemical conversion is small (around peak A2), which reflects the irreversibility of the (de-)alloying process and a slow desolvation.

Chapter 8 Summary

The present work focuses on determining entropic effects during electrochemically driven adsorption processes at Au(111) electrodes using electrochemical microcalorimetric measurements.

Electrochemical microcalorimetry allows the measurement of small temperature changes at the working electrode, thereby enabling a determination of the heat generation and the entropy change during interfacial reactions.

Two types of electrochemically induced adsorption processes were studied: the adsorption of organic molecules and the over- and underpotential deposition of Pb, both on Au(111).

Firstly, the pyridine adsorption from aqueous solutions on Au(111) was examined because pyridine is a prototypical molecule identified as a cocatalyst for CO_2 reduction. From the microcalorimetric measurements, it was found that the process of pyridine adsorption has a reaction entropy about $\Delta_R S \approx -98 \pm 20$ J mol_{py}^{-1} K^{-1}. In order to disentangle the entropic contributions involved in the process, two cases were built: a thermodynamic cycle and a simpler model. Both models fit very well, and it was concluded that the main entropic contribution to the negative adsorption entropy comes from the fixation of the pyridine molecules on the surface. Regarding the desolvation of the pyridine upon adsorption, and its influence on the water molecules, the results suggest that pyridine preserves its solvation shell upon adsorption. Other factors that minorly contribute are the lifting of the pyridine molecules from the surface.

Given that in this thesis, the application of electrochemical microcalorimetry was well established for the pyridine adsorption on Au(111), the method was transferred to a slightly larger organic molecule – thymine. From the microcalorimetric measurements, the reaction entropy for the adsorption of thymine is –60 J mol_{Thy}^{-1} K^{-1}. Here, as for pyridine, a simple model was built, which approximated that the thymine molecules behave as solid when adsorbed on Au(111). The rough model fits well with the experimentally determined reaction entropy. That leads to the conclusion that also for thymine molecules the fixation from aqueous solution dominates the entropy change of the process.

A general conclusion is therefore made that the main entropic contribution to the adsorption of slightly polar organic molecules on Au(111) originates form the fixation of the molecules on the surface.

The results for the over- and underpotential deposition of Pb derived from the microcalorimetric measurements indicate that the reaction entropy of Pb bulk is $\Delta_R S_{exp,Pb,dep}$ = 50 J $mol^{-1}K^{-1}$ referenced to moles of electron. The further quantitative comparison of the experimental values with those from the literature corroborates the examined value, and it was determined that the desolvation of the Pb is the dominant contribution to the reaction entropy, which even overcompensated the entropy change by fixation of the Pb. In the underpotential lead deposition region, the molar Peltier heat, and hence the reaction entropy, is the same as that of the bulk deposition. That points out that no considerable side process occurs. This finding is aligned with the previously reported data for Ag OPD and UPD, as well as Cu OPD and UPD on Au(111) in the absence of coadsorption of anions.

References

[1] J. M. Hermann, H. Mueller, L. Daccache, Ch. Adler, S. Keller, M. Metzler, T. Jacob, L. A. Kibler, *Electrochim. Acta 388*, **2021**, 138547

[2] N. Srinivasan, S. Thirumaran, *Superlattices and Microstructures 51*, **2012**, 912-920

[3] J. Li et al., *J. Am. Chem. Soc. 137,* **2015**, 2400

[4] Sh. Iqbal, S. Wezisla, N. Podgaynyy, H. Baltruschat, *Electrochimica Acta 186,* **2015**, 427–435

[5] B. Roelfs, H. Baumgaertel, *Ber. Bunsen-Ges. Phys. Chem., 99,* **1995**, 677

[6] S. G. Kiron, K. Kundu, *Can. J. Chem. 72*, **1994**, 1120

[7] C. Donner, S. Kirste, L. Pohlmann, H. Baumgärtel, *Langmuir 14*, **1998**, 6999

[8] A. P. M. Camargo, H. Baumgärtel, C. Donner, *PhysChemComm. 5*(22), **2002**, 151–157

[9] D. Pletcher, F. C. Walsh*, Industrial Electrochemistry*, Chapman and Hall, London, **1990**

[10] R. W. Murray, *Molecular Design of Electrode Surfaces*, Wiley, New York, **1992**

[11] Ch. Chen, N. Washburn, A. A. Gewirth, *J. Phys. Chem. 97*, **1993**, 9754–9760

[12] S. Sayed, K. Juettner, *Electrochim. Acta 28*, **1983**, 1635

[13] M. Bouty, Sur un phénomène analogue au phénomène de Peltier. *Journal de Physique Théorique et Appliquée, 8*, **1879**, 341–346

[14] C. Wagner, Über die thermodynamische Behandlung stationärer Zustände in nicht iso-thermen Systemen. *Annalen der Physik 395*, **1929**, 629–687

[15] C. Wagner, Über die thermodynamische Behandlung stationärer Zustände in nicht iso- thermen Systemen II Berichtigung und Ergänzung. *Annalen der Physik 398*, **1930**,370– 390

[16] E. Lange, T. Hesse, *Journal of the American Chemical Society 55*, **1933**, 853–855

[17] E. Lange, J. Monheim, Über elektrolytische Peltier-Wärmen und ihre Messung mittels isotherm-adiabatischer Differentialcalorimetrie. *Zeitschrift für Physikalische Chemie 150A*, **1930**, 177–202

[18] Agar, J. N., Thermogalvanic Cells in Advances in Electrochemistry and Electrochemical Engineering, Delahay, P., Hrsg.; Interscience Publishers: London, **1963**

[19] J. M. Gottfried, R. Schuster, Surface mictrocalorimetry in Surface and Interface Science, Wandelt, K., Hrsg.; Wiley-VCH: Berlin, **2015**

[20] T. Ozeki, N. Ogawa, K. Aikawa, I. Watanabe, S. Ikeda, *Journal of Electroanalytical Chemistry and Interfacial Electrochemistry 145*, **1983**, 53–65

[21] P. Boudeville, *Inorganica Chimica Acta 226*, **1994**, 69–78

[22] R. Schuster, *J. Phys. Chem. C* 120, **2016**, 21522–21535

[23] R. Schuster, R. Rösch, A. E. Timm, *Zeitschrift für Physikalische Chemie 221,* **2007**, 1479–1491

[24] K. R. Bickel, K. D. Etzel, V. Halka, R. Schuster, *Electrochimica Acta 112*, **2013**, 801–812

[25] S. Frittmann, V. Halka, C. Jaramillo, R. Schuster, *Review of Scientific Instruments 86*, **2015**, 43301

[26] S. Frittmann, Der Einfluss der Anionen auf die elektrochemische Silber- und Kupfer- Abscheidung auf Au(111) - Mikrokalorimetrische Untersuchungen zur Identifikation ladungsneutraler Adsorptionsprozesse, Diss., Karlsruhe: Karlsruher Institut für Technologie, **2017**

[27] L. Stolberg, S. Morin, J. Lipkowski, D.E. Irish, *J. Electroanal. Chem. 307*, **1991**, 241-262

[28] H. Wang, D. Wang, *Journal of Electroanalytical Chemistry 392*, **1995**, 13–19

[29] A. L. Rockwood, *Thermochimica Acta 490*, **2009**, 82–84

[30] H. S. Frank, M. J. Evans, *Journal of Chemical Physics 13*,**1945**, 507

[31] Y. Marcus, *Ion solvation*; Wiley: Chichester, **1985**

[32] B. B. Damaskin, O.A. Petru and V.V. Batrakov, Adsorption of Organic Compounds on Electrodes Plenum, New York, **1971**;

[33] B. E. Conway, R. G. Barradas, *Electrochim. Acta 5*, 319, **1961**, 349

[34] B. E. Conway, R. G. Barradas, P. G. Hamilton, J. M. Parry, *J. Electroanal. Chem.10*, **1965**, 485-502

[35] J. Lipkowaki, L. Stolberg, D. F. Yang, B. Pettinger, S. Mirwald, F. Henglein, D. M. Kolb, *Electrochimica Acta, Vol 39, 8/9*, **1994**, 1045–1056

[36] L. Stolberg, J. Lipkowski, D.E. Irish, *J. Electroanal. Chem. 207*, **1986**, 213

[37] L. Stolberg, J. Lipkowski, D.E. Irish, *J. Electroanal. Chem. 238*, **1987**, 333

[38] L. Stolberg, J. Lipkowski, D.E. Irish, *J. Electroanal. Chem. 296*, **1990**, 171

[39] A. Hamelin and G. Valette, *C.R. Acad. Sci. Ser. C 267*, **1986**, 929

[40] A. Hamelin, *J. Electroanal. Chem. 144*, **1983**, 365

[41] W-B. Kai, H. Noda, Y. Hibino, K. Ataka, M. Osawa, *Langmuir 14*, **1998**, 6992–6998

[42] M. Schönig, S. Friedmann, R. Schuster, *ChemPhysChem 23*, **2022**,1

[43] B. Pettinger, M. Danckwerts, K. Krischer, *Faraday Discuss. 121*, **2002**, 153–165

[44] M. Schönig, Mikrokalorimetrische Untersuchungen zur Kinetik und Thermodynamik elektrochemischer Adsorptionsprozesse und der Wasserstoffentwicklung an Gold- und Platinelektroden, Institut für Physikalische Chemie, Dissertation, Karlsruhe: Karlsruher Institut für Technologie, **2021**

[45] A. Hamelin, S. Morin, J. Richer, J. Lipkowski, *J. Electroanal. Chem. 304*, **1991**, 195

[46] A. Hamelin, S. Morin, J. Richer and J. Lipkowski*, J. Electroanal. Chem. 272*, **1989**, 241

[47] A. Hamelin, S. Morin, J. Richer and J. Lipkowski, *J. Electroanal. Chem. 285,* **1990**, 249

[48] B. Pettinger, U. Wenning, H. Wetzel, *Surface Science 101*, **1980**, 409

[49] R. L. Paul, A. J. McQuillan, P. J. Hendra and M. Fleischmann. *J. Electroanal. Chem. 66*, **1975**, 248

[50] J-G. Lee, J. Ahner, J. T. Yates, *J. Chem. Phys. 114*, **2001**, 1414

[51] D.A. Stern, L. Laguren-Davidson, D. G. Frank, J. Y. Gui, C-H. Lin, G. N. Salaita, N. Walton, D. L. Zaoien, A. T. Hybbard*, J. Am. Chem. Soc. 111*, **1989**, 877

[52] B. E. Conway, L.G.M. Gordon, *J. Phys. Chem. 73*, **1969**, 3609

[53] W. M. Haynes, CRC Handbook of Chemistry and Physics, 95th ed.; CRC Press: New York, **2014**

[54] J. P. McCullough, D. R. Douslin, J. F. Messery, I. A. Hossenlopp, T. C. Kincheloe, G. Waddington*, J. Am. Chem. Soc., 17*, **1957**, 4289-4295

[55] D. R. Lide, CRC Handbook of chemistry and physics : a ready-reference book of chemical and physical data, 71. Aufl.; CRC Press: Boston, **1990**

[56] J. Florian, A. Warshel, *J. Phys. Chem. B 103*, **1999**, 10282–10288

[57] S. Cabani, P. Gianni, V. Mollica, L. Lepori, *J. Solution Chem.10*, **1981**, 563

[58] J-F. Li, Y-J. Zhang, A. V. Rudnev, J. R. Anema, S-B. Li, W-J. Hong, P. Rajapandiyan, J. Lipkowski, Th. Wandlowski, Z-Q. Tian, *J. Am. Soc. 137*, **2015**, 2400–2408

[59] J. H. Hermann, Y. Mattausch, A. Weiss, T. Jacob, L. A. Kibler, *J. Electrochem. Soc. 165*, **2018**, J3192

[60] J. Lipkowski, Z. Shi, A. Chen, B. Pettinger, C. Bilger, *Electrochim. Acta 43*, **1998**, 2875–2888

[61] Y. Ikezawa, H. Terashima, *Electrochimica Acta 47*, **2002**, 4407–4412

[62] M. H. Hoelzle, D. M. Kolb, D. Krznarich, B. Chosovich, *Ber. Bunsenges. Phys. Chem. 100*, **1996**, 1779–1790, n 11

[63] B. Roelfs, E. Bunge, C. Schroeter, T. Solomun, H. Meyer, R. J. Nichols, H. Baumgaertel, *J. Phys. Chem. B 101*, **1997**, 754–765

[64] O. Manousek, P. Zuman, *Collect. Czech. Chem. Commun. 20*, **1955**, 1340

[65] W. Haiss, B. Roelfs, S. N. Port, E. Bunge, H. Baumgaertel, R. J. Nichols, *J. Electroanal. Chem. 454*, **1998**, 107–113

[66] C. Donner, St. Kirste, *Langmuir 17*, **2001**, 1630–1636

[67] Th. Wandlowski, *J. Electroanal. Chem. 395*, **1995**, 83

[68] A. P. M. Camargo, H. Baumgärtel, C. Donner, *PCCP 5*, **2003**, 1657

[69] A. Chen, J. Lipkowski, *J. Phys. Chem. B*, 103, **1999**, 682

[70] W. J. Lorenz, G. Staikov, *Surf. Sci. 335*, **1995**, 32–43

[71] J. W. Shin, U. Bertocci, G. R. Stafford, *J. Phys. Chem. C 114*, **2010**, 7926–7932

[72] J. O'M. Bockris, S. U. M. Khan: Surface electrochemistry, a molecular level approach. Plenum Press, New York, London, **1993** ISBN 0-306-44298-1

[73] G. Y. Wu, W. Schwarzacher, *J. Electroanal. Chem. 629*, **2009**, 164–168

[74] G. Meyer, M. Michailov, M. Henzler, *Surf. Sci. 202*, **1988**, 125–141

[75] L. B. Rogers, D. P. Krause, J. D. Griess, D. B. Enrlinger, *J. Electrochem. Soc. 95*, **1949**, 33

[76] W. J. Lorenz, H. D. Hermann, N. Wuethrich and F. Jilbert, *J. Electrochem. Soc. 121*, **1974**, 1167

[77] S. Trasatti, *J. Electroanal. Chem. 33*, **1971**, 351

[78] D. M. Kolb, Advances in Electrochemical Eng., H. Gerischer, W. Tobias, Wiley and Sons, New York, **1978**

[79] E. Budevski, G. Staikov, W. J. Lorenz, Electrochemical Phase Formation and Growth, R. C. Alkire et al. (eds), VCH, Berlin, **1996**, p.41

[80] B. Beden, F. Kadirgan, C. Lamy and J M. Leger, *J. Electroanal. Chem. 142,* **1982**, 171

[81] A. Szczepanska, N. Vasiljevic, *J. Electrochem. Soc. 169*, **2022**, 112509

[82] A. Hamelin, *J. Electroanal. Chem. 101*, **1979**, 285–290

[83] A. Hamelin, A. Katayama, *J. Electroanal. Chem. 117*, **1981**, 221

[84] A. Hamelin, J. Lipkowski, *J. Electroanal. Chem. 171*, **1984,** 317

[85] R. Adzic, E. Yeager, B. D. Cahan, *J. Electrochem. Soc. 121*, **1974,** 474

[86] M. P. Green, K. J. Hanson, R. Carr, I. Lindau, *J. Electrochem. Soc. 137*, **1990**, 34–93

[87] T. A. Brunt, T. Rayment, S. J. O'Shea, M. E. Welland, *Langmuir 12*, **1996**, 5922

[88] M. F. Toney, J. G. Gordon, M. G. Sammant, G. L. Borges, O. R. Melroy, D. Yee, L. B. Sorensen, *J. Phys. Chem. 99*, **1995**, 4733

[89] D. Dickertmann, F. D. Koppitz, J. W. Schultze, *Electrochim. Acta 21*, **1976**, 967

[90] A. Bewick, B. Thomas, *J. Electroanal. Chem. 84*, **1977**, 127

[91] N. Dimitrov, A. Popov, T. Vitanov, E. Budevski, *Electrochim. Acta 36*, **1991**, 2077

[92] K. Takayanagi, D. M. Kolb, K. Kambe, G. Lehmpfuhl, *Surf. Sci. 100*, **1980**, 407

[93] D.A. Koos, V. L. Shannon, G. L. Richmond, *J. Phys. Chem. 94*, **1990**, 2091

[94] J. Sackmann, A. Bunk, R. T. Potzschke, G. Staikov, W. J. Lorenz, *Electrochim. Acta 43*, **1998**, 1223

[95] M. G. Samant, G. L. Borges, J. G. Gordon, O. R. Melroy, L. Blum, *J. Am. Chem. Soc. 10*9, **1987**, 5970

[96] L. Laguren-Davidson, F. Lu, G. N. Salaita, A. T. Hubbard, Langmuir 4, **1988**, 224

[97] C. Nagel, O. Haller, E. Platzgummer, M. Schmidt, P. Varga, *Surf. Sci., 321*, **1994**, 237

[98] J. Clavilier, J. M. Orts, J. M. Feliu, A. Aldaz, *J. Electroanal. Chem. 293*, **1990**, 197

[99] J. M. Feliu, A. Fernandez-Vega, J. M. Orts, A. Aldaz, *J. Chim. Phys. 88*, **1991**,1493

[100] K. Engelsmann, W. J. Lorenz, *J. Electroanal. Chem. 114*, **1980**, 11–24

[101] A. Hamelin, *J. Electroanal. Chem. 165*, **1984**, 167–180

[102] U. Muller, D. Carnal, H. Siegenthaler, E. Schmidr, W. J. Lorenz, W. Obretenov, U. Schmidt, G. Staikov, E. Budevski, *Phys. Rev. B, 46*, **1992**, 12899–12901

[103] D. Rath, *J. Electroanal. Chem. 150*, **1983**, 521–534

[104] T. Takamura, K. Takamura, in T. Takamura, A. Kozawa (Eds.) Surface electrochemistry: Advanced methods and concepts, Japan Scientific Societies Press, Tokyo, **1987**, pp. 229

[105] P. A. Nikolaychuk, *Ocidius Uni. Annals of Chem., 29*, **2018**, 55–67

[106] G. Y. Wu, S. E. Bae, A. A. Gewirth, J. Gray, X. D. Zhu, T. P. Moffat, W. Schwarzacher, *Surf. Sci., 601*, **2007**, 1886–1891

[107] G. Y. Wu, W. Schwarzacher, *J. Electroanal. Chem. 629*, **2009**, 164–168

[108] E. Herrero, L. J. Buller, H. D. Abruna, *Chem. Rev. 101*, **2001**, 1897–1930

[109] M. P. Green, K. J. Hanson, *Surf. Sci. 259*, **1991**, 743

[110] N. J. Tao, J. Pan, Y. Li, P. I. Oden, J. A. DeRose, S. M. Linsay, *Surf. Sci. 271*, **1992**, 338

[111] A. Crepaldi, S. Pons, E. Frantzeskakis, F. Calleja, M. Etzkorn, A. P. Seitsonen, K. Kern, H. Brune, MN. Grioni, *Physical Review B 87*, **2013**, 115–138

[112] J. W. Shin, U. Bertucci, G. R. Stafford, *J. Phys. Chem. C 114*, **2010**, 7926–7932

[113] S. Frittmann, V. Halka, R. Schuster, *Angew. Chem., Int. Ed. 55*, **2016**, 4688–4691

List of Abbreviations

CV	cyclic voltammogram
OPD	overpotential deposition
UPD	underpotential deposition
HER	hydrogen evolution reaction
OCP	open circuit potential
PZC	potential of zero charge
SEIRAS	surface-enhanced infrared absorption spectroscopy
STM	scanning tunneling microscopy
AFM	atomic force microscopy

Table of Figures

Figure 2-1 Schematic representation of the electrode/electrolyte interface for the ion and electron transport 2-9

Figure 3-1 Cyclic voltammogram of 0.1 M $K_3[Fe(CN)_6]$ / 0.1 M $K_4[Fe(CN)_6]$ 3-19

Figure 3-2 Potential pulses of 1 mM pyridine adsorption on Au(111) in 0.1 M $NaClO_4$ supporting electrolyte. 3-20

Figure 3-3 Current pulses for 0.1 M $K_3[Fe(CN)_6]$ / 0.1 M $K_4[Fe(CN)_6]$ 3-21

Figure 3-4 Temperature transient of a 2 ms long laser pulse 3-23

Figure 3-5 Exemplary laser adjustment of a current pulse 0.1 M $K_3[Fe(CN)_6]$ / 0.1 M $K_4[Fe(CN)_6]$ 3-24

Figure 3-6 Plot of the heat per charge versus the overpotential from current pulses in 0.1 M $K_4[Fe(CN)_6]$ / 0.1 M $K_3[Fe(CN)_6]$ solution on Au(111) 3-26

Figure 5-1 Cyclic voltammogram of Au(111) in 1 mM pyridine in 0.1 M $NaClO_4$ as supporting electrolyte 5-33

Figure 5-2 Cyclic voltammograms of pyridine in 0.1 M $NaClO_4$ on Au(111) recorded with various scan rates. 5-35

Figure 5-3 Effect of the scan rate 5-35

Figure 5-4 Temperature transients from anodic current pulses over the adsorption region 5-39

Figure 5-5 Linear adjustment of the molar heat of potential pulses measurement in 1 mM pyridine in 0.1 M $NaClO_4$ on Au(111) 5-42

Figure 5-6 Plot of the capacitance and the Peltier heat from all different experimental procedures versus the electrode potential 5-43

Figure 5-7 Digitized data of surface concentration-charge density curves adapted from [28]. 5-45

Figure 5-8 CVs from a Au(111) electrode in 0.1 M $NaClO_4$ solution without pyridine (green) and with different concentrations of pyridine 5-53

Figure 5-9 Peltier heat of pyridine adsorption from different concentrations 5-55

Figure 5-10 Cyclic voltammogram of Au(111) in 10 mM pyridine in 0.1 M NaF as supporting electrolyte. 5-56

Figure 5-11 Exemplary laser adjustment of current pulses 5-57

Figure 5-12 Plot of the CV and the Peltier heat from the consecutive current pulses versus the electrode potential for the system of 10 mM pyridine in 0.1 M NaF. 5-58

Figure 6-1 Cyclic voltammogram of Au(111) in 10 mM thymine and 0.1 M $NaClO_4$ as a supporting electrolyte in aqueous solution 6-65

Figure 6-2 Cyclic voltammogram of Au(111) in 10 mM thymine and 0.1 M $NaClO_4$ and the molar heat from the microcalorimetric pulse experiments 6-70

Figure 6-3 Plot of differential capacitance and molar heat against the electrode potential. 6-71

Figure 7-1 Cyclic voltammogram of Au(111) in 10 mM $Pb(ClO_4)_2$ / 1 M $HClO_4$ for lead bulk deposition. 7-6

Figure 7-2 Cyclic voltammogram of Au(111) in10 mM $Pb(ClO_4)_2$ / 1 M $HClO_4$during Pb_{UPD} on (111)-textured Au film 7-7

Figure 7-3 Cyclic voltammogram of Au(111) in 10 mM $Pb(ClO_4)_2$ / 1 M $HClO_4$ 7-9

Figure 7-4 Cyclic voltammograms of Au(111) in 10 mM $Pb(ClO_4)_2$ / 1 M $HClO_4$ recorded with scan rates of: 5, 10, 20 and 50 mV/s. 7-10

Figure 7-5 Cyclic voltammograms of Au(111) in 10 mM $Pb(ClO_4)_2$ / 1 M $HClO_4$. 7-11

Figure 7-6 Exemplary laser adjustment of current pulses 10 mM $Pb(ClO_4)_2$ / 1 M $HClO_4$ OPD on Au(111). 7-12

Figure 7-7 Linear fit of the molar heat of current pulses measurement in 10 mM $Pb(ClO_4)_2$ / 1 M $HClO_4$ on Au(111) 7-13

Figure 7-8 Exemplary laser adjustment of potential pulses for the system10 mM $Pb(ClO_4)_2$ / 1 M $HClO_4$on Au(111)..... 7-14

Figure 7-9 Linear adjustment of the molar heat of potential pulse measurement in 10 mM Pb(ClO4)2 / 1 M HClO4 on Au(111)..... 7-15

Figure 7-10 Cyclic voltammogram of Au(111) in 10 mM $Pb(ClO_4)_2$ / 1 M $HClO_4$ during Pb_{UPD} on (111)-textured Au film. 7-16

Figure 7-11 Plot of the cyclic voltammogram of Au(111) in 10 mM $Pb(ClO_4)_2$ / 1 M $HClO_4$ and the Peltier heat from all different experimental procedures versus the electrode potential (vs Pb^0/Pb^{2+}) 7-19

Figure 7-12 Plot of the cyclic voltammogram of Au(111) in 110 mM $Pb(ClO_4)_2$ / 1 M $HClO_4$ and the Peltier heat from continuous current pulses, versus the electrode potential (vs Pb^0/Pb^{2+}) 7-21

Figure 7-13 Entropic diagram for 10 mM $Pb(ClO_4)_2$ / 1 M $HClO_4$ on Au(111)..... 7-24

List of Tables

Table 5-1 Transients of continuous current pulses of 1 mM pyridine on (111)-textured Au in 0.1 M $NaClO_4$ 5-38

Table 5-2 Linear adjustment of the molar heat of continuous current pulses measurements 5-40

Table 5-3 Linear adjustment of the molar heat of potential pulses 5-41

Table 6-1 Linear adjustment of the molar heat of current pulses for the system 10 mM thymine on (111)-textured Au in 0.1 M $NaClO_4$. 6-67

Table 6-2 Linear adjustment of the molar heat of continuous current pulses 6-68

Table 7-1 Linear adjustment of the molar heat of current pulses for the system 10 mM $Pb(ClO_4)_2$ / 1 M $HClO_4$ on Au(111) 7-18

Table 7-2 Eastman entropies of transfer, molar limiting conductivities and Hittorf transfer numbers of the respective ions. 7-22

Acknowledgements

I would like to express my sincere thanks to everyone who helped and guided me throughout my academic journey.

First and foremost, I am thankful to Prof. Dr. Schuster, for the opportunity to engage with subject of molecular adsorption and for his consistent support, expert guidance and patience. I am genuinely grateful for the many lessons I have learned under his supervision.

A special thanks to Prof. Dr. Unterreiner for taking the role of a co-referee for this thesis and for the insightful discussions throughout these years.

I would also like to thank my colleagues Marcel, Marco, Laurin, Lisa, Jens, Franzi, Agnes, Janet, Detlef, Daniel, Sebastian and Steffen for the pleasant working atmosphere.

Katrin, I am beyond grateful to you! This work would not have been possible without your boundless encouragement, constant guidance and inspiration.

My endless thanks to Ane, Nina, Cveta, Alek, Vik, Ivo, Gordana, Nikolas, Marcel, Miri, Sanja, Milena and Jane for your love and friendship.

My deepest gratitude goes to my parents, Danica and Lazar, and my aunt, Ilinka. Thank you for your love, care and endless support.

Finally, Mone …Simona… dade, there are no words big enough to describe even a minute portion of my gratitude for your love, encouragement and belief in me. Therefore, I am dedicating this work to you.